THE SEARCH FOR CLUSTER STRUCTURE IN ^{14}C WITH THE PROTOTYPE AT-TPC

By

Adam Louis Fritsch

A DISSERTATION

Submitted to
Michigan State University
in partial fulfillment of the requirements
for the degree of

Physics - Doctor of Philosophy

2014

ABSTRACT

THE SEARCH FOR CLUSTER STRUCTURE IN ^{14}C WITH THE PROTOTYPE AT-TPC

By

Adam Louis Fritsch

Certain light nuclei are known to have inherent cluster structuring, and the nature of the triple-α structure of carbon isotopes is a subject of active discussion in nuclear physics. Clustering in neutron-rich nuclei is of particular interest as such work could shed light on how neutrons affect α clustering, making ^{14}C a logical candidate for such a study. Cluster structure in ^{14}C was investigated at the University of Notre Dame with the prototype Active Target-Time Projection Chamber (AT-TPC). A 38.2 MeV secondary beam of ^{10}Be was incident on an active target volume containing He:CO_2 90:10 gas at 1 atm, in which trajectories of beam particles and reaction products were measured using the tracking capabilities of the prototype AT-TPC. Angular correlations of ^{10}Be and α particles were used to reconstruct kinematics of scattering. Excitation functions and angular distributions were measured in both elastic and inelastic channels, which unraveled a number of resonances in ^{14}C. Spin-parity assignments have been made for the elastic resonances by R-matrix analysis. Evidence of a positive-parity rotational band has been indicated by the ^{14}C resonances. The proposed level scheme and the strong resonance strength observed in the inelastic channel are in line with the prediction by the antisymmetrized molecular dynamics (AMD) method indicating linear-chain structure in ^{14}C. The results also demonstrate unique and powerful potentials of active-target technology in radioactive-beam experiments and are an important step toward the construction of the full-scale AT-TPC for the ReA3 facility at NSCL.

ACKNOWLEDGMENTS

There are many people I would like to thank, starting with my advisor, Wolfi Mittig. Throughout my time as a graduate student, he has been a source of constant support, guidance, and encouragement. It's been a real pleasure working for him. I also thank Daisuke Suzuki, who has also been extremely helpful and gracious, and his work in helping setup and run my thesis experiment and his advice and guidance during my analysis have been phenomenal. Saul Beceiro-Novo also deserves much thanks, as he helped me greatly in my understanding of the physics of my work over the last year. Among the numerous other scientists who assisted me in making this dissertation become a reality, I want to specifically thank Tan Ahn, Daniel Bazin, Jim Kolata, and John Yurkon for their great help.

In addition to my group members, many of my fellow graduate students have been great to spend time with in and out of school. Jack Winkelbauer, Zach Meisel, Mike Scott, Andrew Klose, Shawna Valdez, and many others have all been amazing friends and colleagues during my time here at NSCL, and I'm forever thankful for their help and time.

From my first days at NSCL as a college freshman and continuing to today, I've had a fantastic experience interacting with many people, including Jim Brown, Michael Thoennessen, and Artemis Spyrou, who were instrumental in introducing me to the field of nuclear physics. Remco Zegers, Scott Pratt, and Vladimir Zelevinsky have also been very helpful with their advice regarding graduate school and my future career plans. I'd also like to thank Carl Bromberg and Mark Olson for their guidance during my time as a TA, and Rique Campa, Danny Caballero, and Norman Birge for helping me grow as a teacher.

My family deserves the most thanks. Their support has been unconditional, starting from my early years and continuing still. Thank you.

TABLE OF CONTENTS

LIST OF TABLES

LIST OF FIGURES

Chapter 1

Introduction

Atomic nuclei are of fundamental importance to our understanding of the universe. Researching nuclear physics tells us about the type of matter that comprises the visible universe and how that matter is created. Knowledge of matter provides limitless potential for the advancement of science and for real-world application, with medicine, energy, and defense being a few examples. One of the most effective ways to study the nucleus is through nuclear reactions. In this chapter, some of the basic tools used in nuclear reactions studies are described.

1.1 Nuclear Reactions

By colliding nuclei with sufficient energy, information such as the internal structure of an individual nucleus as well as the interactions between nuclei can be discovered. There are a variety ways to investigate nuclear reactions, but all of them share some common characteristics.

For a given reaction, there is a projectile nucleus and a target nucleus. The projectile is accelerated to some energy, anywhere from hundreds of keV up to even GeV, and is directed towards the target. In the event that the projectile strikes the target nucleus, a reaction takes place. This reaction could be a simple elastic collision, where the projectile and target simply bounce off each other and both nuclei remain in the same internal states as before the collision. Other possibilities include transfer reactions, where one of the nuclei loses a

proton or neutron to the other nucleus, and fusion reactions, in which the two nuclei combine to form one larger nucleus. There are many other types of reactions, but only elastic and inelastic collisions will be covered in further detail in this dissertation.

1.2 Elastic Collisions

As mentioned above, reactions where the projectile nucleus and incident nucleus do not change from their initial states are referred to as elastic collisions. Such a collision can be written as

$$A + B \rightarrow A + B, \tag{1.1}$$

that is, the incident projectile nucleus A enters and exits the reaction in the same nuclear state, as does the target nucleus B. A common convention is to write Eq. 1.1 as

$$B(A, A)B, \tag{1.2}$$

where again A represents the incident nucleus and B the target nucleus.

The individual kinetic energies of the two nuclei can change after the reaction, and often do, but the internal states of the nuclei do not. For example, if A is incident on B at 15 MeV, the elastic collision results in many possible exit angles and kinetic energies. The following non-relativistic conservation laws of mass, energy, and momentum determine the allowed exit angles and kinetic energies:

$$m_A + m_B = m'_A + m'_B \tag{1.3}$$

$$E_A = E'_A + E'_B \tag{1.4}$$

$$\boldsymbol{p}_A = \boldsymbol{p}'_A + \boldsymbol{p}'_B \tag{1.5}$$

where the unprimed notation denotes the states of the particle before the reaction and the primed after. The target B has no initial energy or momentum in the lab frame; if calculating

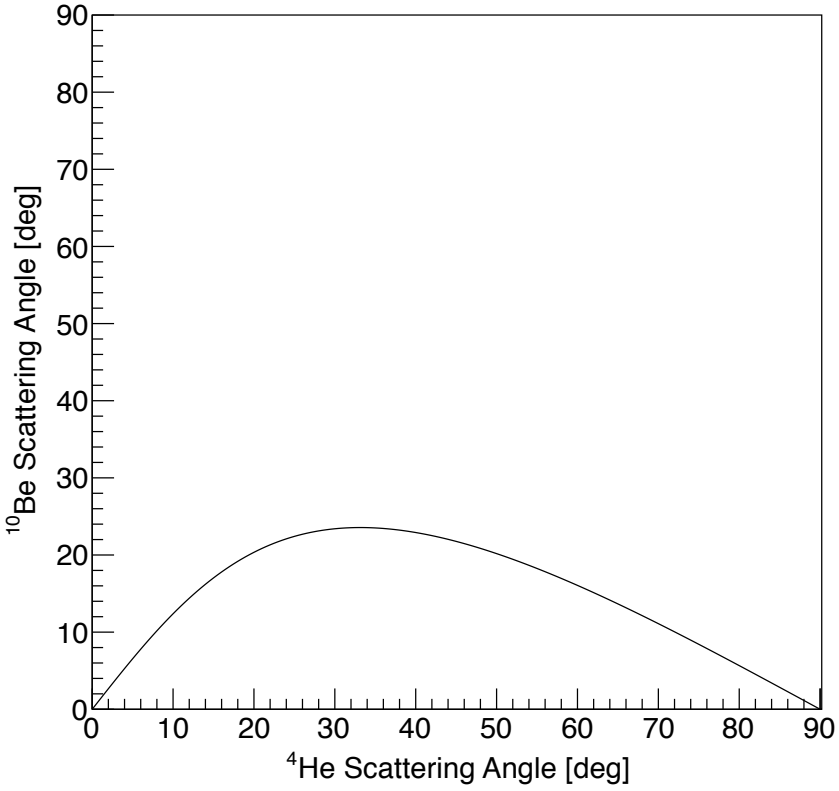

Figure 1.1: Allowed kinematical angles for ^{10}Be and ^{4}He nuclei after the elastic collision of a ^{10}Be projectile nucleus incident on a ^{4}He target nucleus. This curve is independent of the incident energy of ^{10}Be. The angles are given in the lab frame.

in the center-of-mass frame, these values must of course be included. Angles are calculated from the momentum vectors.

An important feature of elastic scattering is that for a given elastic scattering system A and B, the angular kinematics are independent of incident energy and only depend on the masses of A and B. An example plot of allowed exit angles where A is a ^{10}Be nucleus and B is a ^{4}He nucleus is shown in Fig. 1.1. From the figure, one sees that kinematically the scattered beam particle ^{10}Be can never have an exit angle larger than about 23° in the lab frame, owing to its larger mass in comparison to the target nucleus ^{4}He.

1.3 Inelastic Collisions

If during the reaction, either or both of A and B undergo a change in internal state without changing mass or charge, the reaction is called an inelastic collision. In this case, the changed nucleus or nuclei enter an excited state where the nucleus transitions to a higher energy state from its initial ground state, the lowest energy state. The spin and parity of the nucleus also may change. To denote an excited state, an asterisk (*) is put after it. Thus, if A transitions into an excited state during the reaction, one writes

$$B(A, A^*)B. \tag{1.6}$$

The conservation laws are then

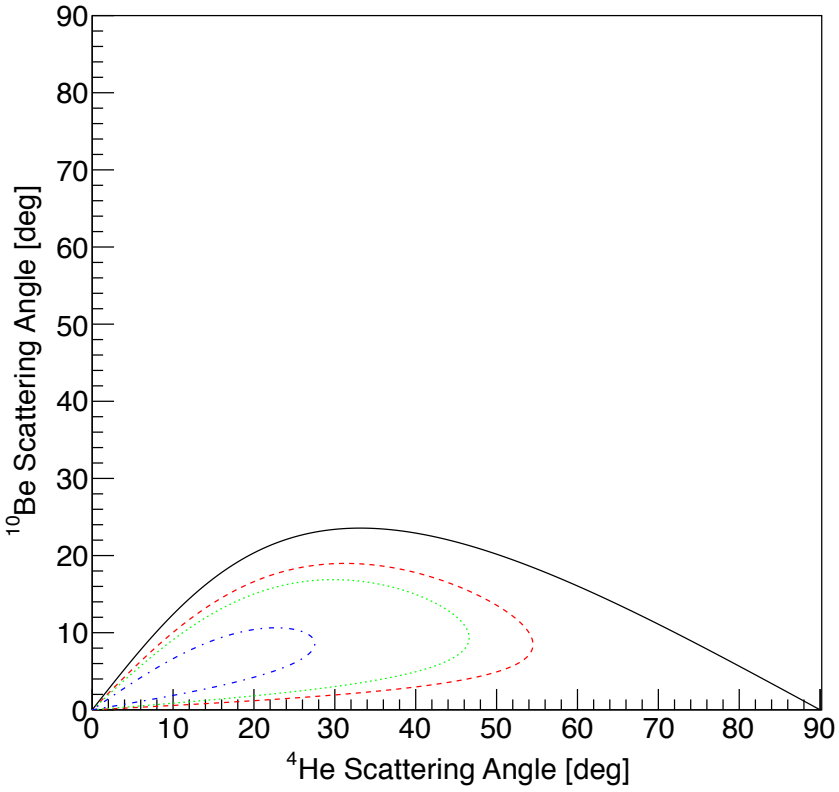

Figure 1.2: Allowed kinematical angles for ^{10}Be projectile nucleus incident on a ^{4}He target nucleus. The black curve is for elastic scattering, which is energy independent. The other three curves are for different ^{10}Be incident energies of inelastic scattering to the first excited state in ^{10}Be at 3.368 MeV. The red dashed curve is at 35 MeV, the green dotted at 25 MeV, and the blue dash-dotted at 15 MeV incident energy, respectively.

$$m_A + m_B = m'_{A^*} + m'_B \tag{1.7}$$

$$E_A = E'_{A^*} + E'_B + Q \tag{1.8}$$

$$\boldsymbol{p}_A = \boldsymbol{p}'_{A^*} + \boldsymbol{p}'_B \tag{1.9}$$

where Q represents the Q-value of the reaction, given by

$$Q = (m_A + m_B - m'_{A^*} - m'_B)c^2 \tag{1.10}$$

$$= (m_A - m'_{A^*})c^2. \tag{1.11}$$

Since the excited state A^* is at a higher energy than the initial state A, the Q-value is negative. The Q-value can be interpreted in this case as the energy threshold needed to be overcome by the incident nucleus A in order to inelastically scatter off of the target B; if E_A is less than the Q-value, the inelastic reaction is not allowed.

Therefore, unlike elastic collisions, inelastic collisions kinematics depend on the incident energy of nucleus A. Fig. 1.2 compares the allowed kinematical angles of the elastic collision and those of an inelastic collision of the type found in Eq. 1.6 at three different beam energies. As in the elastic example, here A represents a ^{10}Be nucleus and B ^{4}He. Notice that as the energy of the reaction decreases, the angular domain in which the particles ^{10}Be* and ^{4}He may scatter becomes smaller.

The two outcomes of elastic and inelastic scattering for the $A+B$ system refer to possible exit channels of the reaction. There is one exit channel for elastic scattering as written in

Eq. 1.2. In inelastic collisions, however, there is one exit channel per possible inelastic reaction. For example,

$$B(A,A^*)B \tag{1.12}$$

$$B(A,A)B^* \tag{1.13}$$

$$B(A,A^*)B^* \tag{1.14}$$

represent three separate exit channels. If there is more than one possible excited state in A or B, and there often are, then there are even more exit channels that can be populated. Approaching nuclear reactions calculations by analyzing each exit channel separately allows for the comparison of the relative influence of each channel on the reaction.

1.4 Cross Sections

Elastic and inelastic collisions can both provide information about the system being studied. A common method used to quantify the reaction rates of various exit channels is by computing the cross section σ for each channel. Cross section is a measure of the probability of a nuclear reaction occurring; thus, comparing cross sections of various exit channels gives the relative probability of the reaction taking each exit channel. When considering cross section as a function of angle, it is referred to as a differential cross section. The integrated cross section is found by taking the integral of the differential cross section over all angles. The sum of the integrated cross sections for all possible exit channels is then called the total cross section.

The differential cross section $d\sigma(\theta,\phi)/d\Omega$ can be written as

$$\sigma(\theta,\phi) \equiv \frac{d\sigma(\theta,\phi)}{d\Omega} = \frac{N}{N_{\text{inc}} n_t \sin\theta d\theta d\phi}, \tag{1.15}$$

where N is the number of reactions in a given exit channel for a given solid angle (θ,ϕ), N_{inc} is the number of incident nuclei, and n_t is the number of target nuclei per unit area. The notation $d\sigma(\theta,\phi)/d\Omega$ is often used to clearly illustrate that the differential cross section has units of area per solid angle. The unit often used when reporting a differential cross section is millibarn per steradian [mb/sr], where 1 mb $=$ 10^{-27} cm^2. It's also common to report the elastic cross section as a ratio to the Rutherford, or point-Coulomb, cross section [1]:

$$\sigma(\theta)_{\text{Ruth}} = \frac{\eta^2}{4k^2 \sin^4(\theta/2)} \tag{1.16}$$

where η is defined as

$$\frac{Z_p Z_t e^2}{E} = \frac{2\eta}{k} \tag{1.17}$$

for charges Z_p and Z_t of the projectile and target, elementary charge e, reaction energy E, and wave number k. The variables θ, E, and k are all in center-of-mass.

A sample plot of elastic and inelastic differential cross sections is given in Fig 1.3. A more detailed description of how differential cross sections are calculated experimentally will be given in the following chapters.

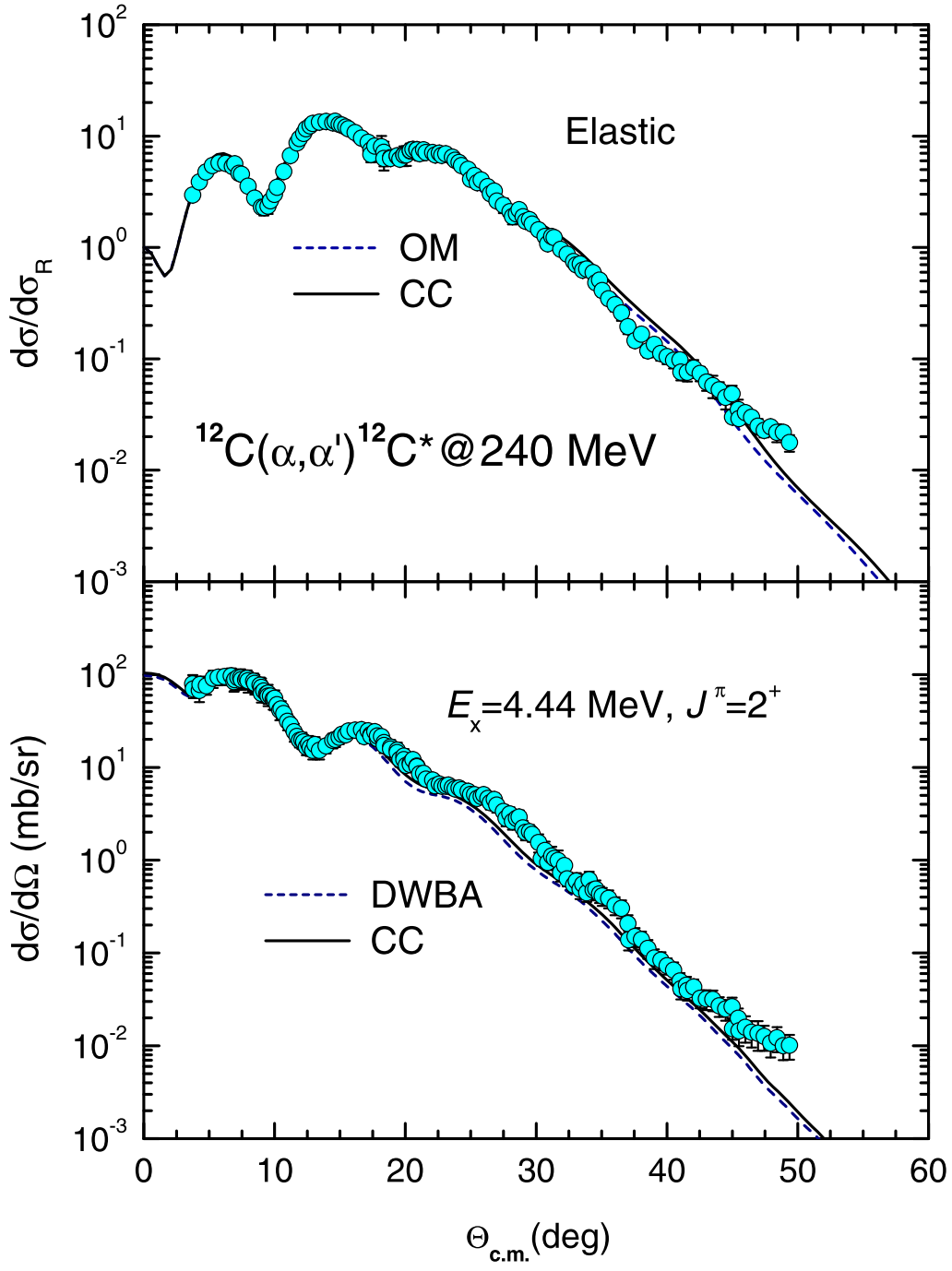

Figure 1.3: Elastic and inelastic scattering of 240 MeV α particles incident on ^{12}C. Comparisons of the data, in colored circles, to various reaction calculations, in solid and dashed lines, are shown. Figure adapted from Ref. [2].

Similarly, the integrated cross section is

$$\sigma = \int \frac{d\sigma(\theta, \phi)}{d\Omega} d\Omega. \tag{1.18}$$

In addition to energy, the properties angular momentum, spin, and parity are used to describe the internal state of the nucleus. The convention used to represent a nucleus' given state is J^{π} for

$$\boldsymbol{J} = \boldsymbol{L} + \boldsymbol{S}, \tag{1.19}$$

where total angular momentum is represented by J, angular momentum by L, spin by S, and parity by $\pi = (-1)^L$. The angular momentum terms are added as vectors in Eq. 1.19.

By employing partial wave scattering theory [1], the single channel elastic cross section can be separated into a sum of many partial waves, one for each relative angular momentum L value:

$$\frac{d\sigma}{d\Omega}_{\text{el}} = \left| \frac{1}{k} \sum_{L=0}^{\infty} (2L+1) P_L(\cos\theta) e^{i\delta_L} \sin(\delta_L) \right|^2 \tag{1.20}$$

for wave number k, Legendre polynomials $P_L(\cos\theta)$, and partial wave phase shift δ_L [1]. Note that the relative angular momentum L in Eq. 1.20 is not the same as the intrinsic angular momentum L in Eq. 1.19.

At small angles, the Coulomb potential dominates and causes the cross section to tend to infinity. Because of this, Eq. 1.20 is often divided by the point-Coulomb cross section from Eq. 1.16, allowing for the non-Coulomb processes present in elastic scattering to be quantified.

Integrating Eq. 1.20 over all angles yields [1]

$$\sigma_{\text{el}} = \frac{4\pi}{k^2} \sum_{L=0}^{\infty} (2L+1) \sin^2 \delta_L. \tag{1.21}$$

Quantifying cross sections as a function of exit angle is a useful method for assigning angular momentum states L to various exit channels in a reaction. To make determinations about the energy of excited states that are populated in a reaction, the dependence of cross section on reaction energy must be studied.

1.5 Excitation Functions and Resonances

In addition to measuring cross sections at various angles, it is often useful to examine them as a function of reaction energy. Such cross sections

$$\sigma(E) \equiv \frac{d\sigma(E)}{dE} \tag{1.22}$$

are then called excitation functions [1]. If the excitation function is not fully integrated over all angles, it is then expressed as

$$\frac{d\sigma^2(E,\theta,\phi)}{d\Omega dE}. \tag{1.23}$$

Example plots of experimental excitation functions are given in Fig. 1.4.

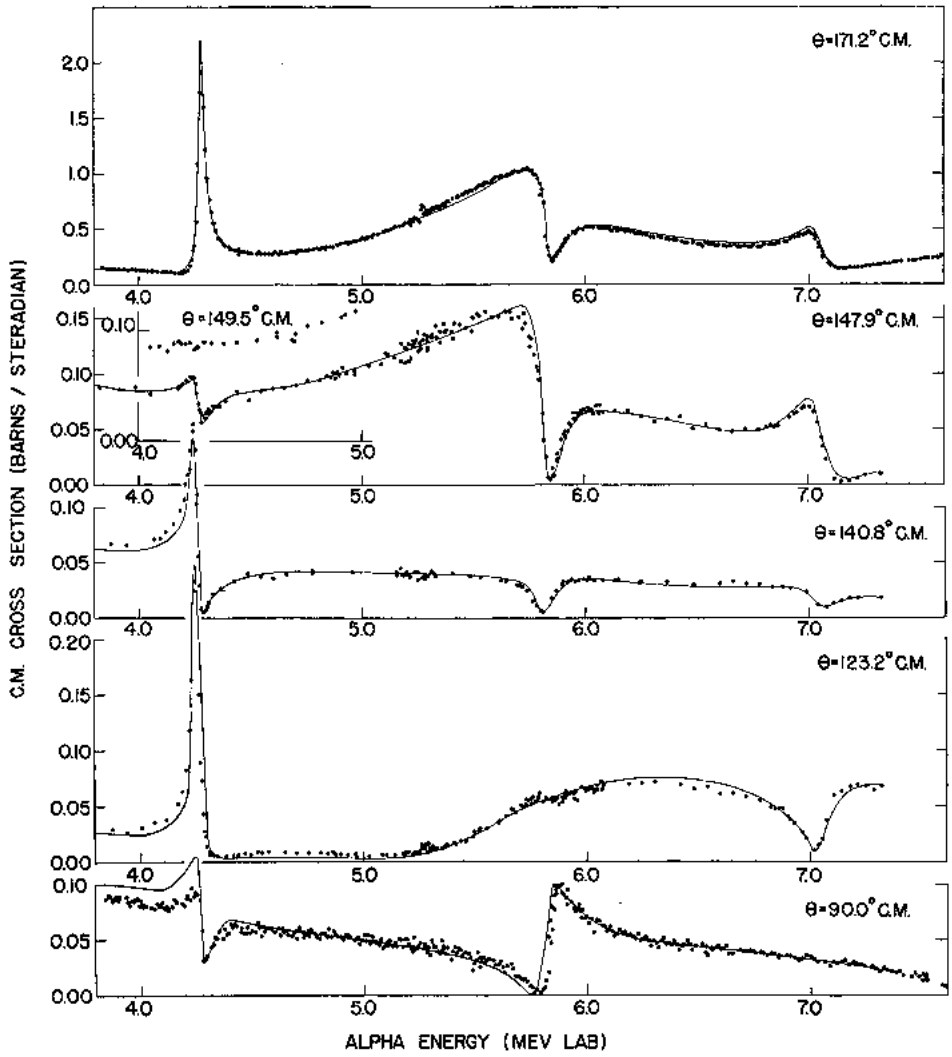

Figure 1.4: Excitation functions of α+^{12}C elastic scattering at various angles. Resonances in the compound nucleus ^{16}O are seen. The points are experimental data. The solid lines are a theoretical fit. Figure from Ref. [3].

When looking at an excitation function, the structure of the data can reveal a resonance. While it is not a bound state, the resonance forms a discontinuity in the excitation function near the energy E_r. Resonances can be described in part by their energy widths Γ, which are related to the lifetime τ over which the resonance occurs. This relation is constrained by the Heisenberg Uncertainty Principle [4]

$$\Delta E \Delta t \sim \hbar \tag{1.24}$$

for the reduced Planck constant $\hbar = 6.58 \times 10^{-16}$ eV·s. Thus, the longer lived the resonance is, the narrower its peak will be:

$$\Gamma \sim \hbar/\tau. \tag{1.25}$$

Experimentally, Γ is defined as the full width at half maximum (FWHM) of the resonance peak found at E_r in the excitation function. The contribution of the resonance to the integrated elastic cross section is [5]

$$\sigma_{\text{el}}^{\text{res}} = \frac{4\pi}{k^2}(2L+1)\frac{\Gamma^2/4}{(E-E_r)^2+\Gamma^2/4}. \tag{1.26}$$

Such a description is called a Breit-Wigner resonance. Eq. 1.26 is valid in its given form only if the background phase shift $\delta_{\text{bg}}(E)$ is near zero and thus negligible; in other cases, there

may be interference effects between the resonance and the background potential scattering that must be considered [1].

If there is also an inelastic exit channel for the same resonance as seen in the elastic channel, Eq. 1.26 becomes [4]

$$\sigma_{\text{inel}}^{\text{res}} = \frac{4\pi}{k^2}(2L+1)\frac{\Gamma_c\Gamma_{c'}/4}{(E-E_r)^2+\Gamma^2/4}. \tag{1.27}$$

Here, Γ_c represents the partial width from the elastic channel, $\Gamma_{c'}$ represents the partial width from the inelastic channel, and $\Gamma = \Gamma_c + \Gamma_{c'}$ is the total width of the resonance. Also, the total cross section would become the sum of the two integrated cross sections [1]:

$$\sigma_{\text{tot}}^{\text{res}} = \sigma_{\text{el}}^{\text{res}} + \sigma_{\text{inel}}^{\text{res}}. \tag{1.28}$$

If necessary, any other possible contributions from other exit channels must be included when calculating the total width Γ of the resonance and thus the total cross section $\sigma_{\text{tot}}^{\text{res}}$ of the reaction.

Furthermore, the partial width of the resonance of a given exit channel c for angular momentum L can be expressed as [5]

$$\Gamma_c(L,E) = 2P_c(L,E)\gamma_c^2(L) \tag{1.29}$$

for $P_c(L)$ as the penetrability and $\gamma_c^2(L)$ as the reduced width of the channel. The penetrability describes the barrier penetration of the two nuclei during the reaction. The reduced width is defined, for a single-particle state, as [5]

$$\gamma_c^2(L) = \frac{\hbar^2 u_L^2(R)}{2\mu R} \tag{1.30}$$

where μ is the reduced mass of the system and $u_L(R)$ is the energy eigenstate of the radial Schrödinger equation [1]

$$u_L''(R) = \left[\frac{L(L+1)}{R^2} + \frac{2\mu}{\hbar^2}(V(R) - E)\right] u_L(R) \tag{1.31}$$

at the interaction radius

$$R = 1.2\left(A_1^{1/3} + A_2^{1/3}\right) \text{ fm} \tag{1.32}$$

for mass numbers A_1 and A_2 of the two nuclei [5]. Mass number is the number of nucleons in a given nucleus and is dimensionless. The value of the partial width goes to zero at the energy threshold of the resonance.

An important note is that the preceding expressions for cross section all assume that the projectile and target both have a spin of zero. If the two nuclei have non-zero spin, these spins must be taken into account in the cross section calculations by adding the spin weighting function [4]

$$g = \frac{2J+1}{(2S_p+1)(2S_t+2)} \tag{1.33}$$

where J is the total angular momentum and S_p and S_t are the entrance channel spins of the projective and target, respectively. Notice that when $S_p = S_t = 0$, Eq. 1.33 simplifies to $2L+1$, as has been used previously. The projectile and target investigated in this work are both spin-zero particles, and thus have cross sections that are well described by the equations found in this chapter where $g = 2L+1$.

1.6 Optical Potentials

When investigating nuclear reactions, it's useful to pick a model describing the reaction that has an effective way to separate the elastic collision from other reaction mechanisms. One such way to do so is by using an optical potential.

Optical potentials describe the interaction between colliding nuclei with a real and imaginary term, where the imaginary term functions to absorb the flux to any non-elastic reaction channels, which is analogous to the absorption of light in a semi-transparent medium; hence the name, optical potential [6].

The complex potential has the form

$$V(R) + iW(R). \tag{1.34}$$

The real part is given by

$$V(R) = \frac{-V_r}{1 + \exp\left(\frac{R-R_r}{a_r}\right)}, \tag{1.35}$$

for the central depth of the potential V_r, diffuseness a_r, and nuclear radius R_r for a distance R between the nucleon and nucleus [1]. The free parameters V_r, a_r, and R_r have typical values of

$$V_r \sim 40 - 50 \text{ MeV} \tag{1.36}$$

$$a_r \sim 0.6 \text{ fm} \tag{1.37}$$

$$R_r \sim 1.2A^{1/3} \text{ fm} \tag{1.38}$$

where A is the mass number of the nucleus. Similarly, the imaginary term is [1]

$$W(R) = \frac{-V_i}{1 + \exp\left(\frac{R-R_i}{a_i}\right)} \tag{1.39}$$

for

$$V_i \sim 10 - 20 \text{ MeV} \tag{1.40}$$

$$a_i \sim 0.6 \text{ fm} \tag{1.41}$$

$$R_i \sim 1.2A^{1/3} \text{ fm.} \tag{1.42}$$

The shape of these potentials is called the Woods-Saxon, or Fermi, shape [1]. The values of the parameters are found by fitting the full complex potential to data and are thus phenomenological. Generally, optical models must account for spin, but as discussed previously, the spin of both of the projectile and target in the entrance channel in this work are zero, and thus is ignored here.

Eq. 1.34 is inserted as the potential in the radial Schrödinger equation from Eq. 1.31, allowing cross sections to be calculated over a continuous energy domain.

By utilizing an optical potential, elastic scattering can be well described and its contribution to the total cross section understood. Other exit channels can then be investigated in proper context to the elastic channel.

1.7 Relation to Current Work

The concepts and equations discussed in this chapter are of great importance to the following work in this dissertation. They will be referred to often, and understanding them is essential to follow the arguments made going forward. For more detailed discussions of nuclear reactions, cross sections, and resonances, as well as more general topics in nuclear physics, see Refs. [1, 4, 5].

Chapter 2

Motivation

The experiment and analysis discussed in this work has two main motivations: one of physics, and one of technical development. The physics of interest is the study of the clustering of ^{14}C via resonant scattering of ^{10}Be incident on ^{4}He. The device used to measure the resonances was the prototype Active Target-Time Projection Chamber. The following sections with delve into detail on both of these motivations.

2.1 Molecular Clustering of Carbon Isotopes

Cluster structure in nuclei has long been predicted; α clustering in particular has been discussed since at least the mid-1930s [7]. It is still at the forefront of nuclear physics, as shown by the impressive number of recent publications [8, 9, 10, 11, 12]. Clustering is often described as molecular in nature, as the clustering of nuclei into a composite nucleus is analogous to atoms forming a molecule [2, 13, 14, 15, 16]. For example, linear-chain configurations have been proposed in nuclei over the years [17, 18].

One such nucleus that may be described via molecular clustering is ^{12}C. How the three α particles cluster to form ^{12}C is important to understanding the properties of the energy levels of ^{12}C. Of particular interest is the Hoyle state in ^{12}C [2, 19, 20, 21]. The 0^+ Hoyle state is the second excited state in ^{12}C and is found at 7.6542 MeV. This energy is only 287 keV above the three-α breakup threshold and can only be formed when a resonant state in ^{8}Be

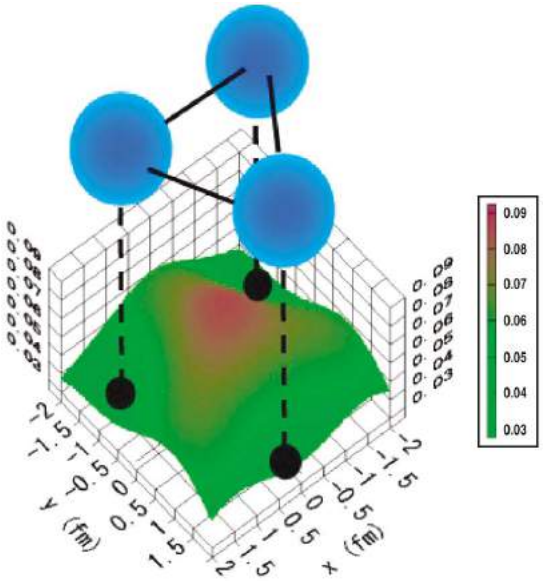

Figure 2.1: The density distribution of the excess neutrons in ^{14}C on the xy plane before the angular momentum projection, based on the molecular-orbit model. The spheres show the positions of the α clusters. The distance between the centers of the α clusters is set to 3 fm, forming an equilateral-triangle shape. The density is integrated over the z axis. Figure adapted from Ref. [22].

pairs with a free α [1]. A narrow resonance of 8.3 eV breadth, the Hoyle state is essential in explaining the observed nuclear abundances of the universe; without it, not only would there be less or no ^{12}C, but all of the nucleosynthesis processes that build on ^{12}C would be impacted. In fact, it's from studying abundances of heavier isotopes that prompted Hoyle to suggest an excited state in ^{12}C near the three-α breakup threshold in the first place [19].

A complimentary nucleus to study of relevance to ^{12}C is ^{14}C. By analyzing a three-α system with two additional neutrons, the role that the neutrons play in the clustering of ^{14}C can shed light on how all C isotopes are structured [13].

An important feature of excited three-α-cluster states is the configuration of the nucleus. Various theoretical works have been made to describe these configurations [13, 22, 23, 24, 25]. Equilateral-triangle shapes in ^{14}C have been predicted [22] based on the molecular-orbit

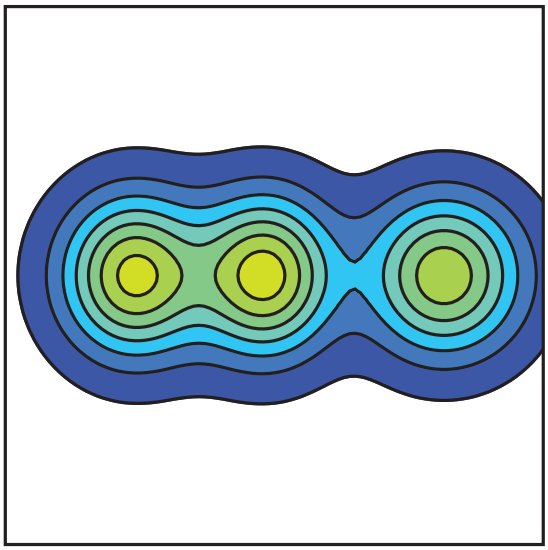

Figure 2.2: Density distribution of protons in positive-parity states of ^{14}C of intrinsic wave functions at $(\beta\cos\gamma, \beta\sin\gamma) = (0.93, 0.04)$ on the $\beta - \gamma$ plane, showing a linear-chain structure with a $^{10}\mathrm{Be} + \alpha$ correlation. The size of the box is 10×10 fm^2. Figure adapted from Ref. [13].

model (Fig. 2.1), as have linear-chain structures [13] based on antisymmetrized molecular dynamics (Fig. 2.2), among other possible configurations.

In Ref. [13], linear-chain structure is predicted not only for one state, but for an entire rotational band, with a strong overlap with $^{10}\mathrm{Be} + \alpha$. Up to now, no experimental evidence has been found for the existence of linear-chain structure in ^{14}C.

Chapter 3 describes the theory presented in Ref. [13] that predicts linear-chain structure, and includes more details on the properties of the rotational band.

2.2 Development of Prototype AT-TPC and AT-TPC Project

In addition to physics motivation, the technical development of the Active Target-Time Projection Chamber, or AT-TPC, project is also important. The AT-TPC is a newly-built device used to study nuclear reactions. The development of the project has included the designing and building of a test chamber [26] and prototype AT-TPC [9, 27].

For this work, the prototype AT-TPC was used, and it has provided many important details about the performance of the device and how to develop the full-scale AT-TPC. Other prior tests and experiments [9, 26, 27] have been carried out to investigate the device's performance and scientific promise. The large angular coverage and active target nature of the prototype AT-TPC is well suited to investigate α clustering in ^{14}C, as various resonance energies can be probed while discriminating between elastic and inelastic scattering of ^{10}Be on α particles.

In this section, a basic description of how the device functions will be given, as well as its impact on the development of the full-scale AT-TPC. The details of the exact experimental setup used in the collection of data in this work will be described in later chapters.

2.2.1 Context of the AT-TPC Project

The current and next generation of accelerators are able to provide radioactive isotope beams at a large variety of energies and intensity, allowing for more types of nuclear reactions to be studied [28, 29, 30, 31]. The development of the AT-TPC project has been undertaken to

provide higher luminosity, efficiency, and resolution in nuclear reactions experiments through the use of active target and time projection chamber capabilities [27].

The full-scale device, installed at NSCL, provides (1) a large active volume defined by an electron drift region of 100 cm along the beam axis and a circular readout plane of 60 cm in diameter, (2) a high electric field (1 kV/cm) for fast electron drift to minimize the detector dead time, (3) high granularity of the readout plane (10,240 pads), (4) efficient waveform digitization of signals by the General Electronics for TPC (GET) currently under development in collaboration with IRFU/SPhN CEA-Saclay, CENBG, GANIL, NSCL, and RIKEN laboratories [32], (5) magnetic rigidity analysis using a superconducting solenoid magnet, and (6) the application of a recently-developed electron amplification technology, Micromegas [26, 33], to an active target [27].

This work was done using the prototype AT-TPC, which uses 253 readout pads in a cylindrical volume 50 cm long and 28 cm in diameter. It is a larger and more efficient device than other existing active target TPCs [34, 35, 36].

The following subsections will describe how the prototype device achieves these features.

2.2.2 Time Projection Chambers

One of the defining features of the prototype AT-TPC is that it is a time projection chamber, or TPC [34, 37, 38, 39, 40]. A TPC functions as a gas-filled ionization drift chamber that allows for the reconstruction of the trajectory of a charged particle [39]. The TPC is filled with a neutral gas, which is ionized by charged particles traversing the gas volume. By setting a fixed electric field across the chamber, the freed electrons then drift to one end of the TPC, where an electron amplifier is located. The segmentation of the electron amplifier gives the position for the two in-plane spatial dimensions. The third spatial dimension is

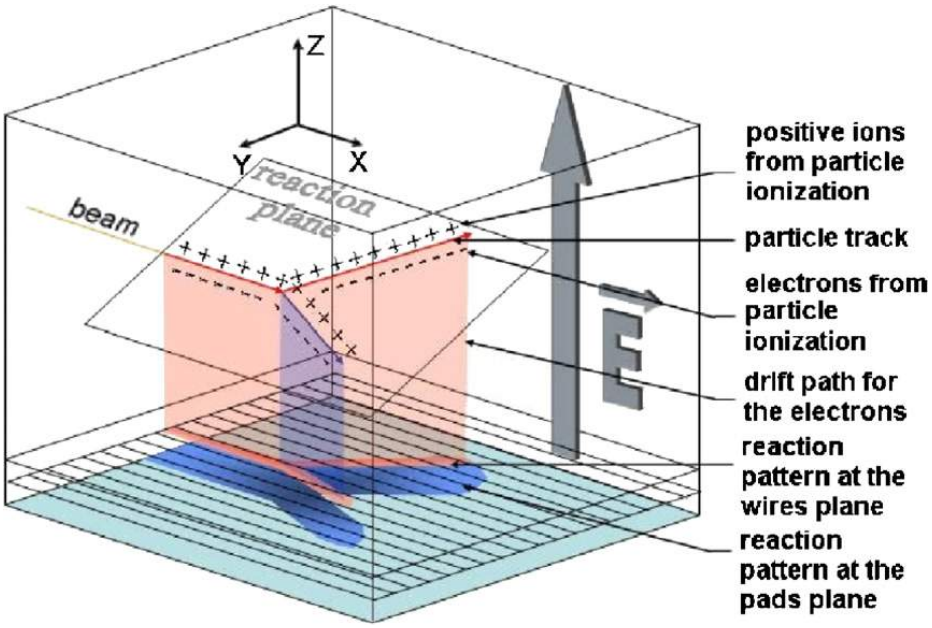

Figure 2.3: Schematic diagram of the ionization process for the MAYA detector, a type of TPC. The electrons drift down against the electric field to the wire plane, where they are detected. The charged particle trajectories can then be reconstructed. Figure from Ref. [34].

obtained by measuring the electron drift time. The time can be converted to a distance by multiplying this time by the drift velocity of the electrons in the electric field. Fig. 2.3 gives a schematic of the TPC principle as seen in MAYA, a TPC used at GANIL [34].

As the charged particles travel through the gas in the TPC, they lose energy. This energy loss is dependent in part on the length of the particle tracks. By measuring the length elements dx of a track that a charged particle has traveled in the TPC, the particle's energy loss dE can be calculated. The rate of energy loss per unit length is given by the Bethe formula [41]

$$-\frac{dE}{dx} = \frac{4\pi e^4 z^2}{m_0 v^2} NB \tag{2.1}$$

where

$$B \equiv Z\left[\ln\frac{2m_0v^2}{I} - \ln\left(1-\frac{v^2}{c^2}\right) - \frac{v^2}{c^2}\right] \tag{2.2}$$

for velocity v and charge ze of the charged particle, number density N and atomic number Z of the tracking gas in the TPC, electron mass m_0, electric charge e, speed of light c, and average ionization potential I of the gas [41].

The trajectories and energy losses of charged particle tracks can be measured in TPCs. How the electrons freed by the ionization of the gas by the charged particles are detected will now be discussed.

2.2.3 Micromegas

The number of primary electrons released in the ionization of the gas by charged particles is too low to be measured; thus, an amplification of these electrons is needed before the electronics can process the signal. For different TPC devices, various types of electron multipliers can be used. Some examples include a Frisch grid with proportional wires [34] and GEM detectors [42]. For the prototype AT-TPC, the detector plane is constituted by Micromegas [33]. The name is derived from the term MICRO-MEsh-GAseous Structure, and it is a type of gas-electron amplification device [33].

Micromegas consists of a micromesh held over an anode readout plane [27]. For the Micromegas used in this work, the micromesh is held at a uniform distance of 128 μm above the anode readout plane. The mesh itself is made of 18 μm thick stainless steel wire woven

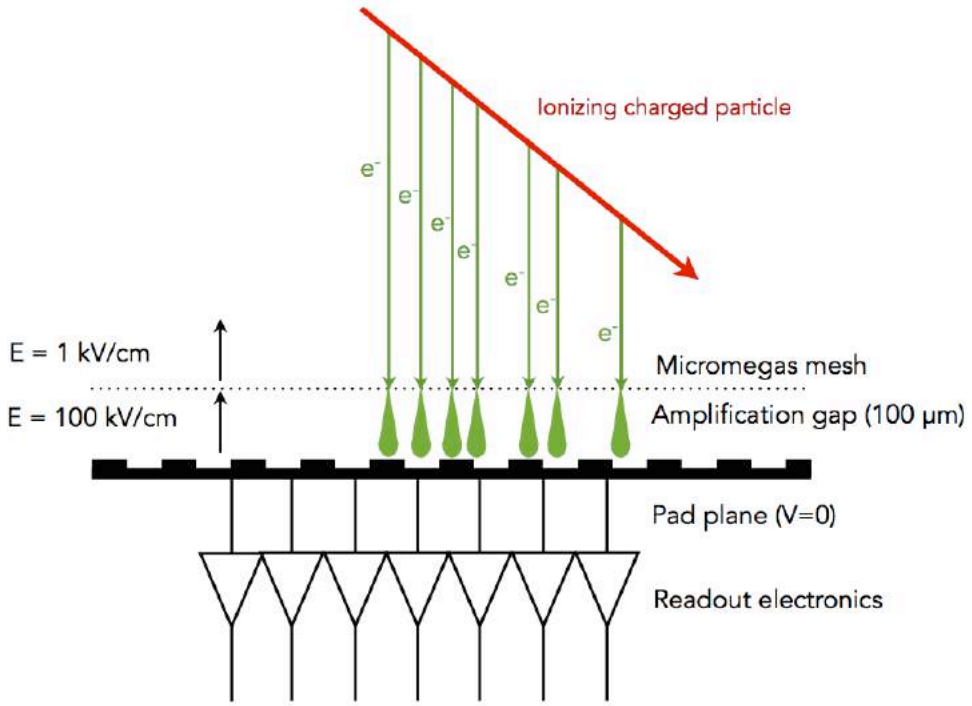

Figure 2.4: Schematic of Micromegas amplification technique. Figure adapted from Daniel Bazin.

at a pitch of 63 μm. Insulated pillars are placed 2 mm apart on the readout plane in a grid configuration to hold the micromesh at a uniform distance above the readout plane [27].

The electric field between the micromesh and the anode plane is much higher than that found in the rest of the detector; the field in the Micromegas is on the order of 10 to 100 kV/cm while it's only on the order of 1 kV/cm in the volume where the charged particles ionize the gas in the TPC. This greatly increased field allows for amplification of the electrons, which produces a much larger signal that then can be read out [27]. Typical amplification factors can reach up to 10,000, depending on the gas, the gas pressure, and the electric field.

The anode readout plane is segmented into pads. Each pad has its own dedicated readout electronics channel. Gain can be varied pad by pad by applying a unique voltage to each pad. This gain variation capability of the Micromegas was essential for the triggering of reaction

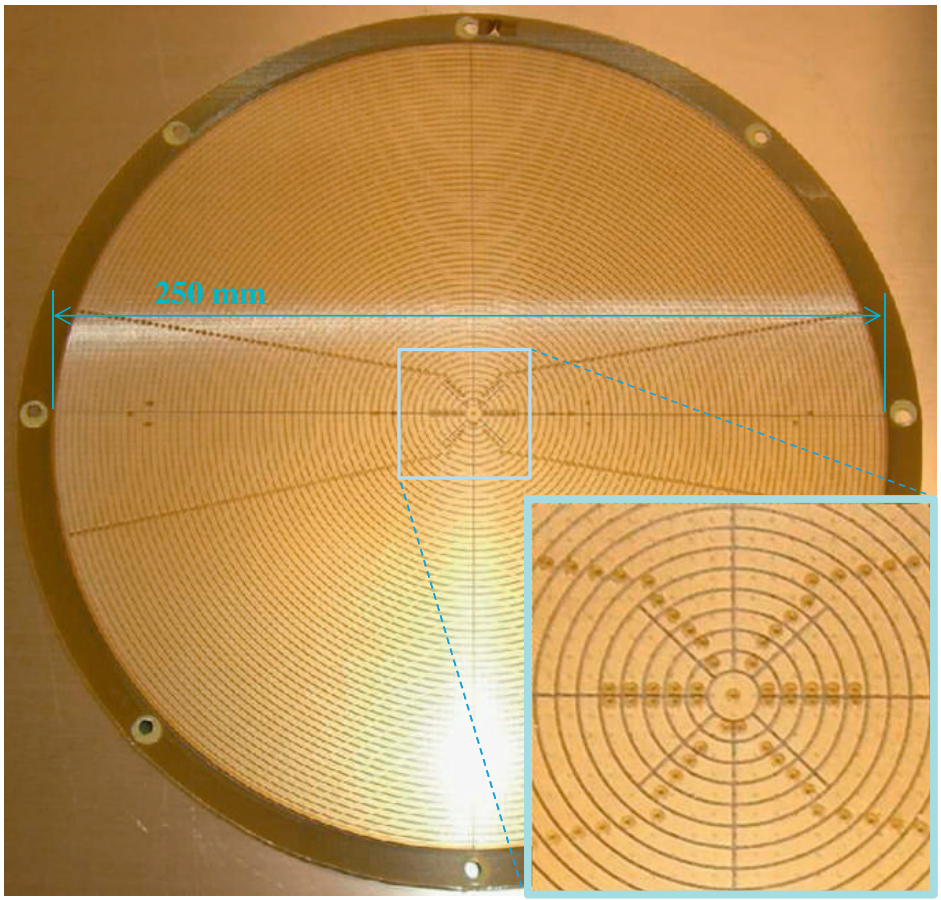

Figure 2.5: Photograph of the Micromegas. The inset shows a magnified view of the central region. The central pad has a diameter of 5 mm, while the other coaxial strips have a pitch of 2 mm. The pads are separated by a 0.25 mm gap. Figure from Ref. [27].

events investigated in this work. With the prototype in this work, there are 252 concentric pads separated into quadrants; the full-scale device uses 10,240 much smaller pads over a larger area. The 2 mm width of the pads used with the prototype allows for radial resolution of also about 1 mm, achieving good precision in determining the range and thus kinetic energy of charged particles in the device [27]. The radial structure of the pads is conducive to measuring two-body reactions. A picture of the Micromegas used in this work is given in Fig. 2.5. An illustration of the TPC technique for measuring a two-body reaction with the Micromegas is shown in Fig. 2.6. More details on the specific Micromegas used in this

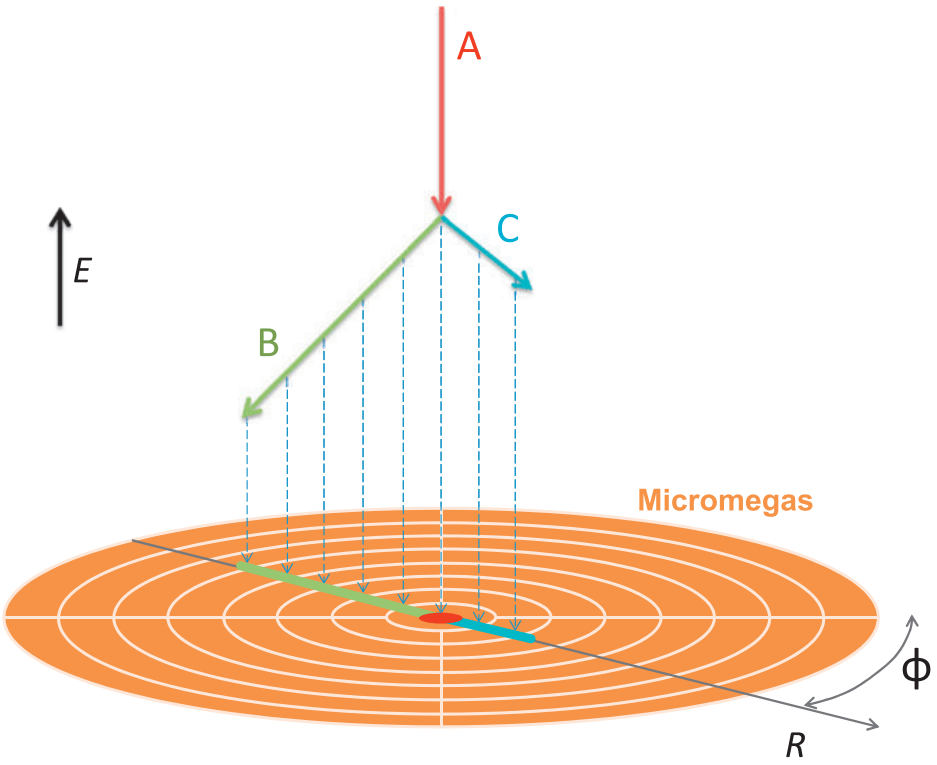

Figure 2.6: llustration of tracking. The beam particle (indicated by A and red) collides with a gas nucleus and produces reaction products (B, green and C, blue). The ionization electrons (dashed lines) are transported by the electric field (E), making a projected image on the surface of the Micromegas. The energy deposit profile of the beam particle is measured by the central pad, while those of particles B and C are measured by the coaxial strips. The track is segmented by 2 mm pitch strips in the R direction, thus providing a resolution of 2 mm or less, while the azimuth ϕ information is absent. Figure from Ref. [27].

work, as well as the Micromegas circuit and readout electronics, are given in Sections 4.2.4 and 4.2.5.

2.2.4 Active Target Mode

Another defining feature of the prototype AT-TPC is that it acts as an active target, that is, the gas medium used for TPC tracking also serves as the reaction target for beam nuclei [27]. When using an active target, the pressure at which the gas is held determines the density of gas particles and thus the thickness of the target. If the study of the entire energy domain of

a given beam energy is desired, the gas pressure should be sufficiently high to allow for the stopping of the beam in the device. The energy loss profile of the beam particles is described by the Bethe formula, defined previously in Eq. 2.1.

Since the gas is used as both a tracking medium and target, the choice of gas varies experiment to experiment. In this work to study ^{10}Be scattered by ^{4}He, a He:CO_2 90:10 mixture at around 1 atm of pressure is used. The ^{10}Be beam particles are incident on the gas at about 4 MeV/u. As they travel through the active target and lose energy, the ^{10}Be nuclei will, with some probability, scatter off of target ^{4}He nuclei. The position of the vertex of the reaction along the beam axis can be calculated with the TPC capabilities of the device. The vertex is converted to the energy of the reaction via Eq. 2.1. Since the ^{10}Be nuclei lose nearly all of their kinetic energy by the time they traverse the full length of the detector, reactions in the prototype AT-TPC occur across almost the entire energy domain of the beam. The number of reactions that occur at a given vertex, and thus reaction energy, gives the cross section $d\sigma(E)/d\Omega$ of the reaction. The active target capability of the device results in nearly the entire energy spectrum of the entering ^{10}Be beam particles being probed, allowing for $^{10}\mathrm{Be} + {}^{4}\mathrm{He}$ reactions at many different energies to be studied.

Scattering of ^{10}Be on the quench gas nuclei ^{12}C and ^{16}O was not observed due to the short ranges of the ^{12}C and ^{16}O nuclei in the gas. Thus, such scattering events were not a source of background scattering in the data.

As described above, the prototype AT-TPC was used in active target mode for this work. If so desired, for other types of experiments a solid foil target can be placed in the detector. In this case, the prototype device would act as a TPC. The prototype has not yet been used in this fixed target mode. The full-scale AT-TPC in particular is designed with such a capability.

Chapter 3

Theory

This chapter describes the theoretical method of β-γ constraint Antisymmetrized Molecular Dynamics (AMD) and the Generator Coordinate Method (GCM), or the β-γ constraint AMD + GCM, presented by Suhara and Kanada-En'yo in their papers Refs. [13, 43]. Their discussion of the structures of ground and excited states in ^{14}C motivated this work. For more details on how the results of Ref. [13] motivated this work, see Section 2.1.

3.1 Antisymmetrized Molecular Dynamics

First mentioned in Ref. [15] and described in Ref. [44], Antisymmetrized Molecular Dynamics (AMD) is a theoretical framework used to model molecule-like structure of nuclear states, among other approaches [22, 45, 46]. In this section, the basic formulation of AMD as used in Ref. [13] is presented.

The origins of AMD are in other microscopic simulation methods, such as Quantum Molecular Dynamics (QMD) [47], an N-body theory that can describe the mean field effect and the dynamics of fragment formation. However, since QMD represents nucleons as distinguishable Gaussian wave packets in phase space, ground states of nuclei are described semi-classically by imitating the Thomas-Fermi model of phase space distribution. Various improvements have been made to QMD to improve its treatment of the fermionic nature of nucleons, including introducing Pauli potentials [48, 49]. The introduction of an antisym-

metrized version of molecular dynamics, called Fermionic Molecular Dynamics (FMD) [14], created a method that treats the fermionic nature of nucleons exactly. In FMD, a Slater determinant of Gaussian wave packets of nucleons is used to build the wave function of a many-body system, and the time-dependent variational principle is used to describe the time development of the wave packet parameters [50]. Modified versions of FMD, such as found in Ref. [15], where the time variations of the width parameters and the spin wave functions are neglected have been shown to make the FMD method free of assumptions such as axial symmetry and even clustering structure. The incorporation of two-nucleon collision processes has been successfully implemented into this modified FMD, which is now referred to as Antisymmetrized Molecular Dynamics (AMD) [44].

3.2 Description of β-γ Constraint AMD + GCM

3.2.1 AMD Wave Functions

The AMD method describes an A-nucleon system's basis wave function $|\Phi\rangle$ as a Slater determinant of single-particle wave functions $|\varphi_i\rangle$ as [13]

$$|\Phi\rangle = \frac{1}{\sqrt{A!}} \det\{|\varphi_1\rangle, ..., |\varphi_A\rangle\}. \tag{3.1}$$

Each single-particle wave function $|\varphi_i\rangle$ is described by its spatial $|\phi_i\rangle$, spin $|\chi_i\rangle$, and isospin $|\tau_i\rangle$ components as

$$|\varphi_i\rangle = |\phi_i\rangle|\chi_i\rangle|\tau_i\rangle. \tag{3.2}$$

The spatial term is described as a Gaussian wave packet centered at $\boldsymbol{Z}_i/\sqrt{\nu}$ of the form

$$\langle \boldsymbol{r}|\phi_i\rangle = \left(\frac{2\nu}{\pi}\right)^{3/4} \exp\left[-\nu\left(\boldsymbol{r} - \frac{\boldsymbol{Z}_i}{\sqrt{\nu}}\right)^2 + \frac{1}{2}\boldsymbol{Z}_i^2\right] \tag{3.3}$$

for width parameter ν common to all single-particle Gaussian wave functions [13]. The parameter $\boldsymbol{\xi}_i$ determines spin orientation as

$$|\chi_i\rangle = \xi_{i\uparrow}|\uparrow\rangle + \xi_{i\downarrow}|\downarrow\rangle \tag{3.4}$$

and isospin is fixed to be either up (proton) or down (neutron) [13]:

$$|\tau_i\rangle = |p\rangle \text{ or } |n\rangle. \tag{3.5}$$

For a basis wave function $|\Phi\rangle$, the complex variational parameters

$$\{X\} \equiv \{\boldsymbol{Z}, \boldsymbol{\xi}\} = \{\boldsymbol{Z}_1, \boldsymbol{\xi}_1, \boldsymbol{Z}_2, \boldsymbol{\xi}_2, ..., \boldsymbol{Z}_A, \boldsymbol{\xi}_A\} \tag{3.6}$$

are determined by energy optimization [13].

3.2.2 Parity and Angular Momentum Projections

Projections of the AMD wave function $|\Phi\rangle$ onto the parity and angular momentum eigenstates are done with the parity projection operator $\hat{P}^{\pm}$ and angular momentum projection operator $\hat{P}^{J}_{MK}$, respectively. The operators are defined as [13]

$$\hat{P}^{\pm} \equiv \frac{1 \pm \hat{P}}{2} \tag{3.7}$$

for parity operator $\hat{P}$ and

$$\hat{P}^{J}_{MK} \equiv \frac{2J+1}{8\pi^2} \int d\Omega \; D^{J*}_{MK}(\Omega) \hat{R}(\Omega) \tag{3.8}$$

for Euler angles $\Omega = (\alpha, \beta\gamma)$, Wigner's D function $D^{J*}_{MK}(\Omega)$, and rotation operator

$$\hat{R}(\Omega) = e^{-i\alpha\hat{J}_z} e^{-i\beta\hat{J}_y} e^{-i\gamma\hat{J}_z}. \tag{3.9}$$

Note that the operator given in Eq. 3.8 is written for the case of axial symmetry. Variation is performed for the parity projected wave function

$$|\Phi^{\pm}\rangle \equiv P^{\pm}|\Phi\rangle, \tag{3.10}$$

after which $|\Phi^{\pm}\rangle$ is projected onto the total angular momentum eigenstates. Thus, the parity projection is made before the variation, while the total angular momentum projection is made after [13].

3.2.3 Constraint Variation on Quadrupole Deformation Parameters, β and γ

When the energy variation is performed, constraints are placed on the quadrupole deformation parameters, β and γ. These constraints are made so that the cluster and shell-model structures in ground and excited states of ^{14}C can be described with the AMD model and have their deformation characterized [13]. The deformation parameters are defined as

$$\beta\cos\gamma \equiv \frac{\sqrt{5\pi}}{3}\frac{2\langle\hat{z}^2\rangle - \langle\hat{x}^2\rangle - \langle\hat{y}^2\rangle}{R^2}, \tag{3.11}$$

$$\beta\sin\gamma \equiv \sqrt{\frac{5\pi}{3}}\frac{\langle\hat{x}^2\rangle - \langle\hat{y}^2\rangle}{R^2}, \tag{3.12}$$

$$R^2 \equiv \frac{5}{3}\Big(\langle\hat{x}^2\rangle + \langle\hat{y}^2\rangle + \langle\hat{z}^2\rangle\Big), \tag{3.13}$$

where the expectation value of an operator $\hat{O}$ for an intrinsic wave function $|\Phi\rangle$ is represented as $\langle\hat{O}\rangle$. The inertia principal axes $\hat{x}$, $\hat{y}$, and $\hat{z}$ are chosen such that

$$\langle \hat{y}^2 \rangle \leq \langle \hat{x}^2 \rangle \leq \langle \hat{z}^2 \rangle, \tag{3.14}$$

$$\langle \hat{x}\hat{y} \rangle = \langle \hat{y}\hat{z} \rangle = \langle \hat{z}\hat{x} \rangle = 0, \tag{3.15}$$

with the constraint

$$\frac{\langle \hat{x}\hat{y} \rangle}{R^2} = \frac{\langle \hat{y}\hat{z} \rangle}{R^2} = \frac{\langle \hat{z}\hat{x} \rangle}{R^2} = 0 \tag{3.16}$$

necessary to satisfy Eq. 3.15 [13].

A constraint potential

$$\begin{aligned} V_{\text{const}} \equiv \eta_1 \Big[(\beta \cos\gamma - \beta_0 \cos\gamma_0)^2 + (\beta \sin\gamma - \beta_0 \sin\gamma_0)^2 \Big] \\ + \eta_2 \left[\left(\frac{\langle \hat{x}\hat{y} \rangle}{R^2} \right)^2 + \left(\frac{\langle \hat{y}\hat{z} \rangle}{R^2} \right)^2 + \left(\frac{\langle \hat{z}\hat{x} \rangle}{R^2} \right)^2 \right] \end{aligned} \tag{3.17}$$

is introduced to the total system energy in the energy variation to obtain the energy minimum state under the constraint condition in Eq. 3.16, where η_1 and η_2 are of sufficiently large values. Thus, the constrained energy $E^{\pm}_{\text{const}}$ is defined as

$$E^{\pm}_{\text{const}} \equiv \frac{\langle \Phi^{\pm} | \hat{H} | \Phi^{\pm} \rangle}{\langle \Phi^{\pm} | \Phi^{\pm} \rangle} + V_{\text{const}}, \tag{3.18}$$

where $\hat{H}$ is the Hamiltonian, to determine $\{X\}$. Once the variation is made on the constraints, the optimized wave function $|\Phi^{\pm}(\beta_0, \gamma_0)\rangle$ are obtained for each set of parameters $(\beta, \gamma) = (\beta_0, \gamma_0)$ [13].

3.2.4 Generator Coordinate Method

To calculate energy levels, the parity and total angular momentum projected AMD wave functions $\hat{P}^J_{MK}|\Phi^{\pm}(\beta, \gamma)\rangle$ are superposed. The final wave function for the $J^{\pm}_n$ state is therefore a linear combination of the basis wave functions:

$$|\Phi^{J\pm}_n\rangle = \sum_K \sum_i f_n(\beta_i, \gamma_i, K)\hat{P}^J_{MK}|\Phi^{\pm}(\beta_i, \gamma_i)\rangle, \tag{3.19}$$

where the coefficients $f_n(\beta_i, \gamma_i, K)$ are determined with the Hill-Wheeler equation,

$$\delta\Big(\Big\langle \Phi^{J\pm}\Big|\hat{H}\Big|\Phi^{J\pm}\Big\rangle - E_n\Big\langle \Phi^{J\pm}\Big|\Phi^{J\pm}\Big\rangle\Big) = 0. \tag{3.20}$$

Therefore, the wave function $|\Phi^{J\pm}_n\rangle$ is the superposition of multiconfigurations described by parity and total angular momentum projected AMD wave functions. In the limit of sufficient basis wave functions on the β-γ plane, $|\Phi^{J\pm}_n\rangle$ corresponds to the Generator Coordinate Method (GCM) with the two-dimensional generator coordinates of the quadruple deformation parameters, β and γ [13].

3.2.5 Hamiltonian

The Hamiltonian $\hat{H}$ mentioned in the previous section is composed of a kinetic term as well as three effective two-body interactions:

$$\hat{H} = \sum_i \hat{t}_i - \hat{T}_G + \sum_{i<j} \hat{V}_{ij}^{\text{central}} + \sum_{i<j} \hat{V}_{ij}^{\text{spin-orbit}} + \sum_{i<j} \hat{V}_{ij}^{\text{Coulomb}}, \tag{3.21}$$

for central force $\hat{V}_{ij}^{\text{central}}$, spin-orbit force $\hat{V}_{ij}^{\text{spin-orbit}}$, and Coulomb force $\hat{V}_{ij}^{\text{Coulomb}}$. The central force is described as

$$\hat{V}_{ij}^{\text{central}} = \sum_{k=1}^{2} v_k \exp\left[-\left(\frac{\hat{r}_{ij}}{a_k}\right)^2 \right] (W + B\hat{P}_\sigma - H\hat{P}_\tau - M\hat{P}_\sigma\hat{P}_\tau), \tag{3.22}$$

the Volkov No. 2 interaction [51], for $v_1 = -60.65$ MeV, $v_2 = 61.64$ MeV, $a_1 = 1.80$ fm, and $a_2 = 1.01$ fm. The spin-orbit term is given by the G3RS interaction [52] as

$$\hat{V}_{ij}^{\text{spin-orbit}} = \sum_{k=1}^{2} u_k \exp\left[-\left(\frac{\hat{r}_{ij}}{b_k}\right)^2 \right] \hat{P}(^3O), \hat{\boldsymbol{L}} \cdot \hat{\boldsymbol{S}} \tag{3.23}$$

a two-range Gaussian with projection operator

$$\hat{P}(^3O) = \frac{1 + \hat{P}_\sigma}{2} \frac{1 + \hat{P}_\tau}{2}, \tag{3.24}$$

for $b_1 = 0.600$ fm, $b_2 = 0.477$ fm, spin exchange operator $\hat{P}_\sigma$, and isosopin exchange operator $\hat{P}_\tau$ [13].

The interaction parameters used in the calculations presented in Ref. [13] are the same as those used in Ref. [23], and they are the same as those adopted in many other studies, including ^{9}Be [53], ^{10}Be [54], and C isotopes [22, 24], save for a small change in the spin-orbit force strength. They are adjusted to reproduce the $\alpha + \alpha$ phase shift, the binding energy of the deuteron, and the $\alpha + n$ phase shift. The width parameter of single-particle Gaussian wave packets in Eq. 3.3 is set to a value of $\nu = 0.235$ fm^{-2}, which is determined from a ^{9}Be ground state variational calculation in Ref. [53].

3.3 Calculations

With the AMD method described in Sec. 3.2, calculations were made for ^{14}C [13]. Positive- and negative-parity state calculations are presented separately.

3.3.1 Energy Surfaces

Variational calculations were made with the $\beta - \gamma$ constraint of the $\beta - \gamma$ plane triangle lattice at 196 mesh points. From these calculations, energy surfaces as functions of β and γ are obtained. Positive-parity surfaces are shown in Fig. 3.1, while negative-parity surfaces are found in Fig. 3.2. In both figures, the top panels show states before the total angular momentum projections, while the bottom panels show states after the projection [13].

In Fig. 3.1, the top panel is called the positive-parity energy surface, and the bottom panel is called the 0^+ energy surface. The positive-parity energy surface's minimum point is located at $(\beta\cos\gamma, \beta\sin\gamma) = (0.00, 0.00)$, indicating a spherical shape. The 0^+ energy

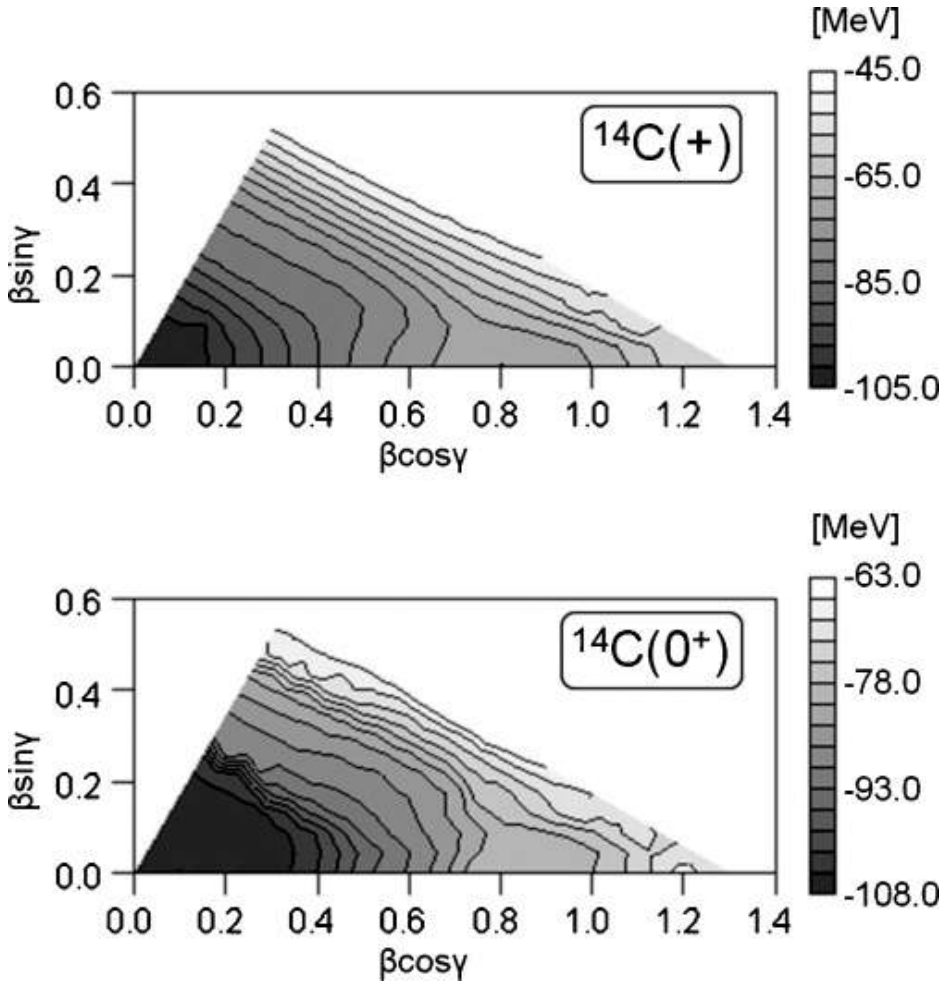

Figure 3.1: Energy surfaces of ^{14}C on the $\beta - \gamma$ plane. The top panel shows the energy for the positive-parity states before the total angular momentum projection and the bottom panel shows that for the 0^+ states after the total-angular-momentum projection. Figure from Ref. [13].

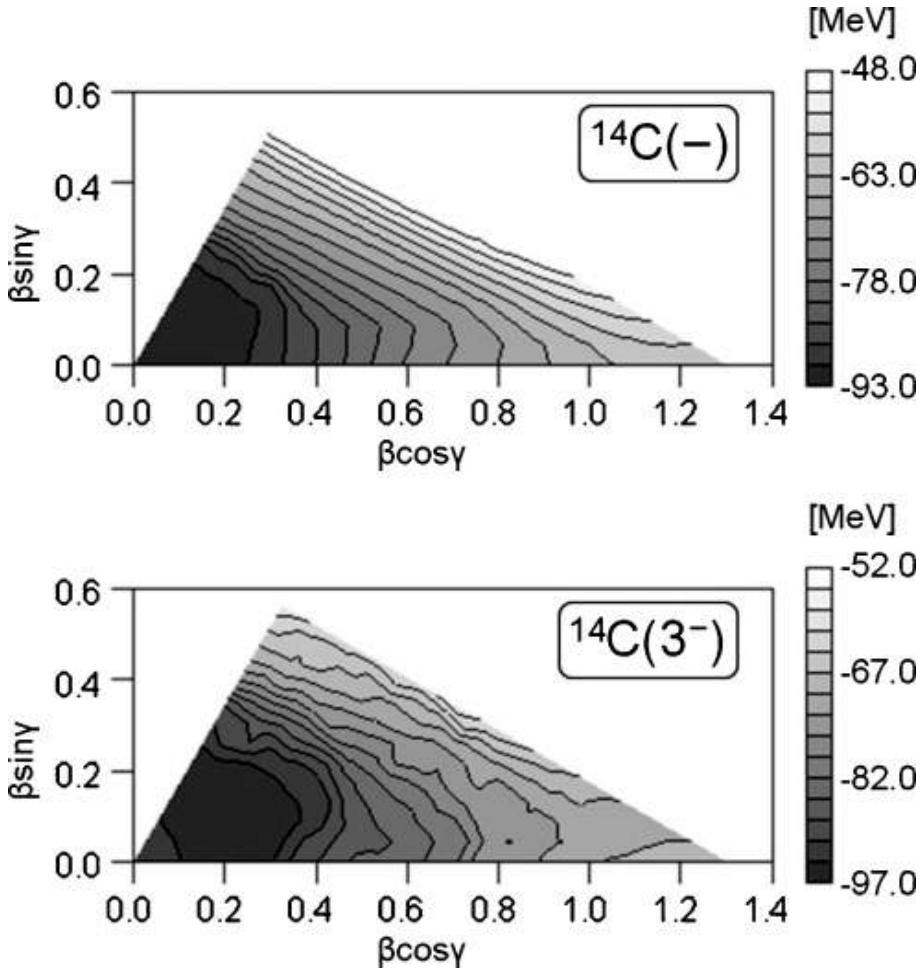

Figure 3.2: Energy surfaces of ^{14}C on the $\beta - \gamma$ plane. The top panel shows the energy for the negative-parity states before the total angular momentum projection and the bottom panel shows that for the 3^- states after the total-angular-momentum projection. Figure from Ref. [13].

surface's minimum point is located at $(\beta\cos\gamma, \beta\sin\gamma) = (0.23, 0.04)$, resulting in a deformation of the energy minimum state from spherical before the projection to triaxial after the projection due to higher correlations beyond the mean field that are incorporated by the projection. Similarly for negative-parity states in Fig. 3.2, the minimum point before projection is $(\beta\cos\gamma, \beta\sin\gamma) = (0.08, 0.04)$ and $(\beta\cos\gamma, \beta\sin\gamma) = (0.20, 0.09)$ after, again changing from nearly spherical to triaxial in shape. While there is a flat region in the 0^+ energy surface near $(\beta\cos\gamma, \beta\sin\gamma) = (0.90, 0.04)$, there is no flat region in the 3^- energy surface. This flat region in the 0^+ energy surface is important since a rotational band with large prolate deformation is constructed by wave functions in this region after the GCM calculation is made, and it is this prolate state that is theorized to be in the form of a linear-chain. No such linear-chain structures are predicted for negative-parity states [13].

3.3.2 β-γ Plane Structures

The intrinsic structures of the ^{14}C states are obtained by the $\beta - \gamma$ constraint AMD. The density distributions of protons and neutrons are analyzed, as is the difference in density between neutrons and protons so that excess neutron behavior can be observed. The densities are defined as

$$\tilde{\rho}(x, z) \equiv \int dy\ \rho(\boldsymbol{r}) \tag{3.25}$$

for

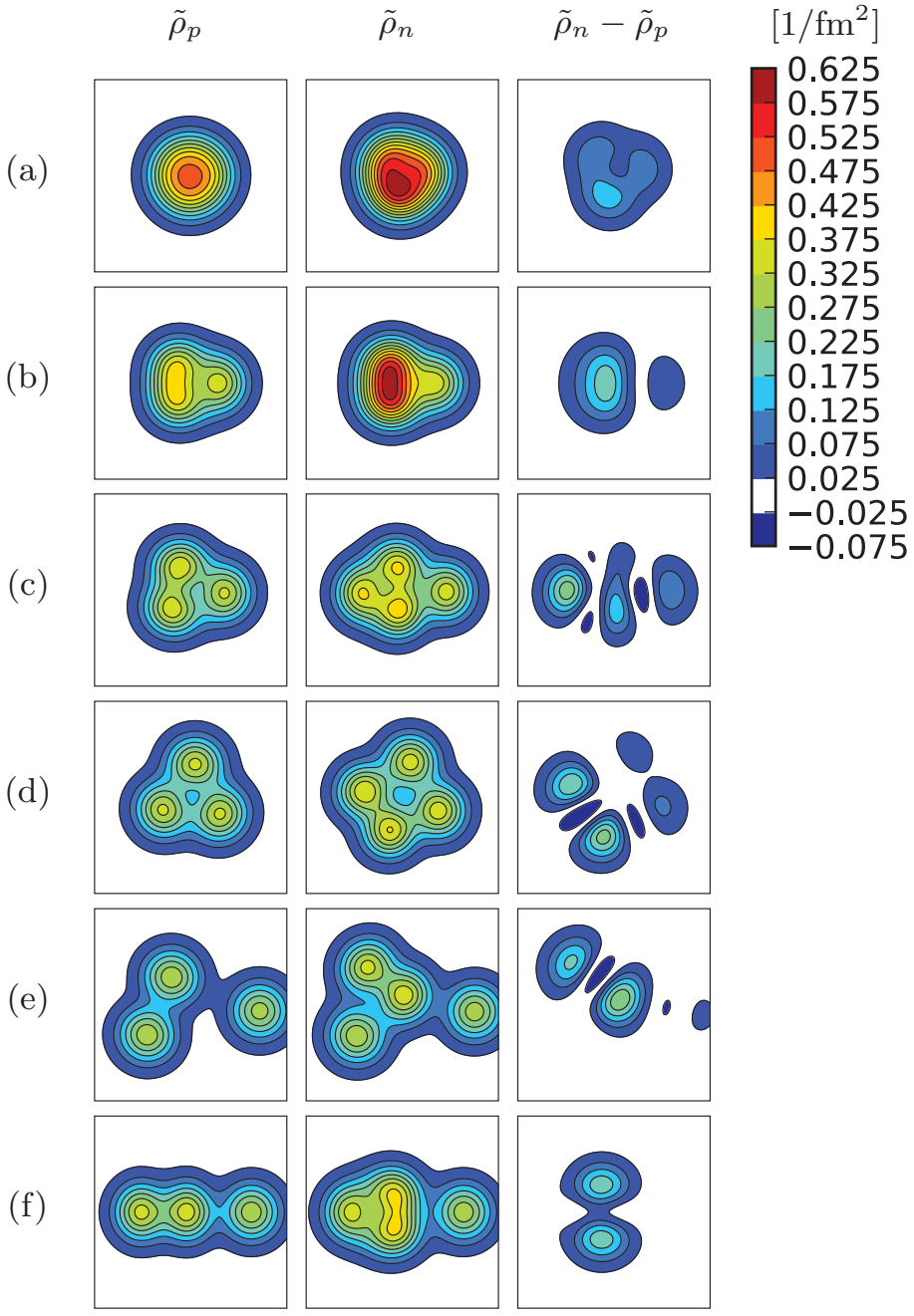

Figure 3.3: Density distributions of the intrinsic wave functions for the positive-parity states of ^{14}C. The proton density $\tilde{\rho}_p$, neutron density $\tilde{\rho}_n$, and difference between the neutron and proton densities $\tilde{\rho}_n - \tilde{\rho}_p$ are illustrated in the left, middle, and right columns, respectively. The density distributions of the intrinsic wave functions at (a) $(\beta\cos\gamma, \beta\sin\gamma) = (0.00, 0.00)$, (b) $(\beta\cos\gamma, \beta\sin\gamma) = (0.23, 0.04)$, (c) $(\beta\cos\gamma, \beta\sin\gamma) = (0.45, 0.17)$, (d) $(\beta\cos\gamma, \beta\sin\gamma) = (0.25, 0.35)$, (e) $(\beta\cos\gamma, \beta\sin\gamma) = (0.78, 0.22)$, and (f) $(\beta\cos\gamma, \beta\sin\gamma) = (0.93, 0.04)$ on the $\beta - \gamma$ plane are shown. The size of the box is 10×10 fm^2. Figure from Ref. [13].

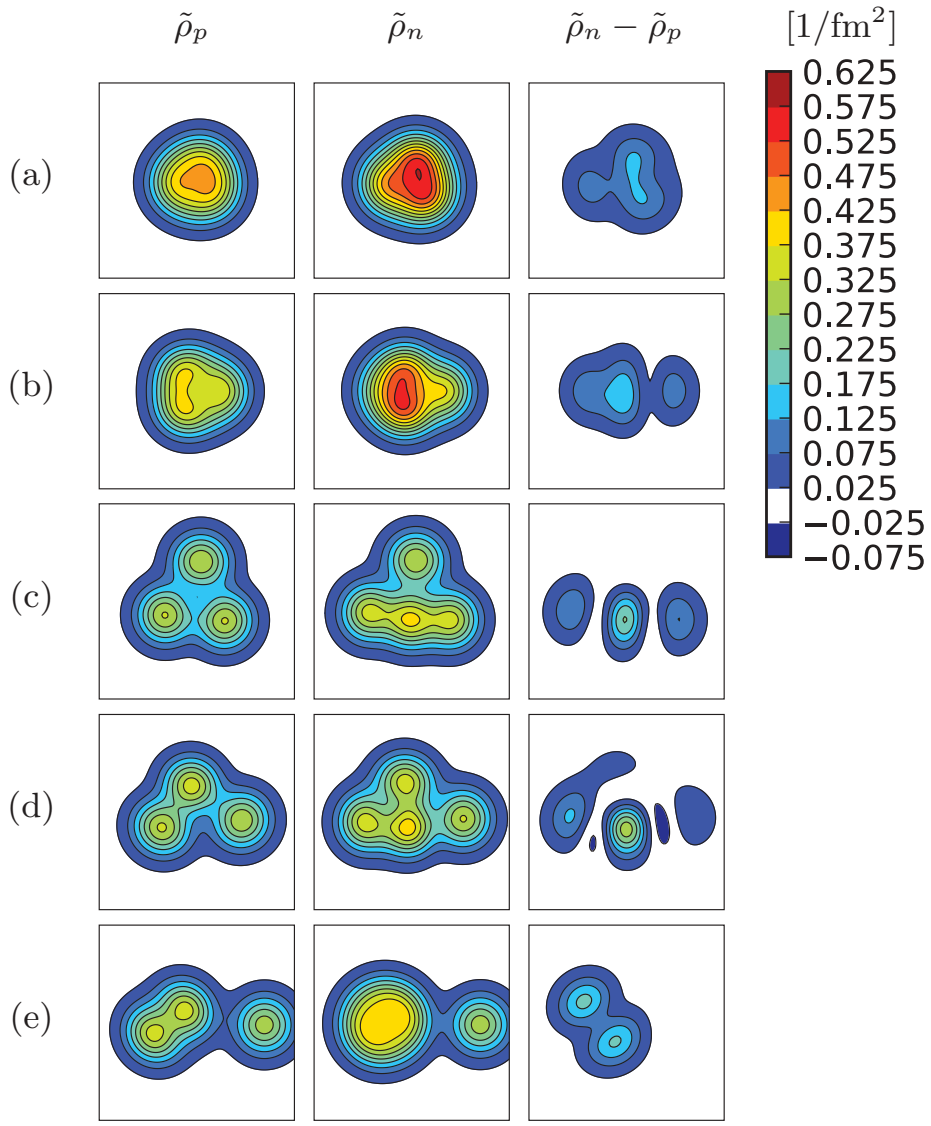

Figure 3.4: Density distributions of the intrinsic wave functions for the negative-parity states of ^{14}C. The proton density $\tilde{\rho}_p$, neutron density $\tilde{\rho}_n$, and difference between the neutron and proton densities $\tilde{\rho}_n - \tilde{\rho}_p$ are illustrated in the left, middle, and right columns, respectively. The density distributions of the intrinsic wave functions at (a) $(\beta\cos\gamma, \beta\sin\gamma) = (0.08, 0.04)$, (b) $(\beta\cos\gamma, \beta\sin\gamma) = (0.20, 0.09)$, (c) $(\beta\cos\gamma, \beta\sin\gamma) = (0.25, 0.35)$, (d) $(\beta\cos\gamma, \beta\sin\gamma) = (0.60, 0.17)$, and (e) $(\beta\cos\gamma, \beta\sin\gamma) = (0.93, 0.04)$ on the $\beta - \gamma$ plane are shown. The size of the box is 10×10 fm^2. Figure from Ref. [13].

$$\rho(\boldsymbol{r}) \equiv \langle \Phi(\beta,\gamma)| \sum_i \delta(\boldsymbol{r} - \hat{\boldsymbol{r}}_i) |\Phi(\beta,\gamma)\rangle. \tag{3.26}$$

The positive- and negative-parity density distributions are shown in Fig. 3.3 and Fig. 3.4, respectively [13].

Of particular interest to the work presented in this dissertation is Fig. 3.3(f), where a linear-chain structure is shown. Such a structure is not seen in Fig. 3.4, indicating that the prolate deformed negative-parity states are different from the prolate deformed positive-parity states, though both show three α-cluster cores with $^{10}\mathrm{Be} + \alpha$ correlation [13].

3.3.3 Energy Levels

Energy spectra are calculated by superposing the $\beta - \gamma$ constraint AMD wave functions at 196 mesh points on the $\beta - \gamma$ plane by using the GCM. Positive-parity states are shown with rotational band assignments in Fig. 3.5 [43], with negative-parity states given in Fig. 3.6 [13].

The GCM calculation results in multiple rotational bands. Consider the rotational band formed by the 0_5^+, 2_6^+, and 4_6^+ states in Fig. 3.5, labeled as band (3). The main component of the band comes from the AMD wave function located at $(\beta\cos\gamma, \beta\sin\gamma) = (0.93, 0.04)$, the linear-chain structure, with 64% overlap in the 0_5^+ state. Due to the large deformation of the linear-chain structure of three α clusters, the band is predicted to have strong $E2$ transitions with $B(E2, 2_6^+ \to 0_5^+) = 67.2\ e^2\ \mathrm{fm}^4$ and $B(E2, 4_6^+ \to 2_6^+) = 88.3\ e^2\ \mathrm{fm}^4$. Since the ratio of these $B(E2)$ values is 1.31, which is consistent with the rigid rotor model value

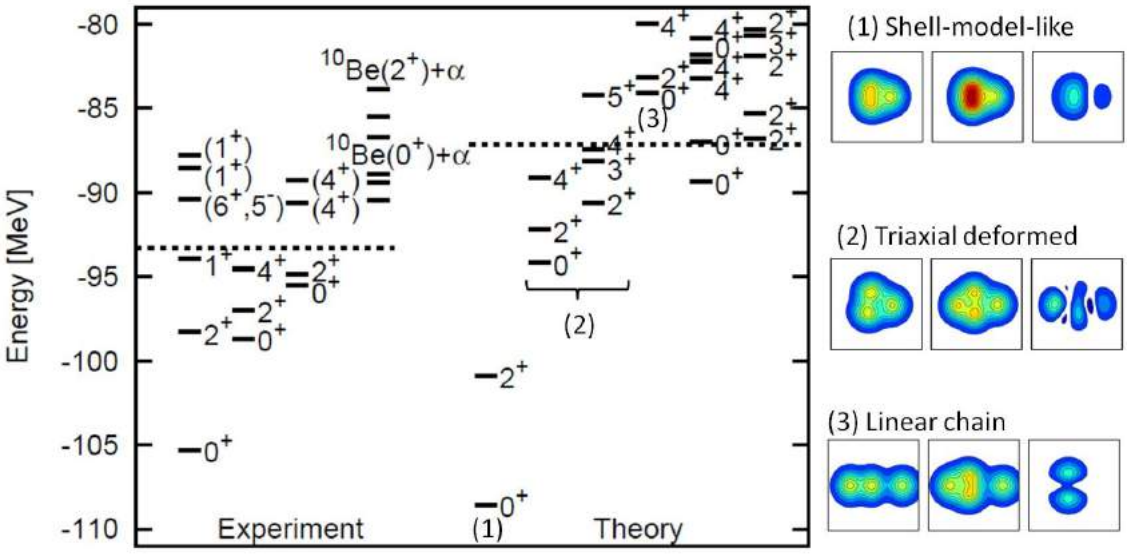

Figure 3.5: Energy levels for the positive-parity states of ^{14}C and the density distributions of the intrinsic wave functions of bands. The dotted lines on the left and right show the experimental and theoretical $^{10}\mathrm{Be} + \alpha$ threshold energies, respectively. The proton density $\tilde{\rho}_p$, neutron density $\tilde{\rho}_n$, and difference between the neutron and proton densities $\tilde{\rho}_n$ - $\tilde{\rho}_p$ are illustrated. Figure from Ref. [43].

of 10/7, this band is considered to be the rotational band of the linear-chain structure with the $^{10}\mathrm{Be} + \alpha$ correlation [13].

3.3.4 Comparison to ^{12}C and Discussion of Excess Neutrons

In ^{12}C, no similar linear-chain rotational band is predicted; only the 0^+_3 state has a linear-chain configuration in this model [13], while an entire rotational band exists in ^{14}C. The existence of triaxial bands in ^{14}C is essential to the appearance of the positive-parity linear-chain band since they prevent the linear-chain band from bending due to orthogonality. The states that prevent bending in the 2^+ and 4^+ states in ^{14}C, however, do not exist in ^{12}C. In fact, the excess neutrons found in ^{14}C are essential for constructing the triaxial bands that prevent bending [13].

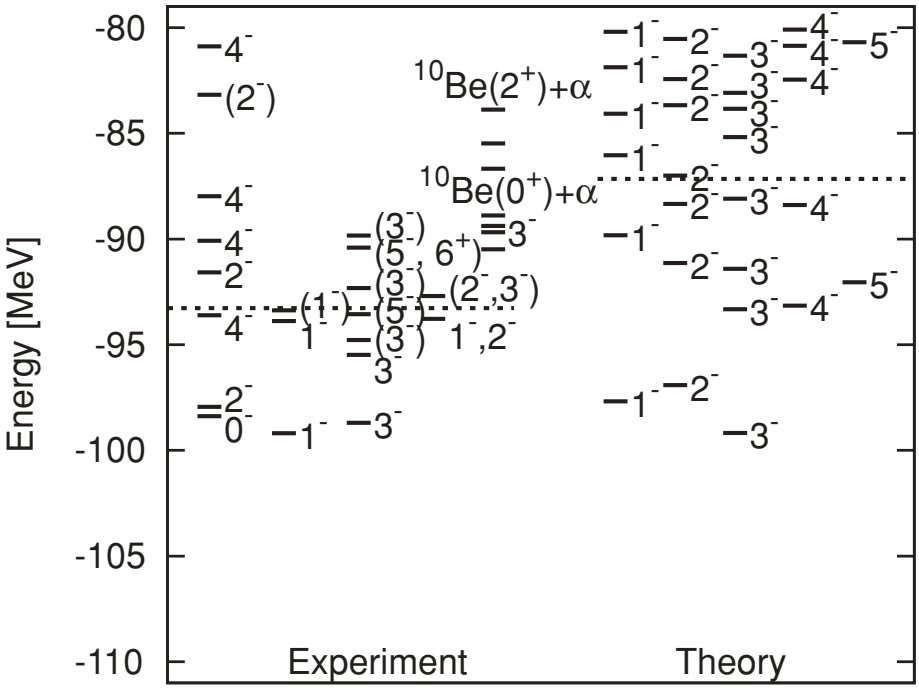

Figure 3.6: Energy levels of the negative-parity states in ^{14}C. The five columns on the left are the experimental data and the five columns on the right are the calculated results. The dotted lines on the left and right show the experimental and theoretical $^{10}\mathrm{Be} + \alpha$ threshold energies, respectively. Figure from Ref. [13].

Calculations from Ref. [24] imply that the linear-chain state is perhaps unstable in ^{14}C. Their work shows that the linear-chain is unstable against the bending mode due to the lack of a local minimum in the energy curve. The work presented in Ref. [13], however, takes into account the orthogonality to lower states in their GCM calculations. Further, the work in Ref. [24] assumes the three α clusters are separated by equal distances with the excess neutrons occupying an orbital moving around the 3α core. The β-γ Constraint AMD + GCM used in Ref. [13] makes no assumptions on the clustering of α particles. The various $3\alpha + 2n$ structures they obtain are a result of their energy variation method, with a preference for a $^{10}\mathrm{Be} + \alpha$ configuration.

The $^{10}\mathrm{Be} + \alpha$ structure of ^{14}C was first proposed in Ref. [25], and a parity doublet linear-chain band is predicted. The work of Ref. [13] only predicts a positive-parity band, as the ^{10}Be core can easily rotate in the negative-parity $^{10}\mathrm{Be} + \alpha$ states, which results in strong mixing of the linear-chain structure with bending $^{10}\mathrm{Be} + \alpha$ configurations. Also, the band predicted in Ref. [25] is below the $^{10}\mathrm{Be} + \alpha$ threshold, while it is above threshold in Ref. [13].

3.4 Relation to Current Work

By the $^{10}\mathrm{Be}+\alpha$ entrance channel chosen in the present work, structures of the type $^{10}\mathrm{Be}+\alpha$ in ^{14}C clearly appear. These resonances in ^{14}C are investigated in this work and are compared to the model predictions of Ref. [13].

Chapter 4

Experiment

The experimental data described in this work were collected at the University of Notre Dame's Nuclear Science Laboratory over a two-week span in October, 2011. The device and electronics were set up and installed from October 11 to October 22, 2011. Beam tuning and electronics setup were completed from October 22 to October 25. Finally, physics data were collected from October 25 to October 31.

This chapter will discuss details of the beam facility at Notre Dame, the experimental setup and detailed design of the prototype AT-TPC, and the data collection process.

4.1 Beam Facility

The Nuclear Science Laboratory is part of the University of Notre Dame's Institute for Structure and Nuclear Astrophysics, or ISNAP. The first accelerator for use in nuclear physics research was built in the 1930's on the campus, and the university has continued to produce active research in the field ever since [56].

With the use of the Multi-Cathode Source of Negatives Ions by Cesium Sputtering (MC-SNICS) ion source at ISNAP [57], a primary beam of ^{11}B was extracted from a ^{11}B + Ag ion source. Of the two accelerators available at ISNAP, the FN Tandem Van de Graaff accelerator [58] was used to accelerate the ^{11}B primary beam. The FN delivered the primary beam to TwinSol, a low-energy radioactive nuclear beam (RNB) apparatus [55], where it

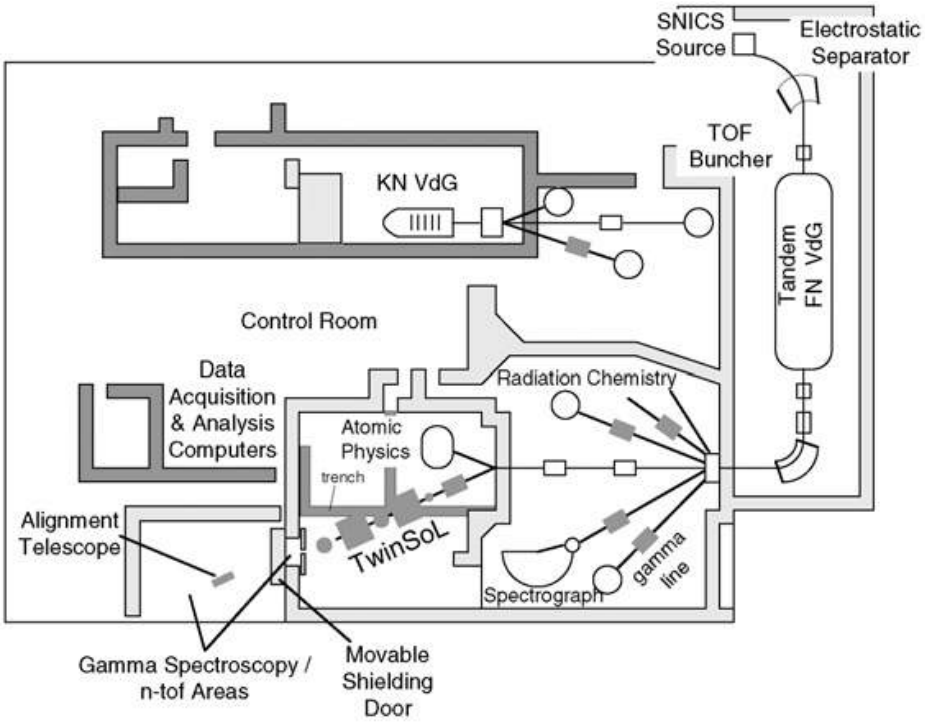

Figure 4.1: Part of the beam-line layout at the University of Notre Dame's Nuclear Science Laboratory. During this work, the prototype AT-TPC was located in the vault to the left of, or beyond, TwinSol. Figure from Ref. [55].

impinged upon ^{13}C foils, from which a secondary beam of ^{10}Be was extracted. The secondary ^{10}Be beam was then delivered to the prototype AT-TPC, where reactions between the ^{10}Be beam particles and target α particles were measured. A schematic showing the beam-line from starting from SNICS and ending at the end of TwinSol is shown in Fig. 4.1.

The three apparatuses mentioned above, in addition to the prototype AT-TPC, are described below.

4.1.1 MC-SNICS Ion Source

For the experiment conducted in this work, a primary beam of ^{11}B was extracted from the MC-SNICS Source at the University of Notre Dame's Nuclear Science Laboratory. An

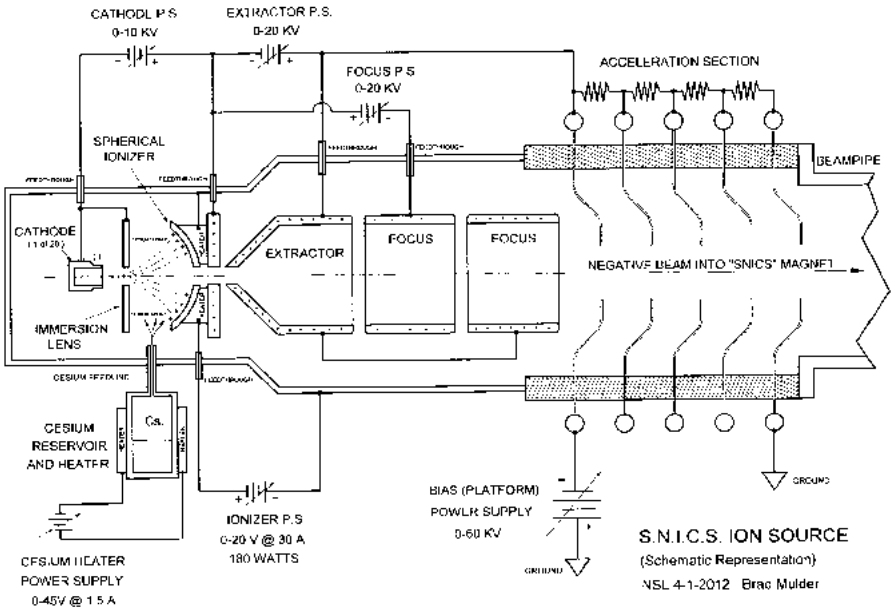

Figure 4.2: A schematic drawing of the MC-SNICS Source at the Nuclear Science Laboratory. Figure courtesy Brad Mulder.

example of a sputter ion source, MC-SNICS, or Multi-Cathode Source of Negatives Ions by Cesium Sputtering [57], is the primary ion source for the FN Tandem Van de Graaff accelerator. Fig. 4.2 shows a schematic of MC-SNICS.

Multiple identical ion source cathodes, in this case $^{11}\mathrm{B}$ + Ag cathodes, are loaded onto a cathode wheel. This wheel, which comes in both 20- and 40-cathode options, is of great convenience to the operation of MC-SNICS; the cathode wheel can be rotated remotely under vacuum as it allows for multiple cathodes to be available for use without opening the device, greatly lessening the amount of time needed to switch from a spent cathode to a new one [57].

Once a cathode is in place and the device is under vacuum, a cesium reservoir is heated to 90 °C [57]. A vapor is formed, and gaseous cesium atoms condense on both a heated spherical

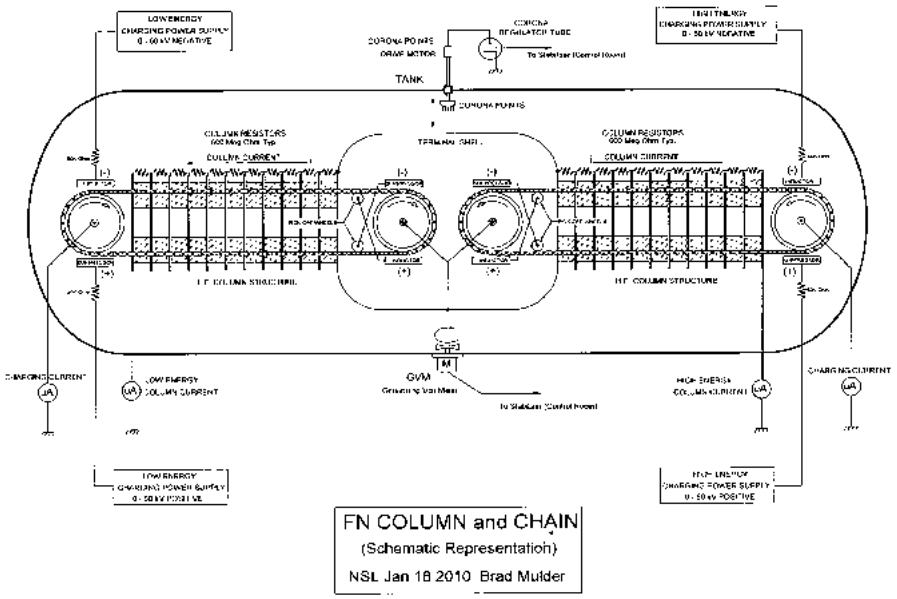

Figure 4.3: A schematic drawing of the FN Tandem Van de Graaff accelerator at the Nuclear Science Laboratory. Figure courtesy Brad Mulder.

ionizer and the cathode surface. Those on the ionizer are quickly boiled off, stripping them of an electron. These positively charged ions are then attracted to the negatively-charged cathode and focused onto the cathode with an immersion lens, where they impact the source material and cause the material to be sputtered, including the desired ^{11}B. Some of the ^{11}B atoms gain an electron as they pass through the cesium that coats the cathode, allowing the now-negatively charged ^{11}B to be extracted out of the source and focused and accelerated towards the FN Tandem Van de Graaff accelerator [57].

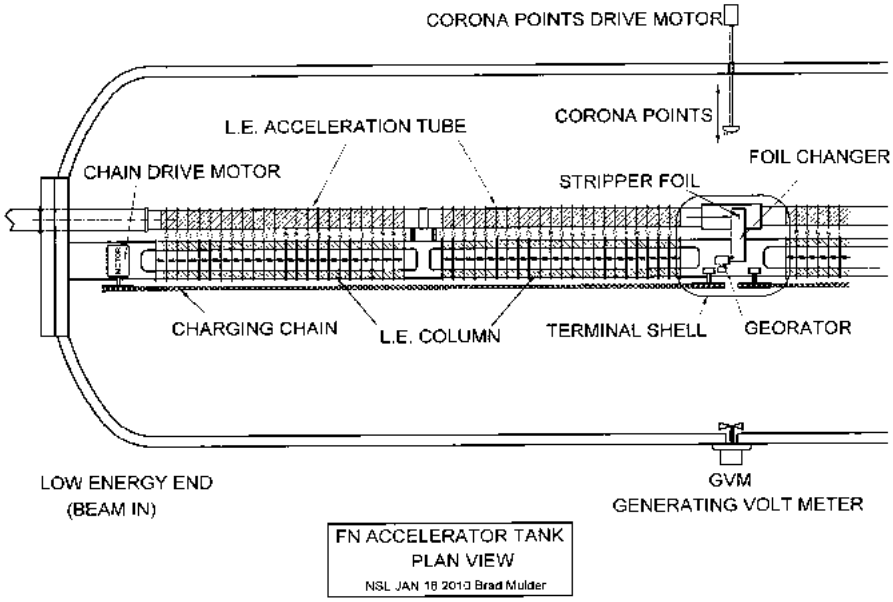

Figure 4.4: A schematic drawing of the FN Tandem Van de Graaff accelerator at the Nuclear Science Laboratory with included detail on the stripper foil mechanism. Figure courtesy Brad Mulder.

4.1.2 FN Tandem Van de Graaff Accelerator

As the ^{11}B ions exit the MC-SNICS ion source, they are transported to the FN Tandem Van de Graaff accelerator. The FN Tandem is 40 ft long and 12 ft in diameter and can be operated at voltages of up to 10 MV [58]. It is shown in Fig. 4.3.

The ^{11}B ions enter the FN Tandem in a 1^- charge state. At the center of the FN Tandem is a terminal, a metal electrode held up to a high voltage of +10 MV. This terminal attracts the negatively charged ^{11}B ions [58]. As the ions approach the terminal, they travel down the FN column. This column focuses the charged ions, provides a vacuum for the ions to travel in, and acts as mechanical support to hold the terminal in place in the center of the FN Tandem by highly compressing it from either side. The part of the column where the

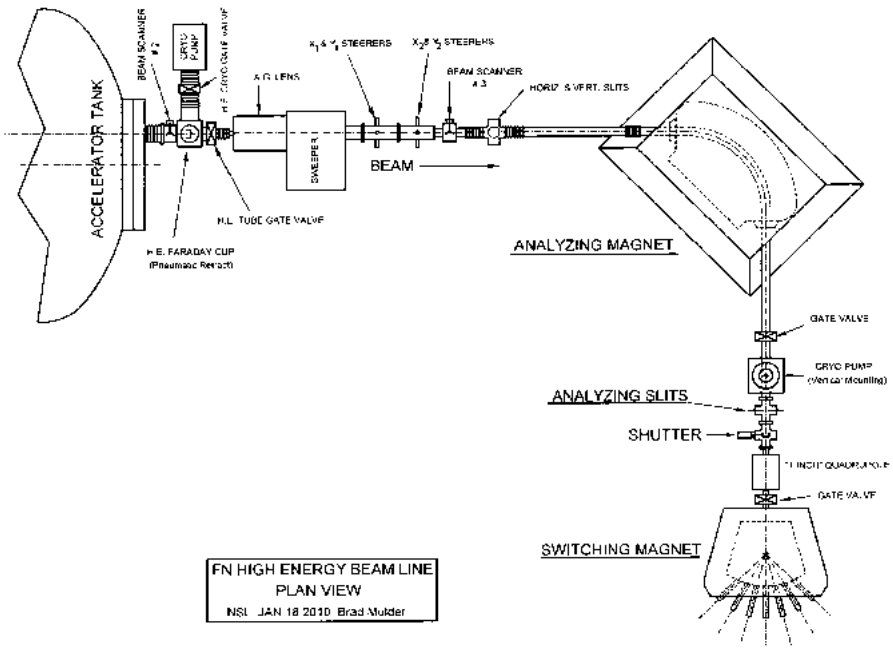

Figure 4.5: A schematic drawing of the beam line including the FN Tandem Van de Graaff accelerator and analyzing magnet at the Nuclear Science Laboratory. Figure courtesy Brad Mulder.

1^- ^{11}B ions travel is called the low energy, or LE column. The other half is called the high energy, or HE column [58].

Upon entering the terminal shell, the 1^- ^{11}B ions traverse a stripper foil, as seen in Fig. 4.4. This foil, made of 3 μg/cm^2 carbon, is used to remove electrons from the ^{11}B ions, thus making it a positively-charged ion [58]. Multiple charge states may be produced; in this work, fully-stripped ^{11}B was desired. Thus, with a charge state of 5^+, an energy of up to 60 MeV is achievable.

The positive ^{11}B ions, which are now completely free of electrons, accelerate away from the terminal through the HE column. As various charge states may have been produced in the FN Tandem, and other contaminants from MC-SNICS may also be present, the nuclei

are sent from the FN Tandem to an analyzing magnet to be sorted (Fig. 4.5). The magnitude of the field in the analyzing magnet is tuned to only accept nuclei of the desired magnetic rigidity; other beam particles are stopped [58]. The beam slits at the exit of the analyzing magnet provide a signal to stabilize the high voltage at the terminal of the accelerator. The chosen nuclei are then sent further down the beam-line to TwinSol.

4.1.3 TwinSol

In front of the TwinSol device, the beam impinges on the production target at a beam current of about 1 μA. For this work, ^{13}C foils were used as the production target. The enriched ^{13}C foils were supplied by the Arizona Carbon Foil Co., Inc. and assembled to target frames at the NSCL using the fishing technique on water. A stack of four 100 μg/cm^2 ^{13}C foils was chosen as no single 400 μg/cm^2 ^{13}C foil was commercially available. The beam of ^{10}Be nuclei formed at the production target, referred to as the secondary beam, is then sent through TwinSol.

TwinSol is a twin superconducting solenoid magnet low-energy radioactive nuclear beam (RNB) apparatus [55]. The magnet is a 6 T superconducting solenoid comprised of two "lenses," the twin magnets in the device, as shown in (Fig. 4.6), which focus the just-produced secondary beam and deliver it to an experimental detector [55].

There are two configurations in which TwinSol is operated: parallel mode and cross-over mode (Fig. 4.7). In cross-over mode, the first magnet focuses the secondary beam between it and the other magnet where either an aperture and/or an energy loss absorber is used to further purify the secondary beam [55]. In parallel mode, the beam is not focused between the magnets. Additionally, an absorber may be placed between the magnets to stop unwanted neutrons from passing down the beam-line through TwinSol. In both modes, the

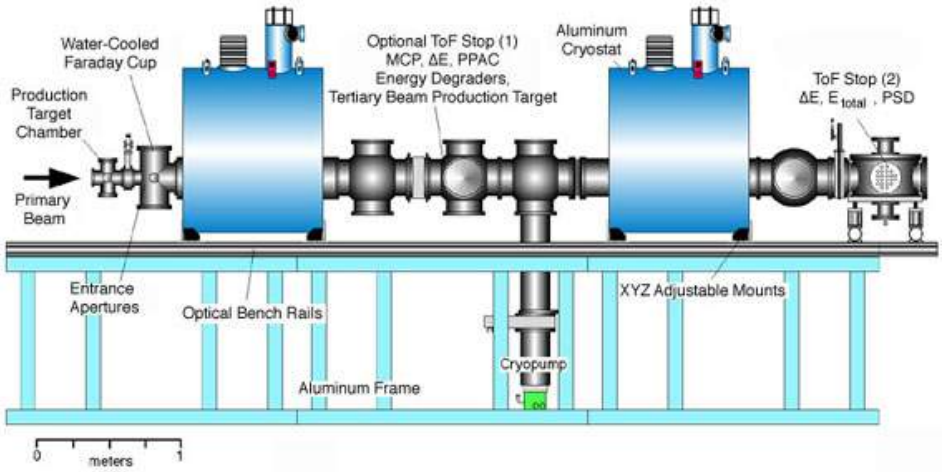

Figure 4.6: A schematic drawing of TwinSol at the Nuclear Science Laboratory. Figure from Ref. [59].

secondary beam is focused after the second magnet in TwinSol to the entrance window of the experimental detector [55], which in this case is the prototype AT-TPC. The direct beam is blocked by a beam stopper or slits. Between TwinSol and the prototype AT-TPC entrance window is a beam steerer, which aids in the focusing of the beam onto the window. In the experiment described in this work, TwinSol was operated in parallel mode.

4.2 Design of the Prototype AT-TPC

Before discussing how the prototype AT-TPC was installed and used at the Nuclear Science Laboratory for this work, the design of the device will be described in detail. The device's most basic components are the exterior chamber, the field cage, the corona ring, the Micromegas, and the readout electronics. A schematic of the device is given in Fig. 4.8. It was built to test the essential components of the AT-TPC at a smaller scale (1:2) for lower cost. Much of the discussion in this section is based on Ref. [27], which additionally provides information on the commissioning of the prototype AT-TPC.

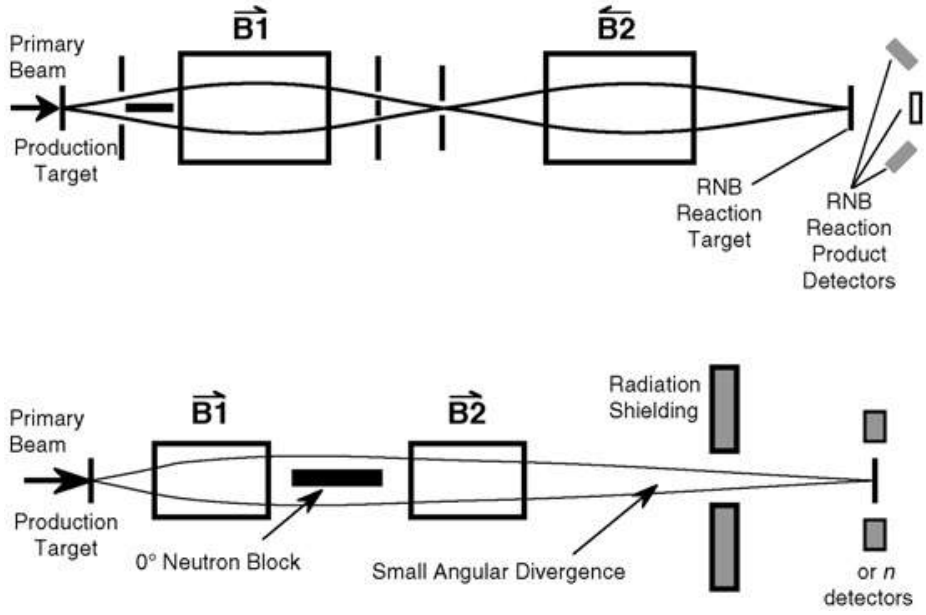

Figure 4.7: Schematic drawings of the two modes of operation of TwinSol. The top image shows cross-over mode, while the bottom is of parallel mode. Figure from Ref. [55].

The exterior chamber of the detector is 70 cm long and 40 cm in diameter, and contains a cylindrical field cage measuring 50 cm in length and 28 cm in diameter, which is centered on the beam axis. The field cage is filled with a gas, which acts as an active target as well as a tracking medium. A 3.7 μm thick para-aramid foil is used as the beam window into the device to separate the vacuum of the beam line ($\sim 10^{-5}$ torr) from the gas that fills the detector ($\sim$ 1 atm = 760 torr). This foil thickness can also be expressed as 0.536 mg/cm^2 given para-aramid's density of 1.45 g/cm^3. Incident beam particles pass through this window and enter the active target gas in the field cage [27].

The beam particles can collide with target gas nuclei, resulting in a nuclear reaction. Both the beam nuclei and the reaction products, being charged particles, ionize the gas. Due to the applied electric field, the freed electrons drift to the Micromegas, which amplifies the electron signal and allows for the reconstruction of the trajectories of the charged particles

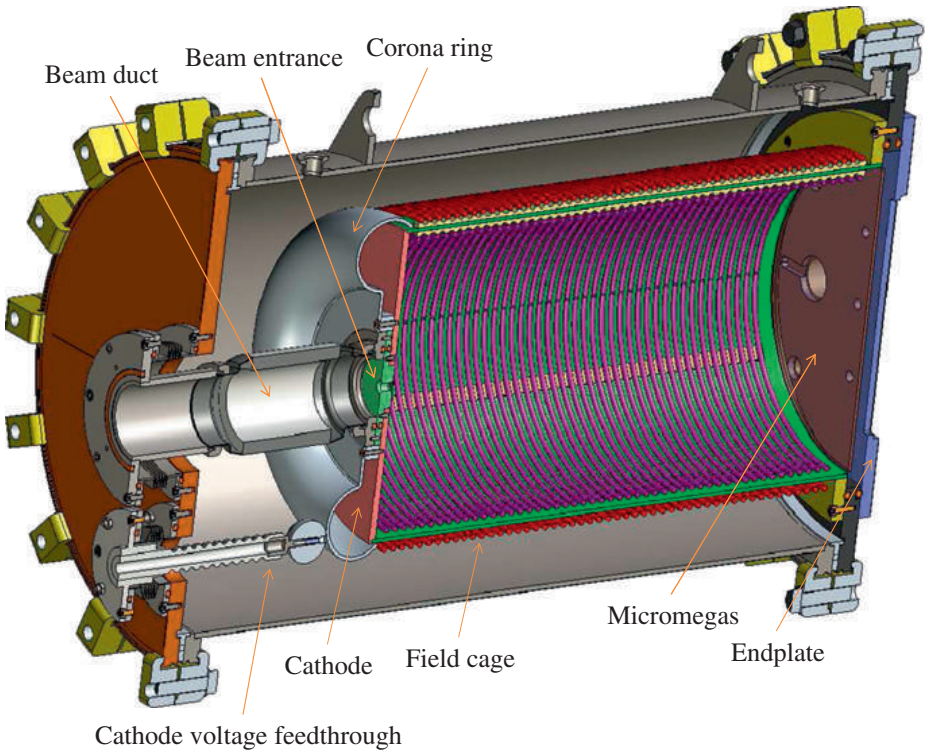

Figure 4.8: Cross-sectional view of the prototype AT-TPC. Figure from Ref. [27].

[27]. For a more general discussion of both the active target and TPC concepts, see the previous descriptions in Section 2.2.

The following subsections will go into detail on each of the prototype AT-TPC's basic components.

4.2.1 Exterior Chamber

A stainless steel design, the outer chamber of the detector is cylindrical in shape and is 70 cm long with a 40 cm diameter, as shown in Fig. 4.9. ISO 400 flanges are mounted on each end of the chamber. The chamber houses the cathode, field cage, and Micromegas, described later in this chapter. Inside of the chamber, a bellows is used to attach the upstream flange to the beam duct and cathode high-voltage feedthrough. The difference in length between the

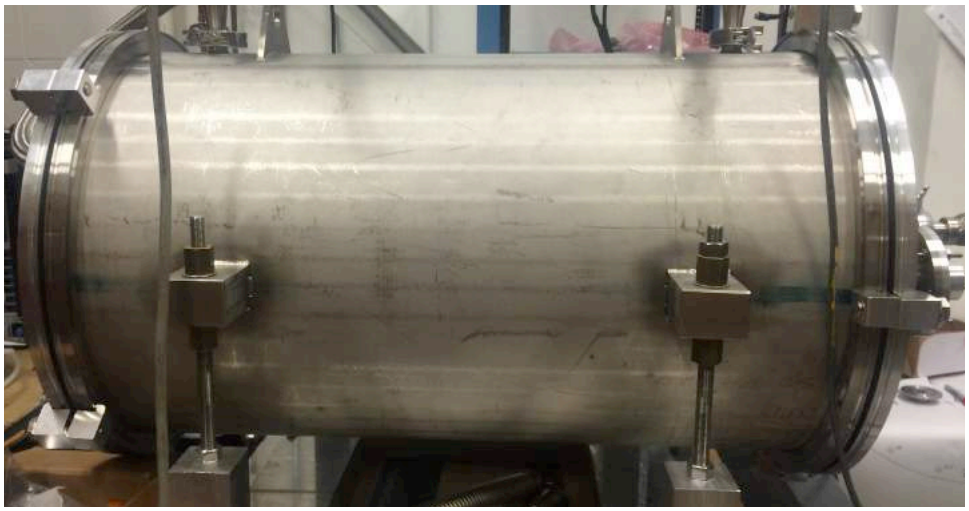

Figure 4.9: Image of the exterior chamber of the device. It's 70 cm in length and has a 40 cm diameter.

chamber and its internal components makes the bellows a practical choice for this situation [27].

On the other end of the chamber, the downstream flange serves both as an endplate for mounting the Micromegas and as a piece to secure the field cage inside the chamber, which is done in such a way to allow for the Micromegas to be removed without dismounting the field cage. A feedthrough on the endplate allows for anode signals from the Micromegas to be relayed directly to exterior electronics, minimizing the addition of noise to the signal between the anode and the preamplifiers. A gas inlet and a gas outlet are mounted on the endplate for flowing the target gas through the field cage, as well as a KF40 flange with four SHV feedthroughs. These SHV feedthroughs provide connections to a thermocouple used to measure the gas temperature, supply bias and grounding and monitor the voltage divider circuit of the field cage, and supply the bias voltage and readout the signal from the micromesh of the Micromegas [27]. An image of the downstream flange is given in Fig. 4.10.

4.2.2 Field Cage

Inside of the exterior chamber is the cylindrical field cage, which is 50 cm long and 28 cm in diameter. The purpose of the field cage is twofold: it provides both (1) a gas-tight volume in which the active target gas can be filled and thus where nuclear reactions can take place and

Figure 4.10: Image of the downstream ISO 400 flange. Readout electronics for the Micromegas are mounted on the vertical feedthroughs on the center of the flange. On the left of the flange, there are the both a gas inlet and outlet, as well as a KF40 flange with four SHV feedthroughs.

(2) an interior and exterior surface on which to mount equipotential rings that step down the voltage of the cathode across of the entire active target volume, allowing for a uniform electric field that guides ionization electrons to the Micromegas. The direction of the field is anti-parallel to the direction of the beam [27].

While the target for this work is ^{4}He, CO_2 is added as a quenching gas to stabilize the operation in practice and to increase the dielectric strength of the target gas [27]. At 1 atm, pure helium gas has a dialectic strength of about 5 kV/cm, much lower than that of the nitrogen insulation gas (34 kV/cm) and CO_2 (28 kV/cm) [60]. The ratio of He to CO_2 is 9 to 1, resulting in a net dielectric strength of 7.3 kV/cm, as the strengths add linearly [60].

In addition to the active target gas that fills the field cage, a second gas between the field cage and exterior chamber is also present. This gas serves as insulation to avoid discharge from the cathode to the exterior chamber. Thus, a gas with a high dielectric strength, such as nitrogen, is used as the insulating gas [27].

The field cage is made of grade G10 non-conducting glass reinforced epoxy laminate, both for its high mechanical strength and low outgassing characteristics. While not flame resistant like FR4, G10 is not doped with bromine, the flame resistant material found in FR4. As bromine can be be a strong source of electron absorption when diffused into the the gas volume, G10 was used [27].

An aluminum flange is glued to the downstream end of the field cage, securing the field cage to the endplate of the exterior chamber. On the upstream flange is glued a cathode plate. Both the aluminum flange and cathode plate are hermetically sealed with an epoxy resin glue, ensuring that the target gas inside of the field cage and the insulating gas outside of it do not mix [27].

The design of the field cage does not allow for a large pressure differential between the inside and outside of the field cage. A large differential could result in the breaking of the seals on the end of the field cage or substantial damage to the mechanical integrity of the field cage itself. To protect the field cage in such a scenario, a thin polypropylene foil of thickness 70 μg/cm^2 is located between the two gas volumes. A high pressure differential would then break the foil, allowing the pressures the quickly equilibrate before any damage to the field cage could occur. The foil is located outside of the exterior chamber in a piece of vacuum tubing that bypasses the inner and outer gas volumes. This location makes replacement of the foil straightforward and simple. The foil is held in place in a KF25 flange, and its differential pressure limit was measured to be about 0.1 atm [27].

As mentioned above, equipotential rings are mounted on the field cage, as shown in Fig. 4.11. The rings serve as electrodes, connected via a series of resistors, that step the voltage provided from the cathode at the front of the field cage down to zero at the opposite end of the field cage where the Micromegas are located. The interior and exterior surfaces of the cage each have 50 rings mounted on them, for a total of 100. The electrodes all are made of aluminum rod with a cross-sectional diameter of 0.5 cm. The interior rings have a diameter of 26.0 cm while the exterior rings are 29.5 cm across. The spacing between neighboring rings is about 1 cm [27].

All rings are supported by both aluminum pin stands (Fig. 4.11a) and two additional G10 supports (Fig. 4.11b). The stands and supports are grooved into a V-shape, into which the rings can snap into place. Once in place, the rings are self-supporting. Interior and exterior rings are located at the same position along the field cage axis, and secured into place at the opposite ends of the aluminum pin stand. The stands are secured to the field cage with an epoxy resign glue and are thus hermetically sealed [27].

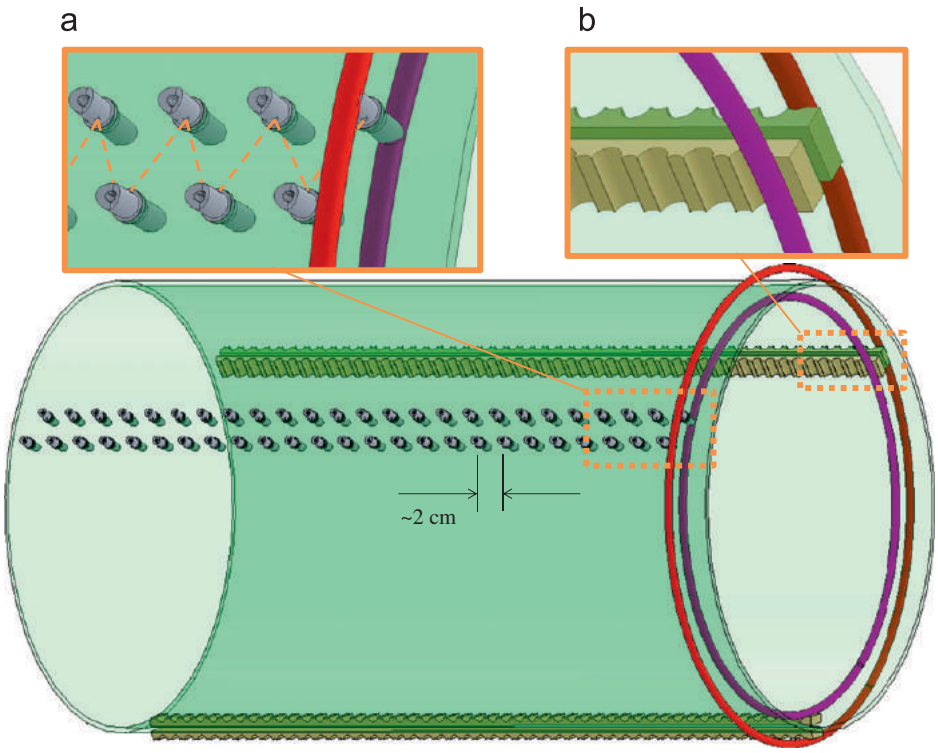

Figure 4.11: Schematic view of the field cage with equipotential rings. For presentation purposes, only one pair of inner (purple and smaller) and outer (red and larger) rings are shown. The equipotential rings are secured to the main frame by (a) the aluminum pin stands and (b) the supports of G10. The pin stands are arranged in a zigzag pattern to increase the inter-stand distance and to reduce the risk of sparking. Resistors are installed along the dashed lines between neighboring stands to step down the potential by voltage division. The stands bore through the G10 tube to put the inner and outer rings at the same potential. The joints between the stands and the tube are hermetically sealed by epoxy resin. Figure from Ref. [27].

In order for the position uncertainty of the electrons that drift down the field parallel to the beam axis to be at most 2 mm radially, or the spatial bin size of the Micromegas anode strips described below in Section 4.2.4, the field non-uniformity must be below 1%. Mounting the rings in the double-array structure described above helps to reduce to field non-uniformity to the required 1% [27].

Starting from the cathode, the electric potential is stepped down the rings via voltage division with a series of resistors. Each ring is connected to its neighbors by a 20 MΩ

resistor. The first ring is also connected to the cathode by a 20 MΩ resistor. The resistors are connected across the pin stands on the outside of the field cage. They are represented by dashed lines in Fig. 4.11a. Each pair of interior and exterior rings for a given pin stand are thus held at the same potential. Note that the pin stands are arranged in a zigzag pattern to lower the sparking risk between stands. The last downstream ring is connected to the exterior chamber with a terminating resistor. The resistance of the terminator is chosen such that the electric field remains uniform all the way to the micromesh of the Micromegas, which is held at a negative potential [27]. For this work, the cathode was held at -40 kV and the micromesh at -245 V, and a terminator with a resistance of 25.5 MΩ was used.

Garfield code [61] was used to simulate the electric field inside of the device [27]. The code is limited to simulations of two-dimensional geometries, and therefore an infinite box with a cross-section equivalent to that of the exterior chamber was used as an approximation. Further, the rings and cathode plate were approximated in the simulation as an assembly of infinitely long wires. Fig. 4.12 shows the equipotential surfaces produced by the code. These surfaces reveal a very uniform field inside of the interior rings, located near a radius of 13 cm in the figure. The uniformity is achieved by the screening of electric field lines from the grounded exterior chamber at about 20 cm in radius by the outer and inner rings [27].

4.2.3 Cathode

An important feature of the prototype AT-TPC is its 1 kV/cm electric field. Such a high field both limits the dead time of the detector, results in fast responses from it, and limits the longitudinal and lateral diffusion straggling. To generate this field, a negative potential of up to -50 kV is held on the cathode of the prototype AT-TPC and then stepped down the

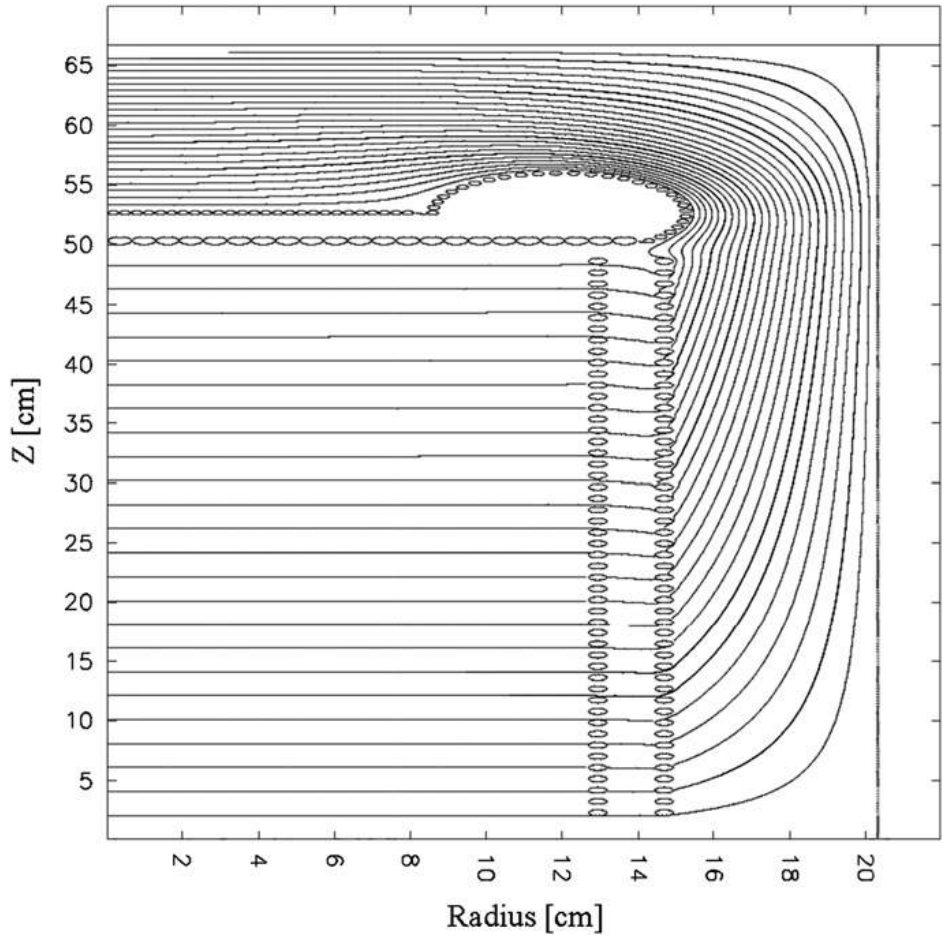

Figure 4.12: Electric field simulations by the Garfield code [61]. The cylindrical detector volume is approximated by an infinite box with the same cross-sectional geometry. Equipotential surfaces are plotted by the solid lines as a function of the radius with respect to the symmetry axis (Z). The cathode plate is located at $Z = 50$ cm. Along the horizontal radius axis, the inner rings are located near 13 cm, the outer rings near 15 cm, and the exterior chamber wall near 20 cm. Figure from Ref. [27].

equipotential rings [27], as described above. As mentioned previously, the cathode plate is glued on the upstream flange of the field cage.

Even though the insulating gas between the field cage and exterior chamber has a dielectric strength that is much greater than the voltage on the cathode, sharp edges or other pointed structures of conducting material can greatly increase the field gradient, causing a large non-uniformity in the field. Since the cathode plate itself has sharp edges, the design

must limit its contribution to field non-uniformity. Thus, a corona ring is used, shown in Fig. 4.8. Built out of aluminum by Ross Engineering, Inc., the corona ring has a diameter of 30 cm and is toroidal in shape, hence its name. Part of the toroid is cut away such that the ring encloses the edges of the cathode plate, providing better shielding of the edges. The cross-sectional diameter of the ring is 3.8 cm; a diameter this large ensures that the electric field on the corona ring surface is below the discharge threshold of the insulation gas. The ring's maximum voltage is rated at 130 kV in air [27].

A cathode voltage feedthrough mounted on the upstream flange of the exterior chamber allows for the voltage to be fed to the cathode from a power supply, as seen in Fig. 4.8. The feedthrough is custom-made and based on the feedthrough used for the beam deflector of the NSCL's K500 cyclotron. It has a maximum 80 kV rating. The feedthrough consists of a hollow cylinder made of machined Macor, an insulating ceramic material. The radius of the surface of the cylinder varies in thickness from 3 to 6 mm in an alternating wavy pattern. The cylinder guides the power cable of the voltage supply to a conducting tip located at the end of the cylinder. Via a conducting spring, this tip is connected to a 3.8 cm wide aluminum sphere that is in contact with the corona ring, which is held at the same potential as the cathode plate [27].

In order to allow beam particles to enter the field cage, a beam duct is located between the upstream flange of the exterior chamber and the cathode plate. The duct is made of alumina ceramic tubing and is 93 mm long with a 64 mm inner diameter and is built from a CeramTec vacuum isolator. It has a 60 kV maximum voltage rating. The entrance window is a hole 7.6 mm in diameter which is centered on an aluminum plate of thickness 12.7 mm that is located at the interface of the duct and cathode plate. The duct itself if hermetically sealed from all other volumes of the device [27]. Over the entrance window, epoxy resin is used

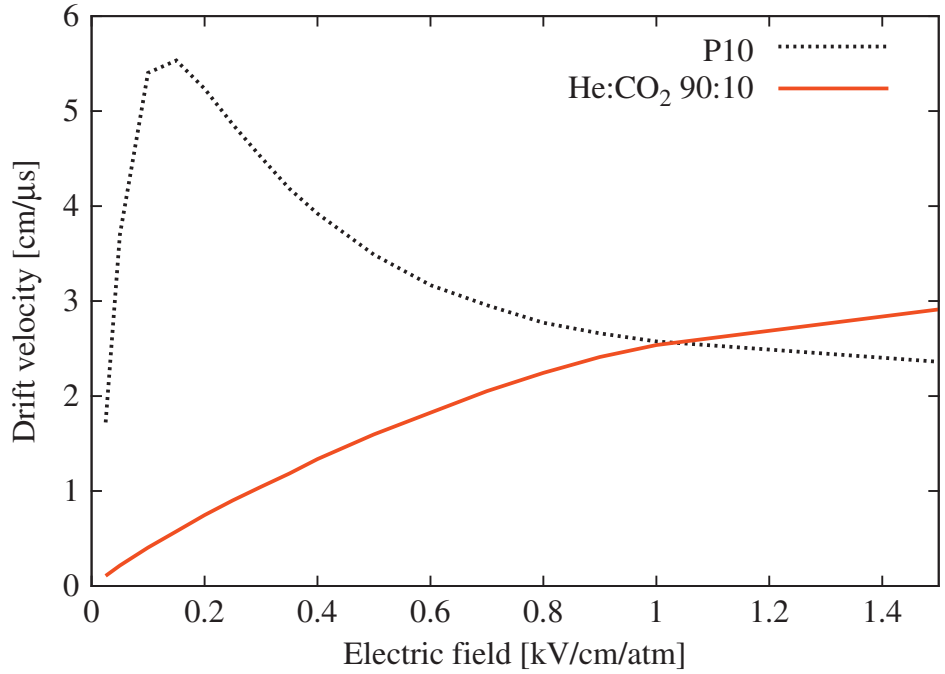

Figure 4.13: Simulated electron drift velocities for P10 (dotted line) and He:CO2 90:10 mixtures (solid line) as a function of electric field. The simulation was made using the Magboltz code [62]. Figure from Ref. [27].

to glue a thin foil of para-aramid, or Mictron, produced by Toray Industries, Inc. Mictron has a density of 1.45 g/cm^3. The specific foil used as the beam window has a thickness of 0.536 mg/cm^2, or 3.7 μm.

To use the prototype AT-TPC for a wide variety of nuclear reactions studies, many different types of gases must be available to use as active target gases. In order to achieve this versatility in gas choice, the high electric field capability of the prototype AT-TPC is vital due to the sometimes radically different electron drift velocities of various gases. Lower drift velocities cause a longer detector dead time, limiting the beam particle rate that can be delivered to the device.

Magboltz [62], a code used to simulate the transport of electrons in gas mixtures, is used to compare the drift velocities of electrons in both He:CO_2 90:10 and Ar:CH_4, or P10, gas

mixtures. The comparison is shown in Fig. 4.13. In the figure, one sees a sharp peak at low electric fields in the P10 simulation, while for He:CO_2 90:10 a smooth rise in drift velocity as a function of electric field is seen. Near 0.2 kV/cm/atm, the drift velocity in P10 is about an order of magnitude higher than that in He:CO_2 90:10. This electric field value is the typical operating voltage of many large scale TPCs [63]. At this value, for a given drift length of 100 cm, a drift velocity of 0.5 cm/μs results in a 200 μs maximum dead time. Such a dead time, coupled with a beam particle rate of 1 kHz, results in a pile up ratio of 20% [27].

In order to avoid such a large dead time scenario, an electric field that is higher than the typical value of 0.2 kV/cm must be used. By utilizing a field of 1 kV/cm at atmospheric pressure, the electron drift velocity in He:CO_2 90:10 is near 2.5 cm/μs. To achieve this field across the 50 cm length of the field cage, a voltage of -50 kV is applied to the cathode [27].

As described in the preceding sections, insulating gas and the corona ring ensure that there is minimal risk for sparking. Tests were performed to rate the maximum voltage on the cathode. The active target gas was He:CO_2 90:10 with an insulating nitrogen gas, both held at atmospheric pressure. The tests were made with a 880PL-10 mA-A unit, a portable DC insulation tester used to supply power to the cathode. The tester was manufactured by Hipotronics. The voltage was increased up to -60 kV before any internal sparking occurred. This -60 kV value corresponds to the maximum voltage rating of the beam duct, and is 20% larger than the nominal -50 kV operating voltage of the cathode. Thus, the safety margin over the maximum operating voltage of the cathode is 20% [27].

The nitrogen insulation gas has a dielectric strength of 34 kV/cm/atm [60]. At 1 atm and with an approximately 6 cm separation between the field cage wall and exterior chamber wall, the insulation gas has a strength of about 200 kV, well above the 50 kV rating of the cathode [27].

4.2.4 Micromegas

A basic description of the operating principles of the Micromegas electron amplification device is found in Section 2.2.3. This section will describe more details about the specific Micromegas used in this work.

The Micromegas is mounted on the downstream end of the field cage. The two basic components of the device are the anode readout plane and the micromesh. Made of 18 μm diameter SDC 45/18 stainless steel wire manufactured by Bopp, the wire is woven with a 63 μm pitch into a mesh plane. Insulated pillars 0.3 mm in diameter are arranged in a 2 mm by 2 mm grid pattern on the anode readout plane to support the mesh at a uniform 128 μm distance above the plane [27]. A field of about 50 kV/cm is held over this distance, which serves as the amplification gap for the electrons.

The anode readout plane is made of printed circuit board (PCB) and was designed and fabricated at the NSCL. The electrodes for the anode consist of copper that has been electroplated with 3 μm of nickel and 1 μm of gold via immersion. This electroplating was done to prevent oxidation damage of the surface of the electrodes and to provide a smooth surface [27]. The assembly of the anode PCB and the micromesh was performed at SEDI/IRFU CEA-Saclay using bulk technology [64].

The anode plane's layout was designed to optimize resolution for kinematical reconstruction of binary events. The anode plane is circular and centered on the beam axis. The active area of the plane is 250 mm in diameter. This area is divided into individual readout channels, referred to as pads. The segmentation of the pads is radially symmetric from the center to optimize radial resolution. The central pad is circular with a 5 mm diameter. All other pads are coaxial in shape and 2 mm wide, and are spaced with a 0.25 mm gap. The coaxial

pads are separated into four quadrants, with the five inner-most pads further separated into eight octants for improved resolution near the beam axis. Each quadrant is comprised of 63 pads, resulting in 253 pads in total [27].

The pads are routed to three surface mount connectors that are soldered on the back of the PCB. Two of the connectors have 100 inputs, and the third has 60, enough in total for all 253 pads. The three connectors couple to the feedthrough on the endplate where the Micromegas is mounted. If so desired, an adapter can be inserted between the endplate and the Micromegas to adjust the placement of the Micromegas relative to the field cage. For this work, the Micromegas was located about 5 mm downstream from the last field cage ring electrode. Six threaded stand-offs are mounted on the back of the PCB for mounting to the endplate. The endplate has six holes drilled into it that are aligned with the stand-offs. The Micromegas are the held to the endplate with six self-sealing screws that are inserted from the backside of the endplate. The endplate's KF40 flange contains an SHV feedthrough that provides a voltage to the micromesh [27].

As first shown in Section 2.2.3, Fig. 2.5 is a photograph of the Micromegas used in this work, while Fig. 2.6 illustrates the tracking detection technique of the Micromegas.

The beam particles enter the field cage perpendicular to the Micromegas. As a ^{10}Be beam particle traverses the active target, the central pad and some of the inner coaxial pads record the energy deposit profile of the particle in time, from which the position of the particle along the beam axis (z) can be calculated given the 24.0 mm/μs drift velocity of the electrons in the active target gas. After an elastic scattering reaction, the outgoing ^{10}Be and ^{4}He particles travel over multiple coaxial pads in opposite quadrants as they leave the beam axis. For each particle, the strips over which it travels give the energy deposit profile as a function of radius r from the center in addition to z, from which the polar angle and total

range of the particle can be calculated. The azimuthal angle cannot be calculated with this design of Micromegas, but for binary reactions, the two products have opposite azimuthal angles, ensuring that they are recorded in opposite quadrants and thus have separable energy deposit profiles [27].

4.2.5 Readout Electronics

The schematic of the electric circuit used for the signal readout of the Micromegas is given in Fig. 4.14. The circuit handles both the anode pad signals and the micromesh signal. The micromesh signal is used as a trigger for reading out the pad signals. The pad signals are digitized and the waveforms of each of the 253 pads (252 separated into quadrants and one central pad) are individually recorded. The electronics includes a 511 channel sampling capacitor array for analog memory, an analog-to-digital converter (ADC), and zero-suppresion [27].

A DC power supply holds a negative bias voltage on the micromesh, and a 100 MΩ resistor is included to limit discharge currents that may occur in the Micromegas. A 2001A Canberra charge-sensitive preamplifier is used, with a 20 nF decoupling capacitor, to amplify the signal of the collected charge on the micromesh [27].

One contribution to the signals in the Micromegas is cross-talk due to the capacitive coupling of the pads. The pads are coupled because the micromesh spans the entire anode plane. Thus, when one pad creates a signal due to an electron avalanche between it and the mesh, reverse polarity pulses are induced on the other pads. The induced pulses can distort the signals on the nearby pads if they also have avalanche signals simultaneously with other pads. The cross-talk pulse amplitude is proportional to the ratio of the capacitance $C_{\text{pad-mesh}}$ and the total capacitance $C_{\text{mesh-ground}}$ between the mesh and ground. This amplitude is

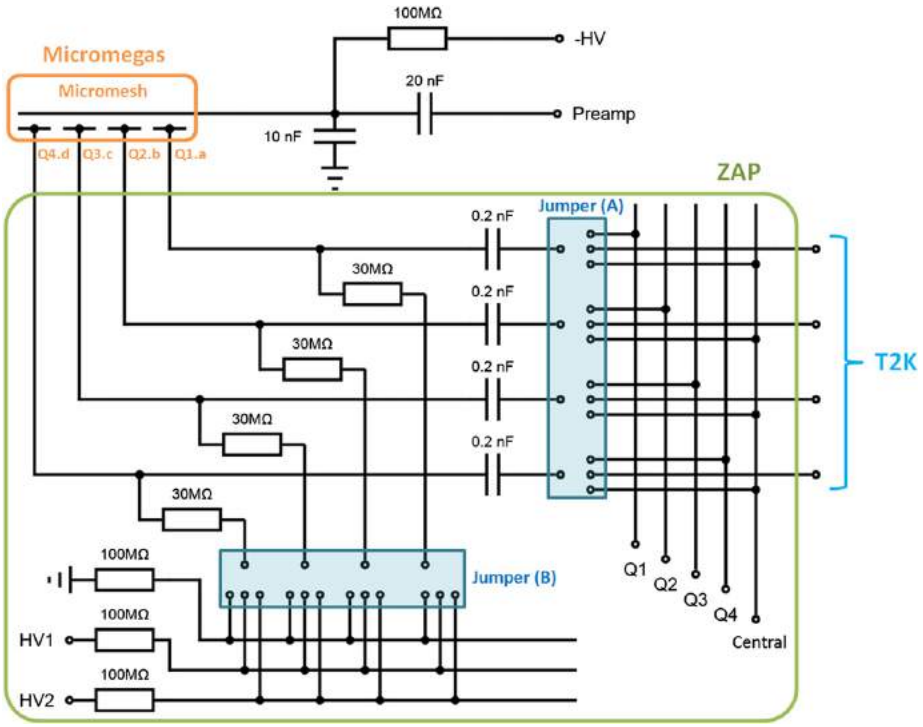

Figure 4.14: Schematic diagram of the readout circuit for the Micromegas. For simplicity, only one pad is shown for each quadrant (Q1.a, Q2.b, Q3.c and Q4.d). The pad signal Q#.X (# = Quadrant ID, X = Pad ID) can be routed to the T2K electronics, the quadrant output 'Q#' and the central output 'Central,' which can be selected by the jumpers A. Signals can be split and sent to multiple outputs by installing resistive jumpers. The potential of individual pads can be selected to be ground, or a different choice of high voltages HV1 or HV2 by the jumpers B. Figure from Ref. [27].

minimized by increasing the detector capacitance relative to ground. The largest contributor to $C_{\text{mesh-ground}}$ is typically the capacitance $C_{\text{mesh-anode}}$ between the mesh and anode plane. The value of $C_{\text{mesh-anode}}$, when modeled in vacuum with a parallel plate configuration, is about 4 nF. Therefore, an additional 10 nF capacitor is added between the mesh and ground to increase $C_{\text{mesh-ground}}$ and thus decrease cross-talk [26]. The value of the capacitor was limited to 10 nF to reduce the risk of damage by discharge of the energy stored in the capacitor and to preserve a good quality signal of the mesh preamplifier [27].

The readout electronics [65] used were originally developed for TPCs used in the Tokai-to-Kamioka (T2K) experiment for neutrino oscillation measurements [66]. The Front End Card (FEC) handles pulse shaping and digitization, and data transfer is done with the Front-End Mezzanine card (FEM). Four Application-Specific Integrated Circuits (ASICs), each with 72 inputs, are located on the FEC. A preamplifier, shaping amplifier, and analog memory for recording input signals and waveforms is included for each pad signal channel. A Sampling Capacitor Array (SCA) built of 511 capacitor cells is used for the analog memory storage. The charge stored in each cell is proportional to the input amplitude. The time window over which the signal is stored in the SCA is programmable to between 0.02 and 1 μs, resulting in a total time range of 10 to 511 μs . Acting as a circular buffer, the SCA samples the input signal over its 511 cells. When the FEM receives an external trigger, the writing in the SCA is stopped. After a read order, the stored charges are sent in sequence to the FEC, where they are converted to a digital number by a 12-bit ADC [27]. A diagram depicting the actions of the SCA is given in Fig. 4.15.

An adapter board, called the ZAP board [27], is used to connect the FEC to the feedthrough from the Micromegas pads located on the back of the endplate of the prototype AT-TPC. The ZAP board and FEC are shielded form electromagnetic interference by two copper plates. The plates also ensure that the FEC is grounded to the exterior of the prototype AT-TPC. A photo of the ZAP board is shown in Fig. 4.16.

The FEM is mounted on the back of the FEC and is unshielded. The fully mounted electronics setup used in this work is shown in Fig. 4.17.

Developed at NSCL, the ZAP board serves two purposes: (1) it allows for each pad to have a specific gain and (2) it relays signals from the pads to the FEC for generating a

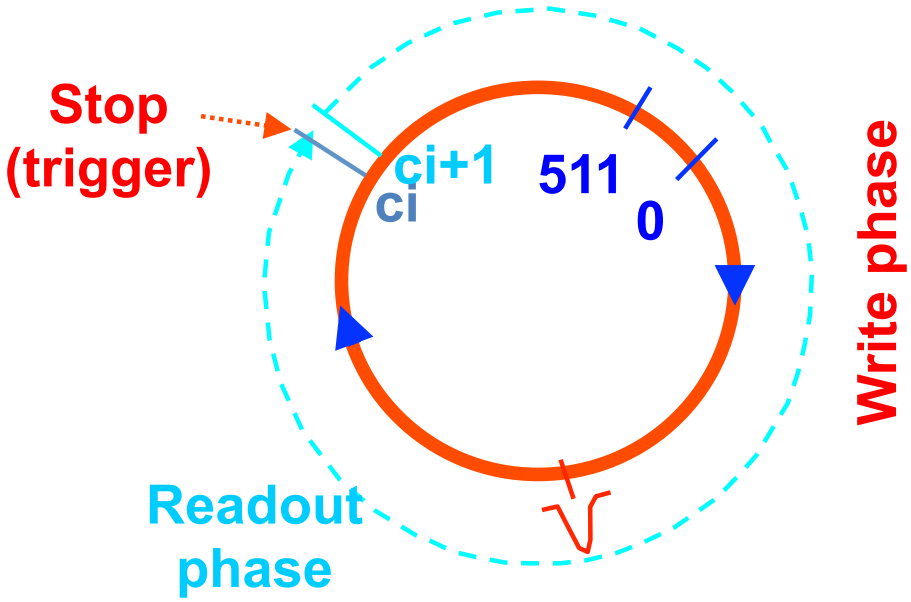

Figure 4.15: Diagram of the writing and readout of the Sampling Capacitor Array (SCA). The SCA is continuously filled in a circular manner. When a trigger signal is received, all 511 cells are read out. Figure from P. Baron.

trigger [27]. In this work in particular, the gain variation feature of the ZAP was necessary to trigger binary events.

Gain variation among pads is achieved in the ZAP board by applying specific biases to individual pads. The gain is a function of the potential difference between the pad and the micromesh [26]. On the ZAP board, a shunt jumper for each pad is used to select one of three possible bias voltages. These jumpers are labeled Jumper (B) in Fig. 4.14. A data plot showing the relationship between gain and the applied voltage on the Micromesh is given in Fig. 4.18.

The utility of gain variation comes from the difference in the energy deposit profile of nuclei with different atomic number Z. As described by the Bethe formula in Eq. 2.1, the energy loss of charged particles in a gas is proportional to Z^2. Considering the nuclei studied in this work, a ^{10}Be particle will deposit four times the energy per unit length as ^{4}He at

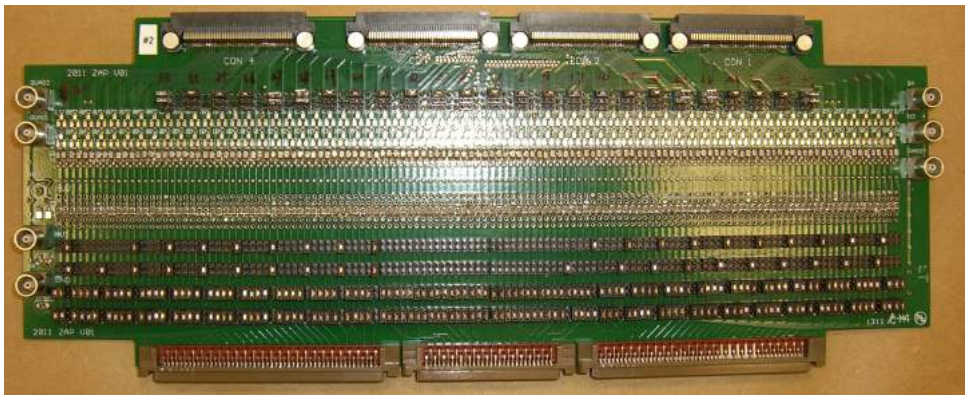

Figure 4.16: A photo of the ZAP board before mounting.

the same velocity. There are two scenarios for keeping a uniform gain across all pads in this case, and both are limited by the finite dynamic range of the readout electronics. One is that the energy deposit profiles of ^{10}Be particles are successfully recorded. However, this would result in the ^{4}He signal being in the noise, and thus not recordable. On the other hand, if the uniform gain is increased to allow for the ^{4}He energy deposit profiles to be measured, the pads over which the ^{10}Be particles traverse would become highly saturated, resulting not only in an unreliable measure of deposited energy on a given pad, but also in large cross-talk between neighboring pads and channels, rendering the ^{10}Be pad signals essentially useless.

The solution to this gain dilemma is to vary the gain on specific pads. The majority of the pads are kept at a gain suitable for recording the energy deposit profile of ^{10}Be. Every fifth pad from the center, however, has an increased gain in order to record the energy deposit profile of ^{4}He particles, allowing for binary events to be triggered. A more detailed description of the triggering scheme is found in Section 4.3 later in this chapter.

The second purpose of the ZAP board is to route signals from the pads to the electronics. There are three options for signal routing [27]:

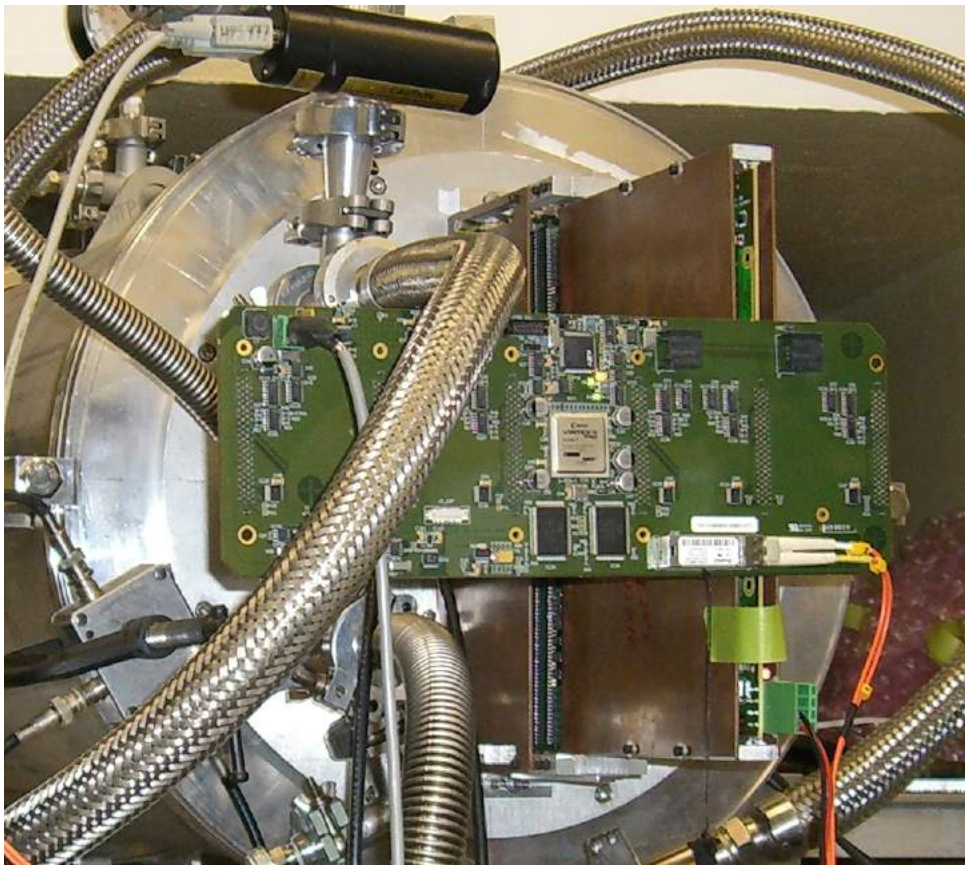

Figure 4.17: A photo of the shielded ZAP board and FEC as mounted on the prototype AT-TPC. The unshielded FEM is perpendicularly mounted on the back of the FEC.

1. Output each individual signal to the T2K electronics.

2. Output Q1, Q2, Q3, and Q4, each corresponding to one quadrant. The pad signals are therefore separated only by which quadrant they are found in. These quadrant output signals can then be used as a condition for triggering on product nuclei as they travel through the TPC away from the beam axis.

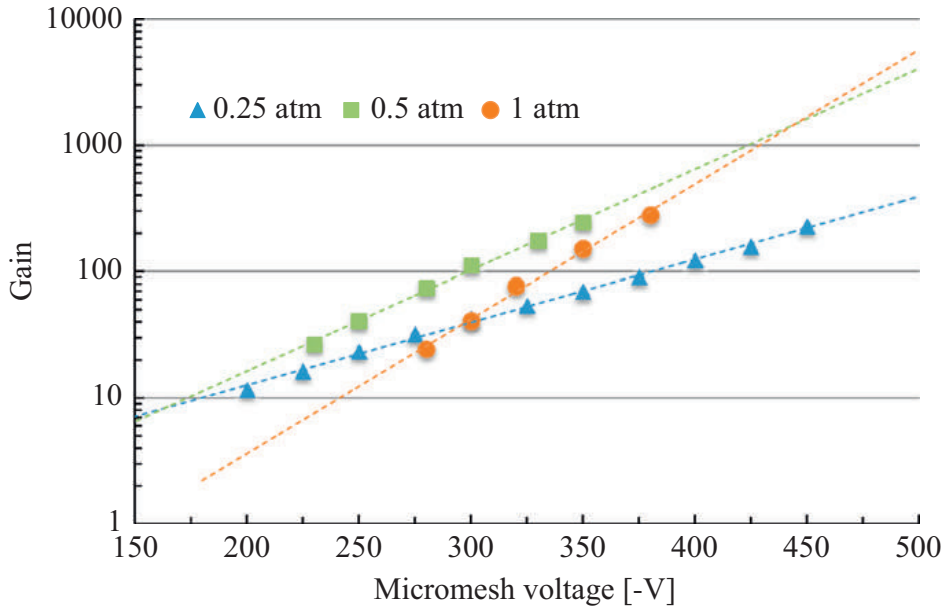

Figure 4.18: Electron amplification gain of the Micromegas as a function of micromesh voltage. The data were measured in He:CO_2 90:10 mixtures at 0.25 atm (blue triangles), 0.5 atm (green boxes), and 1 atm (orange circles). Figure from Ref. [27].

3. Output 'Central.' This option sums the signals of all pads set to 'Central' and is only available to pads within 2 cm of the center of the Micromegas. 'Central' is thus used to record the energy deposit profile of the beam.

The three output options are selected by the use of a shunt jumper, labeled as Jumper (A) in Fig. 4.14. If the jumper used is resistive, the signal can be divided and thus routed to multiple output options simultaneously [27]. The exact options chosen for this work are described in Section 4.3.

The FEC then digitizes the data during the read phase and transfers the data to a computer for collection through the FEM. The FEM outputs the data to the Data Concentrator Card (DCC) via an optical fiber. The fiber decouples the shared ground of the FEC, FEM, and prototype AT-TPC from the DCC and the computer to isolate the analog electronics from potential sources of noise. The DDC is based on the ML507 Evaluation Platform of

Xilinx, Inc., and interfaces the FEM with the computer via an ethernet cable [27]. The collection of data in this work is further described in Section 4.4.

The parameter settings used for the T2K electronics in this work include a 0.5 μs peaking time, a 40 μs time window, and a gain of 360 fC over all 4,000 digitalized channels.

4.3 Experimental Setup

During the experiment, the prototype AT-TPC was installed in the vault beyond TwinSol, as shown in Fig. 4.1. A schematic of the prototype AT-TPC including the Micromegas used in this work is found in Fig. 4.19.

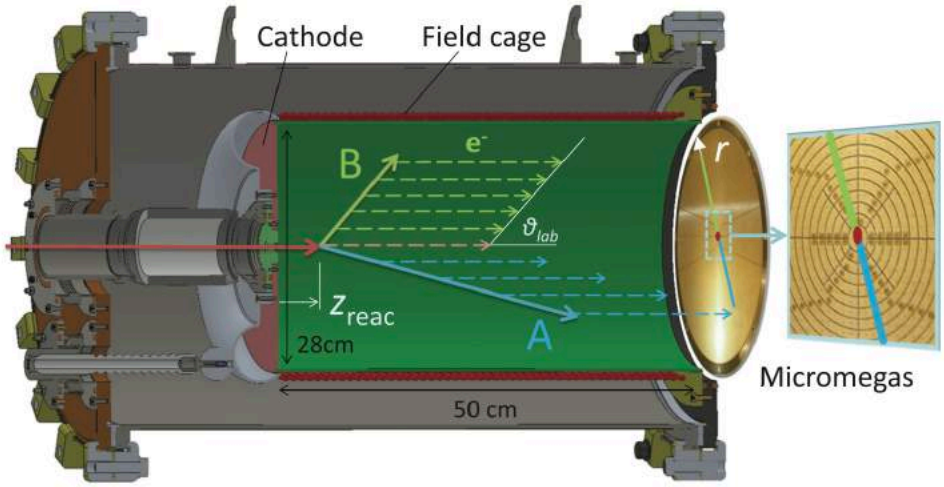

Figure 4.19: Schematic drawing of the experimental setup of the prototype AT-TPC. The inset is a magnified view of the segmented anode pad plane of the Micromegas detector near the beam axis. Figure adapted from Ref. [9].

4.3.1 MCP and Beam Ladder

As mentioned in Section 4.1.3, a beam steerer is located after TwinSol. A high vacuum ISO160 tee, shown in Fig. 4.20 was placed after the beam steerer. This tee houses a Micro-Channel Plate (MCP) detector and a beam ladder, on which various items may be mounted.

An MCP is a fast amplification device. It consists of a bundle of glass tubes with diameters and spacing on the order of a few microns. The upper and lower sides are plated with Ni. The plate is typically held at a voltage of 500 to 1000 V. Each channel acts like a miniature photomultiplier tube (PM tube [41]). When a particle, such as an electron, enters one of the channels of the MCP, a cascade of electrons is formed, amplifying the signal. The MCP used in this work is made of Ni-Cr and was built by tectra GmbH. Its model number is MCP-33-D-R-A. The design employs two identical MCPs. The channels in each plate are angled at $12° \pm 1°$, and the plates are stacked in a Chevron style such that the channels of one plate are rotated 180° with respect to the channels of the other plate, forming a 'V'

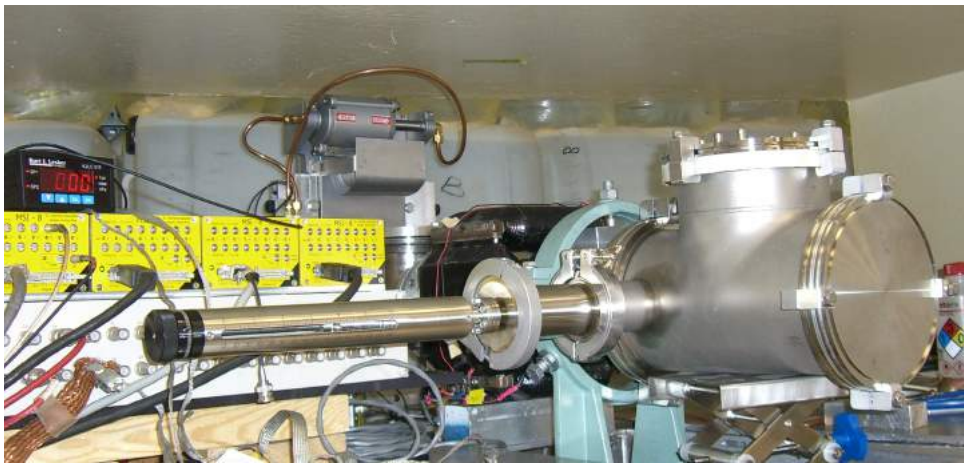

Figure 4.20: Image of the ISO160 tee with the retracting beam ladder. The MCP is mounted on the top flange and is install inside of the tee. The black beam steerer can be seen located a few inches upstream of the tee.

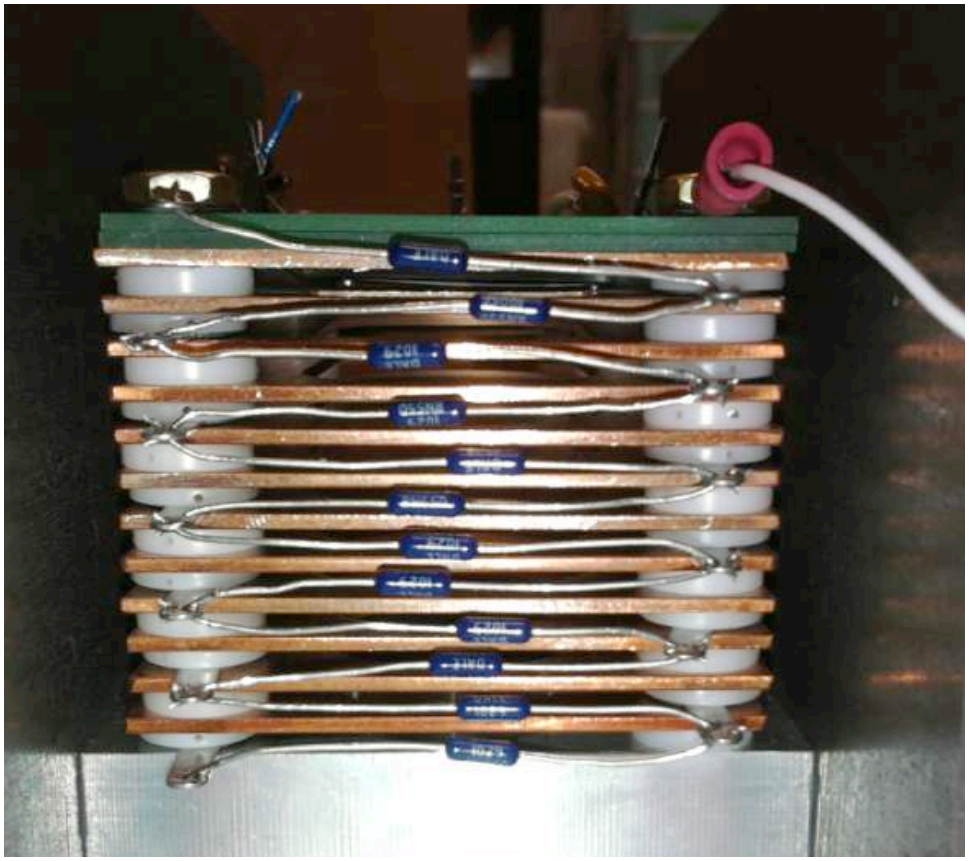

Figure 4.21: A side view of the copper plates and resistor chain on the MCP housing. The MCP and foil are both located on the green PCB on the top of the chain.

shape. This stacking method is chosen to prevent positive ions from traveling back through the plates. The channels have a diameter of 12 ± 0.5 μm and a pitch of 14.5 ± 0.5 μm. The plates are 33 mm in diameter with a 25 mm active diameter. When biased to 2 kV, the pair has a gain of about 5×10^6.

As part of the setup of the Protoype AT-TPC, the MCP is used as a beam diagnostic tool. Its role is to measure the incoming beam rate into the AT-TPC and to output a trigger signal for the incoming beam particles.

The beam is measured by the MCP without being intercepted. A double-sided-aluminized polypropylene foil of thickness 70 μg/cm^2 is placed in the path of the beam and held at a

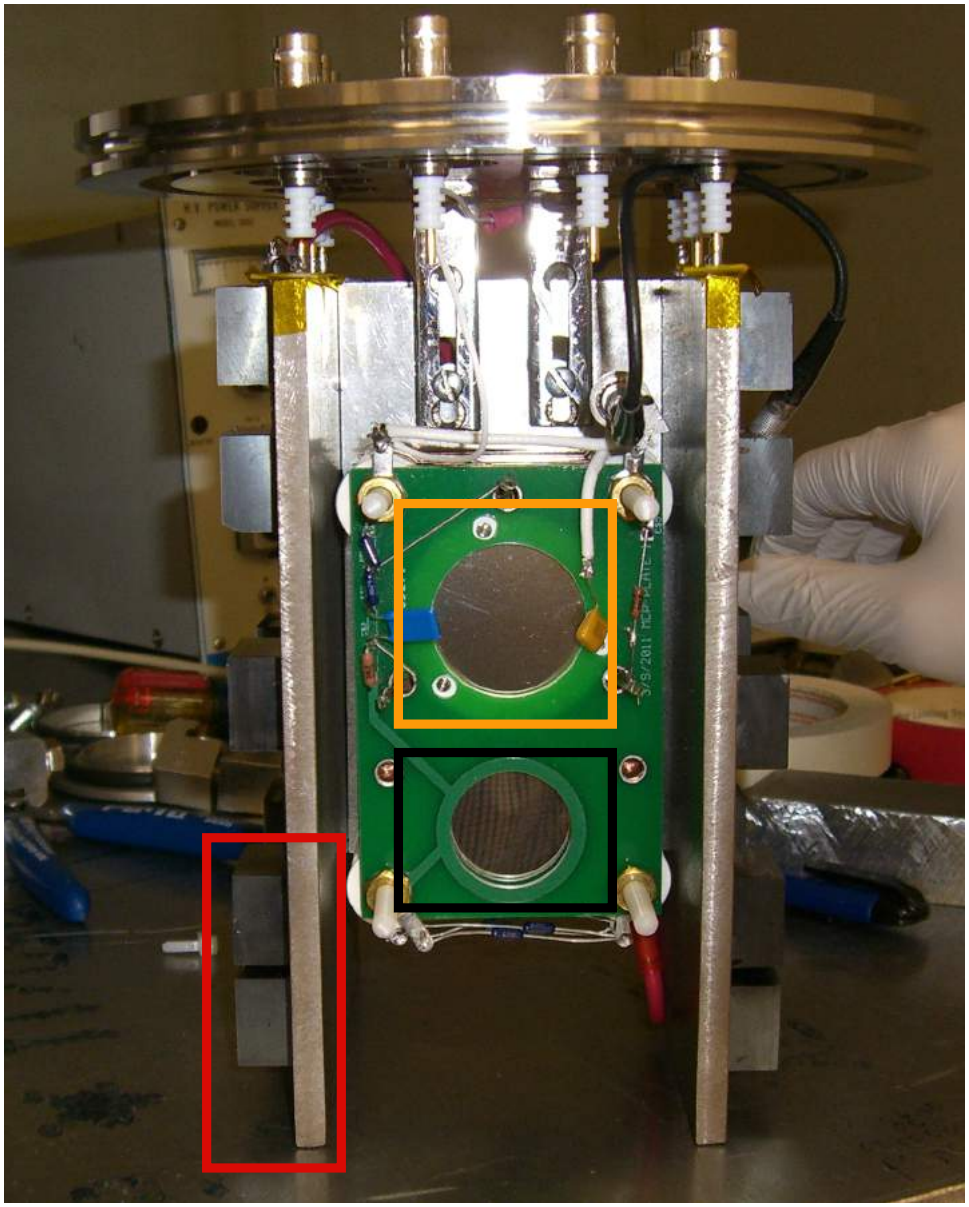

Figure 4.22: Image of the MCP mounted on its housing and flange. Inside of the red rectangle are two of the small permanent magnets mounted on one of the soft iron walls. The orange rectangle shows the location of the back of the MCP anode, while the black rectangle below identifies the double-sided-aluminized polypropylene foil.

negative potential of −2400 V. As the beam particles pass through the foil, they lose negligible energy in producing secondary electrons off of the thin foil before continuing onward into the prototype AT-TPC. A 0.5 kV/cm electric field is established parallel to the beam axis, and the electrons freed from the foil are accelerated in this field. Superimposed is a perpen-

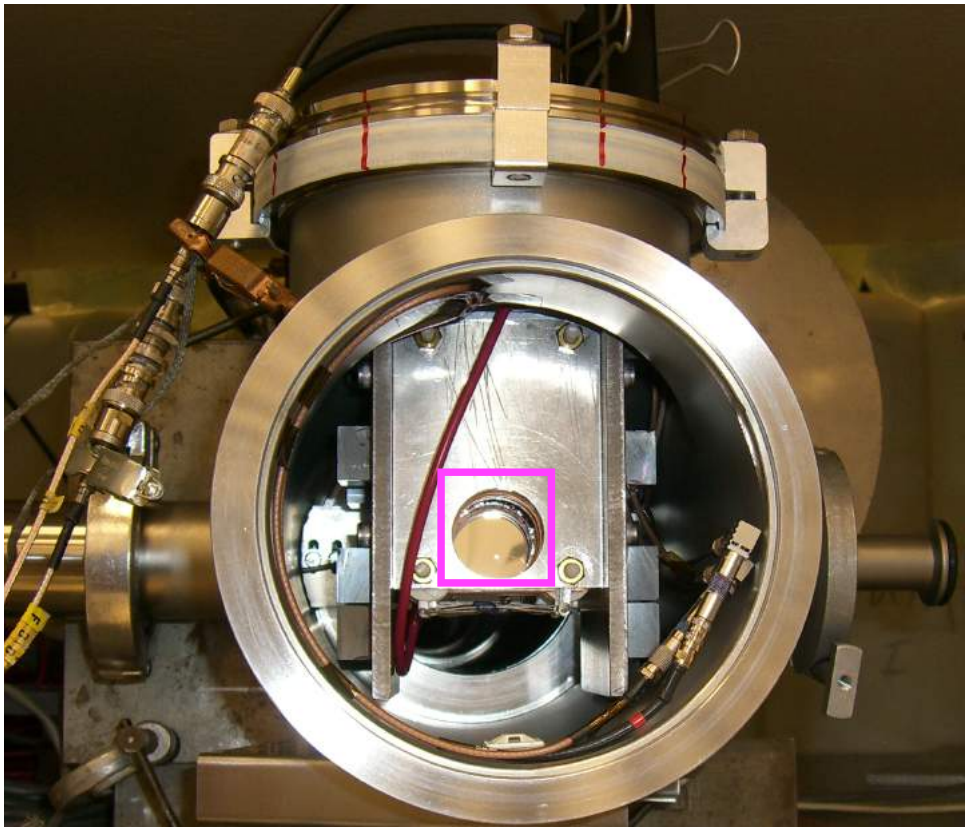

Figure 4.23: The MCP installed in the ISO160 tee, slightly downstream from the beam ladder. Behind the tee, iron and steel plates are mounted to minimize the effects of stray fields from the beam steerer on electron traveling from the foil to the MCP. The foil can be seen inside of the magenta square.

dicular 65 G magnetic field. This $\mathbf{E} \times \mathbf{B}$ field transports the electrons a lateral distance of 4.5 cm to the MCP. The upper side of the MCP is at -2300 V, and the electrons therefore have an energy of 100 eV when hitting the MCP. This energy corresponds to the maximum detection efficiency of the MCP for electrons. The electric field is created by stepping down 2.4 kV over twelve copper plates connected in series with a chain of 10 MΩ resistors, seen in Fig. 4.21. The plates are shaped such that there is an open path along the beam axis and for also an open path for the electrons to be transported from the foil to the MCP. The magnetic field is made by placing twenty small permanent magnets on the soft iron outer walls of the housing, creating a uniform magnetic field between the two walls. While the

electric and magnetic fields are of proper strength to accelerate and bend the electrons to the MCP, they have a negligible effect on the nearly 40 MeV beam particles. The assembled housing as used in this work is shown in Fig. 4.22, and Fig. 4.23 shows it installed in the ISO160 tee.

Once the electrons reach the MCP, they are amplified and the signal is sent to a three-step cascade fast amplifier. From the amplifier, the signal is sent through a leading edge discriminator and then a gate and delay generator, where a 10 μs window is set. This window, in principle, acts as a trigger window for reactions in the prototype AT-TPC. For this experiment, however, the MCP signal could not be used as trigger. The beam rate through the MCP was about 10 kpps (kilo-particles per second), while the beam rate inside of the TPC, as measured by the mesh signal (described later) was only 1 kpps, an order of magnitude less. This difference in rate is due to the large emittance of the secondary beam; most beam particles that pass the MCP were not focused in the small 7 mm diameter beam window of the prototype AT-TPC.

While the MCP did not give the rate of the beam delivered to the prototype AT-TPC, the signal was used to determine how much beam was produced from TwinSol. In other experiments where the beam had smaller emittance, the MCP signal was used as trigger.

In addition to the MCP, the ISO160 tee housed the beam ladder, a retractable arm on which various items can be mounted. The ladder was manufactured by Kurt J. Lesker Company, Part# KLSDDA, Screw Drive KLSD Series (Bellows Sealed), 6" travel, CF1.33". To accommodate the ladder, a KF40 sleeve was welded onto the ISO160 tee, perpendicular to the beam axis and parallel to the floor. During this experiment, a pair of Si detectors, a ^{228}Th 3 μCi α source, and an iris collimator were mounted on the ladder, as seen in Fig. 4.24.

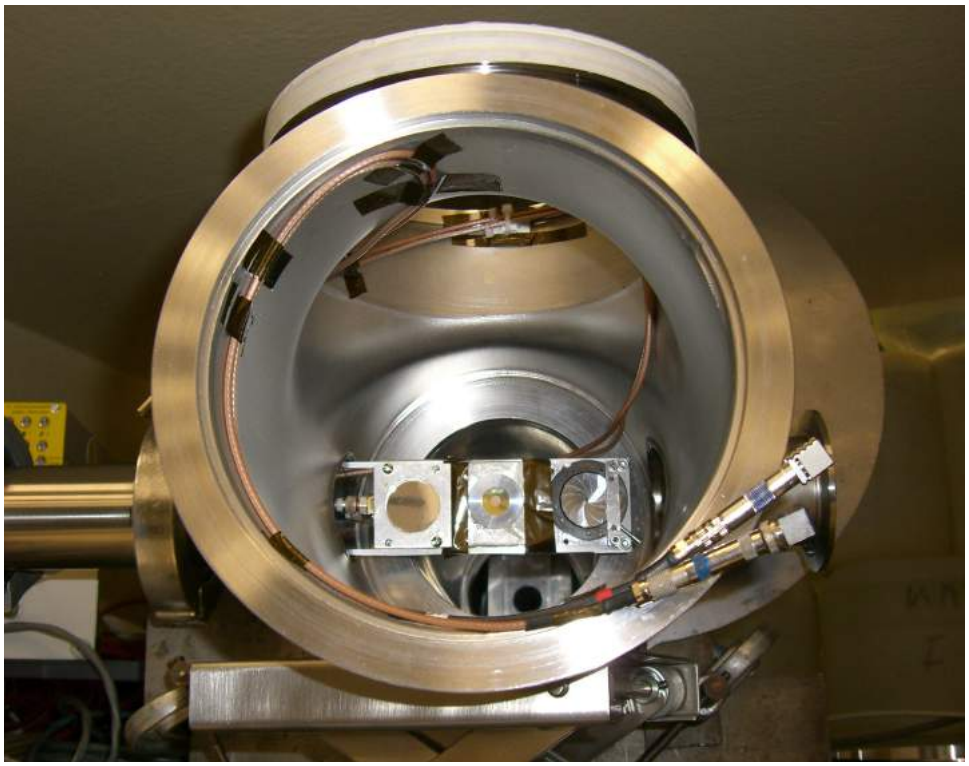

Figure 4.24: The beam ladder installed in the sleeve of the ISO160 tee. On it are mounted, from left, a stacked pair of Si detectors, a ^{228}Th 3 μCi α source, and an iris collimator.

The Si detectors are stacked on top of each other, one on each side of the beam ladder. The detector further upstream acts as a ΔE detector, with the one downstream acting as an E detector. Both detectors have an active area of 450 mm^2 and are Ortec models. The ΔE detector is model 43-017J and is 50 μm thick, while the E detector is model 31-493A with a 1000 μm thickness. Together, the pair is used for beam diagnostics along with another detector, described in detail in Section 4.3.2. A detailed description of Si detectors can be found in Ref. [41].

A 3 μCi ^{228}Th α source was installed on the beam ladder for testing the detection efficiency of the MCP. In the testing, the α particles travel through the foil mounted on the MCP housing and are detected by a Si detector mounted on the back of the housing. The number of events registered by the MCP is compared with that of the Si detector, from which an

efficiency is calculated. The Si detector used was model TB-24-450-300-5. The tests yielded a detection efficiency of between 80% and 85% for the MCP. Stray fields from the beam steerer can alter the paths of electrons to the MCP, lowering the device's efficiency. Iron and steel plates placed between the ISO160 tee and beam steerer minimize the stray fields, alleviating this issue. Some of the plates can be seen clamped behind the tee in Fig. 4.23.

The last item on the beam ladder was an iris collimator, or iris diaphragm. Model #53-911 from Edmund Optics, the diaphragm is made of stainless steel and has an outer diameter of 37.00 mm. Its maximum aperture is 25.00 mm in diameter, and its minimum aperture is 0.90 mm in diameter. The purpose of the iris is to use its adjustable aperture to collimate the beam before the MCP and prototype AT-TPC if needed. For this experiment, the iris did not prove necessary.

The three items on the ladder were positioned on the ladder as follows, with respect to the distance settings of the ladder: 136.84 mm to the center of the Si detectors, 99.3 mm to the center of the α source, and 56.97 mm to the center of the iris. Thus, when the ladder was retracted to 136.84 mm, the Si detectors were centered on the beam axis, and similarly for the α source and iris. When the ladder was set to 17.00 mm, there were 35 mm of clearance around the beam axis, which is larger than the 33 mm foil on the MCP housing. Therefore, when the beam is delivered to the prototype AT-TPC, the ladder was set anywhere between 0 and 17 mm to clear the beam passage.

The MCP and beam ladder were both aligned on the beam axis with the use of a telescope permanently installed in the vault where the experiment was held. The crosshairs of the telescope are centered on the beam axis, and adjustment knobs on the telescope are available to measure how far off axis an object is both vertically and horizontally. For example, by viewing the foil on the MCP housing through the telescope, its relation to the beam axis

can be seen and measured. The MCP mounted is then adjusted until it is on axis. This measurement and adjustment method is done iteratively until the foil is aligned to a precision of about 1 mm from the axis center. The same method is done with the beam ladder. The alignment of the prototype AT-TPC is similar and will be discussed in more detail later.

4.3.2 Position Sensitive Si Detector

Once the MCP and beam ladder were installed in the ISO160 tee, a Position Sensitive Si Detector (PSSD) was temporarily placed after the tee for measuring the energy of beam particles. The PSSD was placed at the location where the entrance window of the prototype AT-TPC would later be located, about 36.8 cm downstream from the centering ring on the downstream flange of the ISO160 tee. Thus, the PSSD provides a measure of the energy of beam particles as they enter the prototype AT-TPC. Fig. 4.25 shows the installation of the PSSD as used in this work.

Figure 4.25: The PSSD mounted past the ISO160 tee, at the eventual location of the beam window of the prototype AT-TPC.

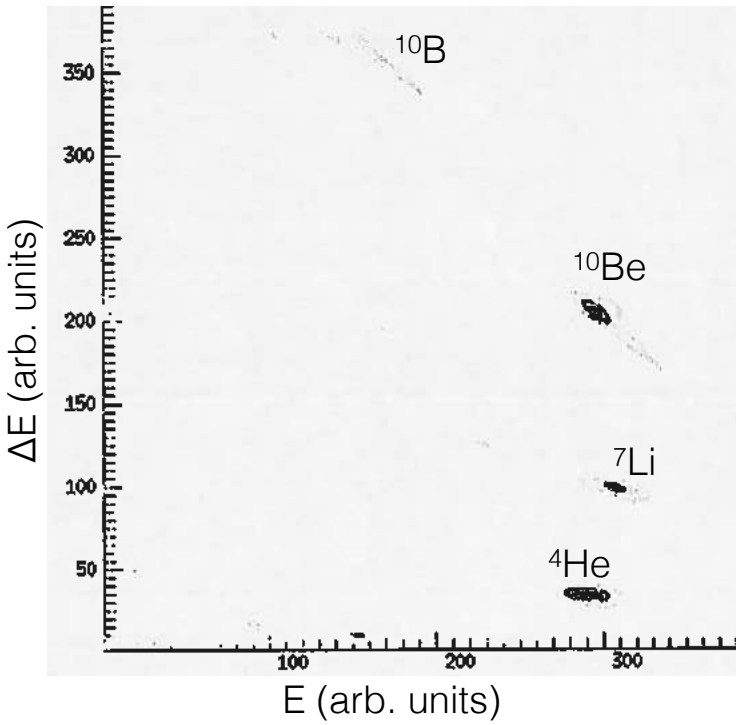

Figure 4.26: Spectrum of $E - \Delta E$, showing separation of isotopes in the beam. The relative intensities of the isotopes somewhat change as beam conditions change.

The PSSD is 230 μm thick and was custom-built by the UC-Berkeley detector group. It is stacked with a thinner Si detector used as a ΔE detector. The ΔE detector is an Ortec 24-008A model, and is 50 μm thick.

The position sensitivity of the PSSD was calibrated with the α source on the beam ladder. An asymmetric mask was placed in front of the PSSD. The resulting image on the PSSD provided the position determination of the device. Once calibrated, the mask was removed and the α source retracted. A 10 mm-diameter circular collimator was then placed in front of the PSSD, centered on the beam axis. Beam was then delivered to the PSSD to determine its energy. The $E - \Delta E$ detectors provided separation of different isotopes in the beam, as shown in Fig. 4.26. From the measurement of $E - \Delta E$ on the beam ladder, the energy of ^{10}Be was found to be between 38.765 and 38.799 MeV, while the $E - \Delta E$ with the PSSD was

39.543 MeV, resulting in an energy determination of $39.0^{+0.50}_{-0.25}$ MeV for ^{10}Be beam particles incident on the beam window of the device. This value was found to be consistent with the energy measured by the $E - \Delta E$ Si detectors mounted on the beam ladder, as well.

Due to energy loss in the beam window, the energy of the beam delivered inside of the prototype AT-TPC is 38.2 ± 0.5 MeV after the beam window. Confirmation of this beam energy via analysis of the length of particle tracks in the active target volume is described in detail in Section 5.3.1.

4.3.3 Prototype AT-TPC

Once the energy calibration measurement was finished, the PSSD was removed from the beam line, and the prototype AT-TPC was put in place. The TPC was mounted on an adjustable table that was bolted to the floor for stability. A bellows was used to join the ISO160 tee with the front flange of the prototype AT-TPC. The pitch of the TPC was leveled by adjusting the vertical height of the four bolts that connect the device to the table. Once leveled, the TPC was then aligned on the beam axis. An image of the TPC during the alignment process is shown in Fig. 4.27. Alignment was done in an iterative process with the beam telescope, similar to the alignment procedures for both the beam ladder and MCP, described in Section 4.3.1. The TPC alignment was more difficult, however, as both the entrance window at the front of the device and the center of the Micromegas located on the back flange must be aligned.

During the alignment procedure, it was necessary to remove the back flange of the TPC so that the beam window was visible. To keep dirt and debris from entering the chamber, plastic wrap was placed over the open back flange. The beam window was then centered on the beam axis. Once the beam window was centered, an alignment plate was installed on the

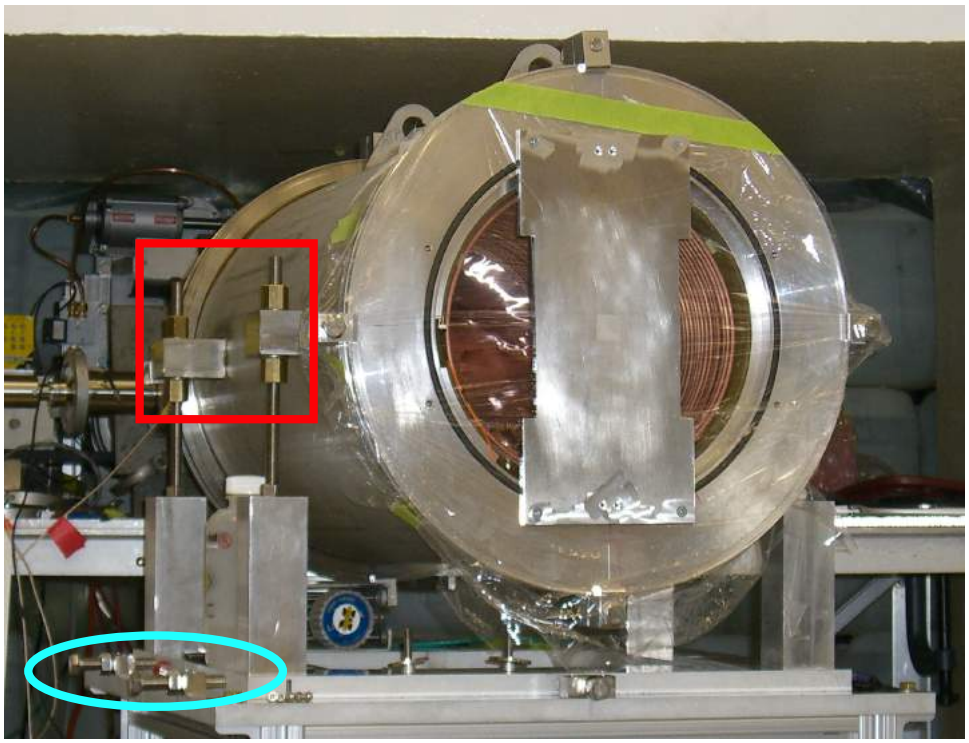

Figure 4.27: The alignment plate as mounted on the back of the prototype AT-TPC. Clear plastic wrap is taped over the flange under the plate to keep dust and dirt out of the interior of the device. The bolts that secure the TPC to the table and allow for height adjustment are highlighted inside the red square. The bolts used to horizontally adjust the TPC on the table are shown inside of the cyan oval. More such bolts are found on the opposite side of the table.

back flange of the TPC. The center of the plate corresponds to the center of the Micromegas. The plate was then centered on axis. The plate would then be removed to check that the alignment of the entrance window was not lost. If necessary, this process would be repeated until both the beam window and rear alignment plate were centered on the beam axis to within a couple of mm. The final distances between various components of the TPC and ISO160 tee as mounted are shown in Fig. 4.28.

Once aligned, the back flange on which the Micromegas were mounted was installed on the prototype AT-TPC. The ZAP, FEC, and FEM were then installed on the back flange and connected to the DDC and computer.

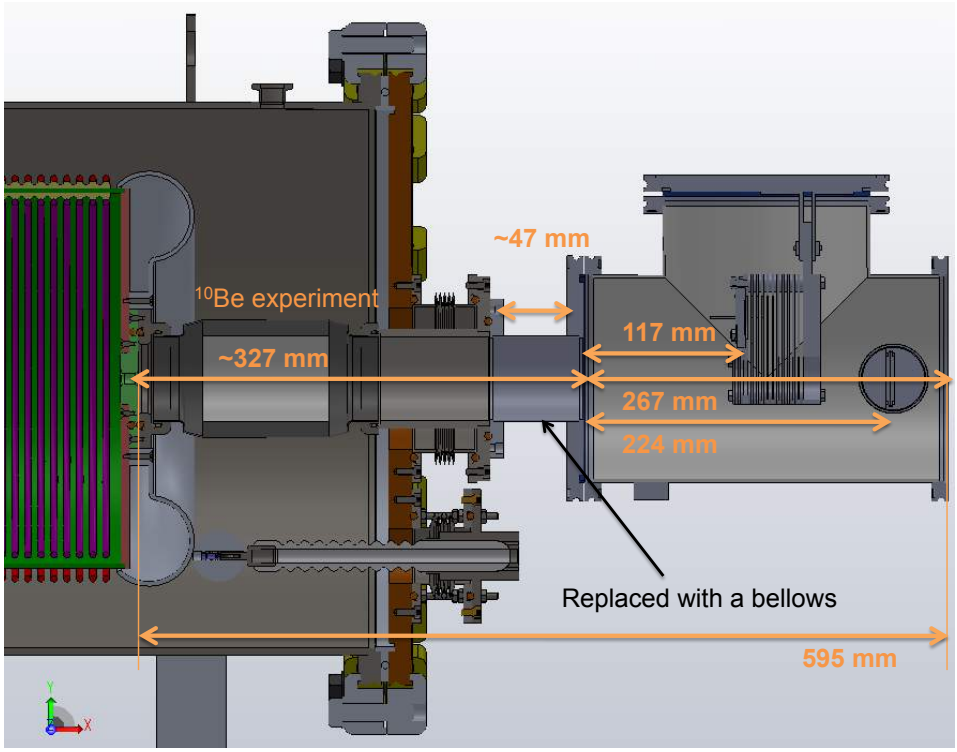

Figure 4.28: A schematic of various distances between the parts of the setup during the experimental run.

4.3.4 Gases

In addition to mounting the Micromegas electronics, the He:CO_2 90:10 active target gas and nitrogen insulation gas must be also be setup and installed. Bottles of each gas were connected to gas handlers, seen in Fig. 4.29, that controlled the pressure and flow of the gases in the detector. The bottles of He:CO_2 90:10 were pre-mixed. During the experiment, the pressure of He:CO_2 90:10 inside the field cage was 695.5 ± 0.1 torr, while the pressure of the nitrogen surrounding the field cage was 754 ± 4 torr. These pressures, however, are uncalibrated. From Weather Underground's historical data, the sea level pressure during the experiment was 30.05 inHg, or 760.3 torr. Accounting for the elevation of 211 m of Notre Dame's campus, the local atmospheric pressure becomes 743 torr. The ambient pressure

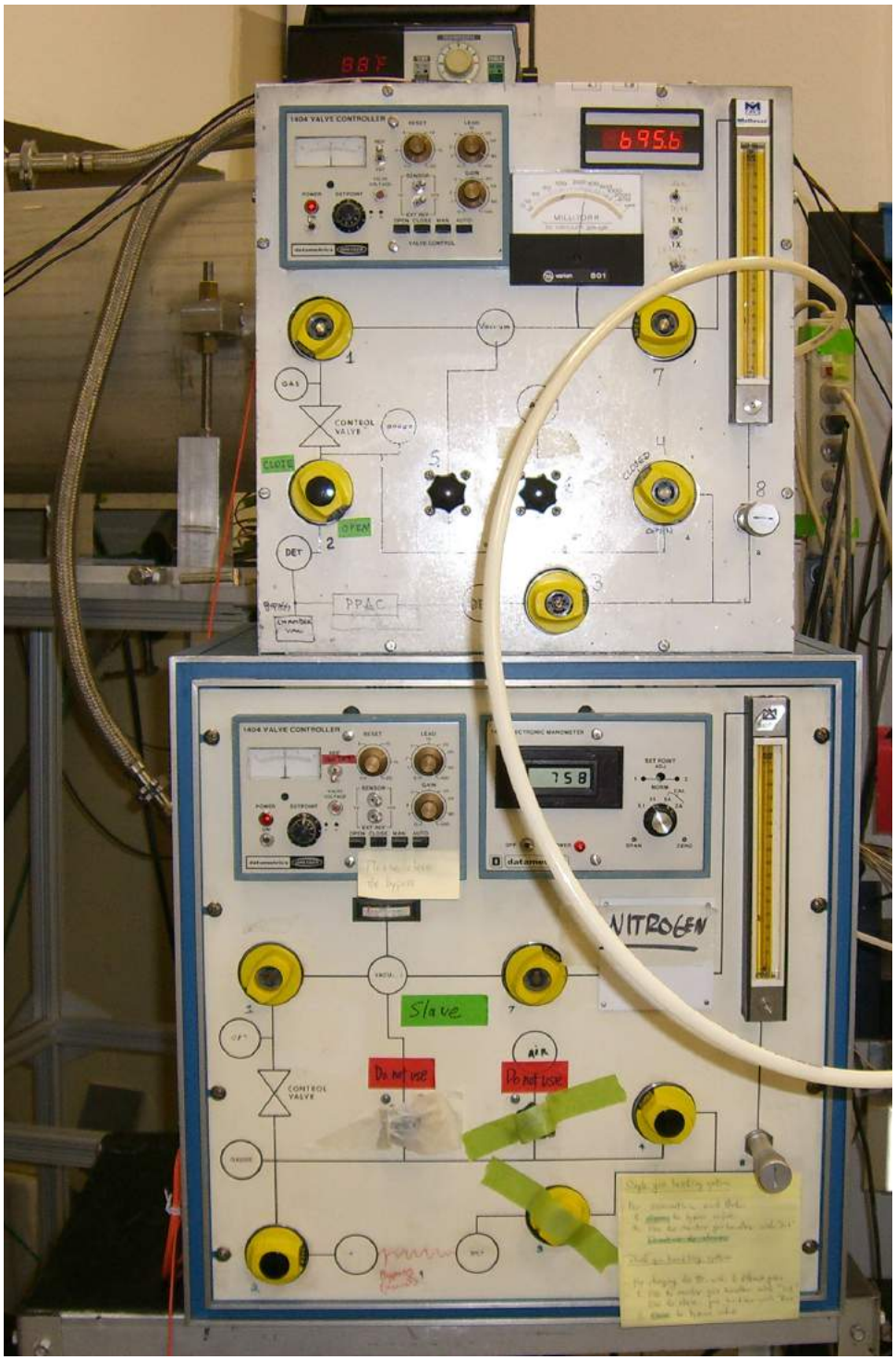

Figure 4.29: An image of the gas handlers used for flowing He:CO_2 90:10 (top) and nitrogen (bottom) as the active target and as buffer gas, respectively.

measured with the gauge for the inner volume at the beginning of the experiment was 699.8 torr. During the data collection it read 695.5 ± 0.1 torr. This difference of 4.3 torr is then scaled by (1 + (743 - 699.8)/743) to give 4.5 torr below atmosphere, or about 738.5 ± 0.1 torr. This pressure and the recorded 88° F temperature inside the chamber give a target gas density of 0.3113 kg/m^3.

The target gas was circulated to minimize the possibility of adverse effects on the Micromegas signal due to contaminant buildup in the gas. In contrast, the nitrogen gas wasn't circulated.

As described in Section 4.2.2, the two gases are connected with a bypass valve that breaks when an elevated pressure differential is achieved. The purpose of this valve is to protect the field cage in the scenario where the two gases achieve a pressure differential of about 0.1 atm, or about 76 torr.

4.4 Trigger and Data Collection

As the beam nuclei enter the chamber, many types of scattering and reactions can occur. In order to select the events of interest, a trigger must be implemented. The design of the trigger was constrained by the limited tolerance in trigger rate of the T2K electronics, which is practically around 10 Hz to ensure high live time. For this experiment, the trigger relied on signals from (1) the micromesh of the Micromegas to measure the beam and (2) the pads of the Micromegas to measure reactions.

The signal from the micromesh is not segmented, and it is used in the trigger as a method of determining when a beam particle enters the TPC. A discriminator after the micromesh signal amplifier delivers a 4 μs gate.

Table 4.1: Table of trigger pad locations for each quadrant.

Quadrant	Trigger Pads [Distance from center]
Q1	6 [9.85 mm] 7 [9.85 mm] 15 [24.55 mm]
Q2	6 [9.85 mm] 7 [9.85 mm] 15 [24.55 mm]
Q3	6 [9.85 mm] 7 [9.85 mm] 12 [18.25 mm]
Q4	6 [9.85 mm] 7 [9.85 mm] 15 [24.55 mm]

Table 4.2: Table of high gain pads by quadrant.

Quadrant	High Gain Pads
Q1	15, 20, 25, 30, 35, 40, 45, 50, 55, 60
Q2	15, 20, 25, 30, 35, 40, 45, 50, 55, 60
Q3	12, 20, 25, 30, 35, 40, 45, 50, 55, 60
Q4	15, 20, 25, 30, 35, 40, 45, 50, 55, 60

The trigger scheme for the pad signals takes advantage of the binary nature of the reaction and thus the quadrant design of the Micromegas. Since $\alpha + {}^{10}$Be elastic scattering is a binary event, the quadrant the α particle traverses will always be directly opposite the quadrant that the ^{10}Be traverses. The trigger logic therefore requires coincident signals from opposite quadrants for an event to be identified as binary. The quadrant signals are from pads near the center of the Micromegas, as described in Section 4.2.5 and seen in Fig. 4.14.

Table 4.1 lists the trigger pads used for each quadrant, and Fig 4.30 shows the layout of the trigger pads in a schematic. For Q3, pad 12 is used instead of 15 due to a bad connection of pad 15. Pad 12 was chosen as it was the nearest eligible trigger pad on the ZAP. In order to trigger on the α particles, the gain on the outer-most trigger pads for each quadrant was increased. The higher gain was achieved by biasing the pads to +100 V. The micromesh was held at -245 V.

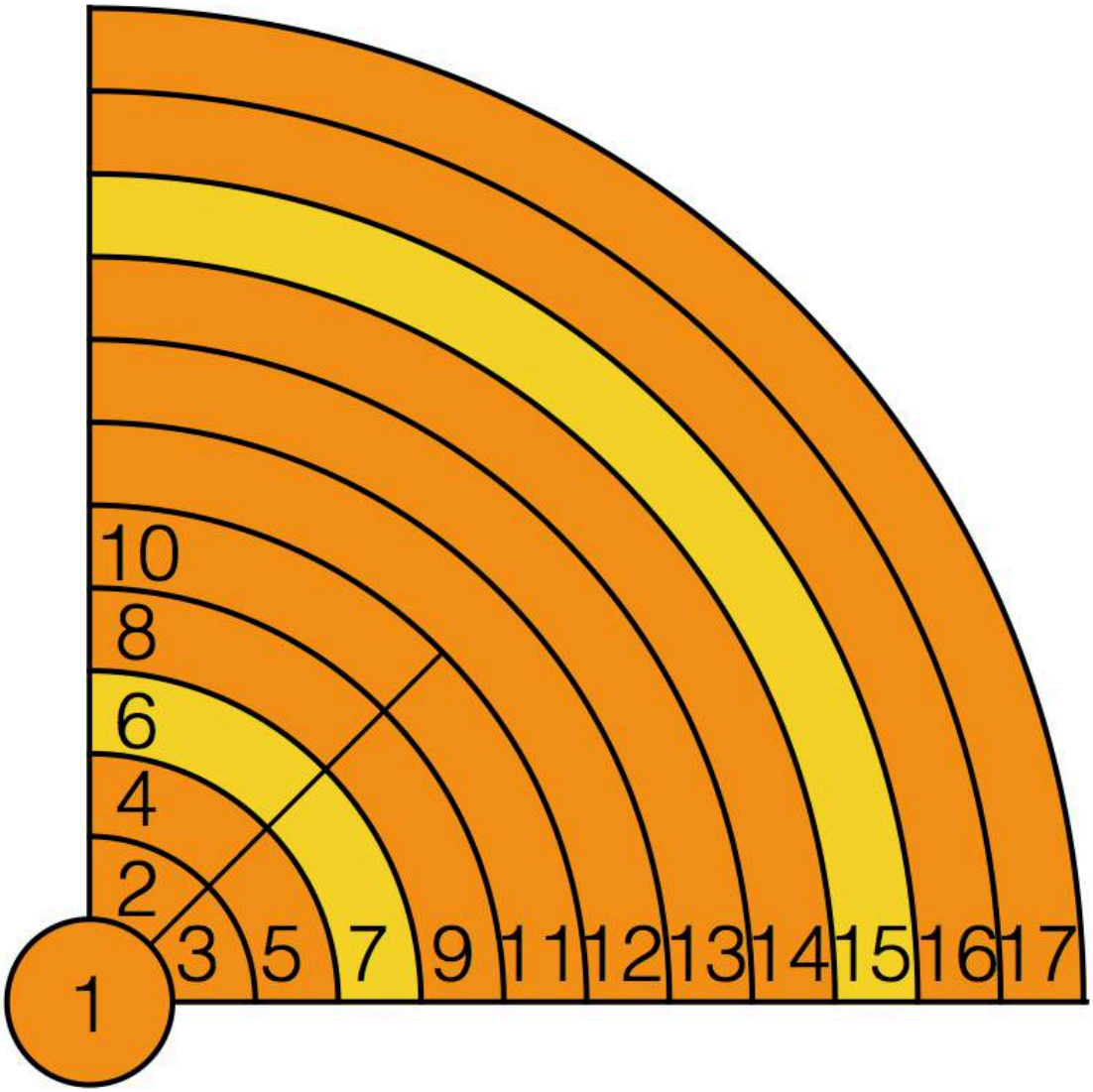

Figure 4.30: Schematic of the first 17 pads of a quadrant of the Micromegas, with trigger pads in yellow. Pad 1 is common to all quadrants. One of the four quadrants uses trigger pads 6, 7, and 12 as it has a bad connection to pad 15.

In addition to the outer-most trigger pads, other pads were also held at a high gain. They are found in Table 4.2. Each high gain pad is spaced 10 mm from its nearest neighbor, except for the first high gain pad in Q3. These pads cover nearly the entire active area of the Micromegas, making the tracking of α particles possible.

If there is a coincidence between Q1 and Q3 or Q2 and Q4 during the gate of the mesh trigger, an Event Trigger is sent to the T2K electronics. This stops the write in the SCA, and is followed by a read of the SCA for all pads. The trigger scheme is show in Fig. 4.31. Typical trigger rates were around 5 to 10 Hz, with live times near 85%.

The analysis performed on the recorded events is discussed in the following chapter.

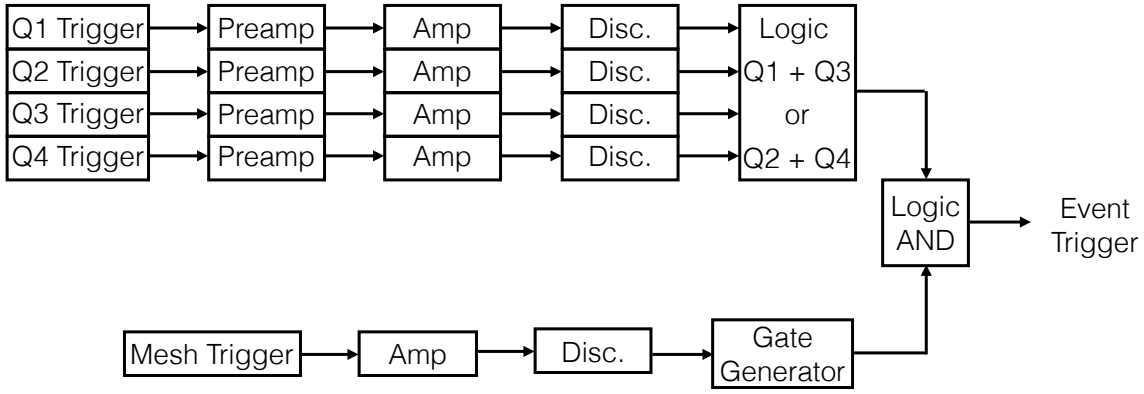

Figure 4.31: The trigger scheme used in this work.

Chapter 5

Analysis

Binary events that are accepted by the trigger are recorded. Software is then used to analyze the events and compute cross sections for the various exit channels of $\alpha + {}^{10}\mathrm{Be}$. This chapter includes discussions on particle identification, energy calibration, angular determination, and cross section calculations.

5.1 Ray Tracing and Angular Determinations

Electrons ionized by charged particles in the field cage drift towards the Micromegas at a velocity of 2.4 cm/μs. By keeping track of the relative time of when the electrons reach the Micromegas and which pads receive an amplified charge, the three-dimensional trajectories of the nuclei are reconstructed. An example of ^{10}Be scattering on ^{4}He is given in Fig. 5.1. The discrete reconstruction of the ^{4}He trajectory in Fig. 5.1 demonstrates the importance of adopting gain variation on individual pads for the reaction trigger. The reaction angles are then calculated.

To calculate the angles, the trajectories are fit with a line, called a ray trace. The ray trace extends from the furthest radial pad with signal back to the center of the beam axis, as seen in Fig. 5.2. These traces are then converted into angles from beam axis with basic trigonometry.

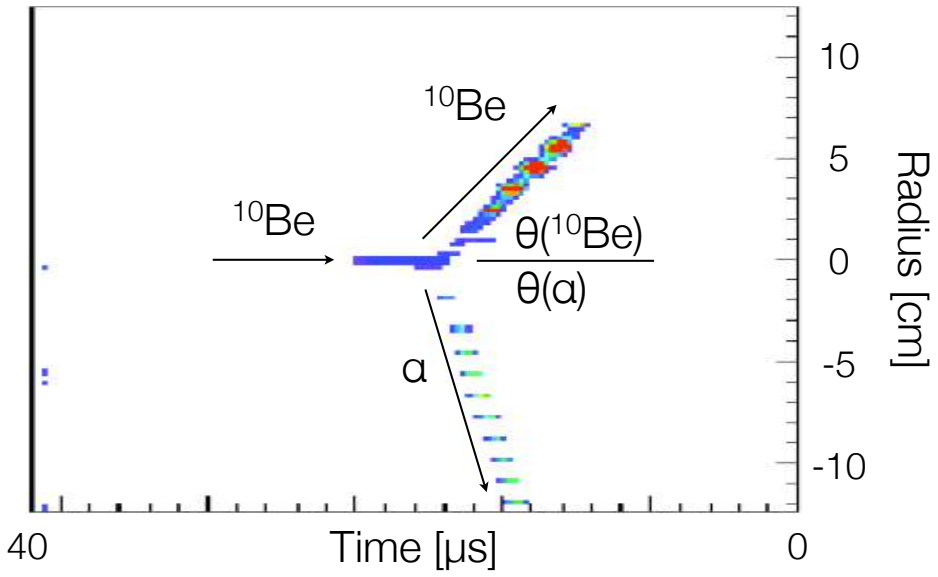

Figure 5.1: Reconstructed trajectories of reaction products in the prototype AT-TPC. The path of the incoming ^{10}Be nucleus is seen, as are the paths of the reaction products ^{10}Be and ^{4}He. The ray traces of the latter two nuclei allow for their angles to be calculated.

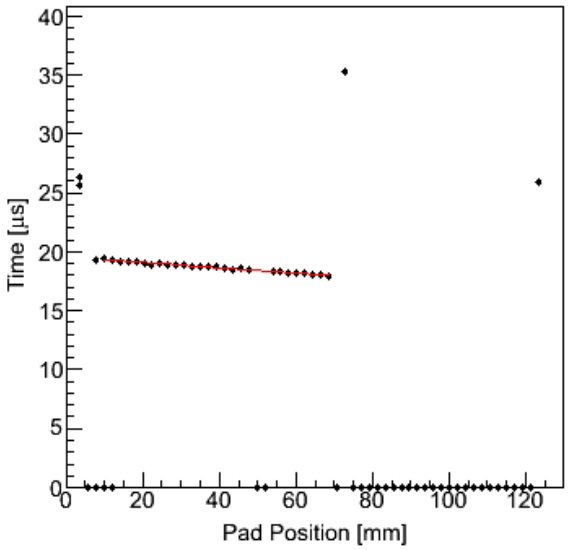

Figure 5.2: A ray trace through pad signals in time for a triggered quadrant. The relative time of each pad signal is denoted by a black diamond. The linear fit is shown in red.

Certain conditions are placed on the ray trace. First, pads within the beam column are excluded from the trace to ensure that signals from the beam or other the reaction product do not affect the trace. For example, the two innermost pads in Fig. 5.2 are excluded for being in the beam column.

Also excluded are signals from pads whose nearest neighbors do not have signal. Such a signal is likely spurious and does not result from the trajectory of the nucleus being traced in the quadrant. For example, the pad signal near 125 mm in Fig. 5.2 is excluded for this reason.

Other spurious signals may be found among pads with real signals, however. In this case, an algorithm is used to sort the signals. From each pad i with signal, a line is drawn to every other pad j with signal, and the slopes of each of these lines are calculated. This calculation is performed for all N pads with signal from $i = 1$ to $i = N$. A standard deviation is calculated for each pad i, defined as

$$\sigma(i) = \sum_j \frac{(m_{j,i} - \overline{m}_{j,i})^2}{N} \tag{5.1}$$

where $m_{j,i}$ is the slope of the line to each pad j from a given pad i and $\overline{m}_{j,i}$ is the average of all such slopes $m_{j,i}$ for a given pad i.

The values of $\sigma(i)$ for each pad i in a trace are then compared. The smallest such value is denoted by $\sigma_<(i)$. By comparing each $\sigma(i)$ to $\sigma_<(i)$, the deviation in time of pad i from the other pads in the trace is determined. If the deviation is too large, the pad is thrown out of the ray trace. The process is then repeated until all signals which deviate too far from

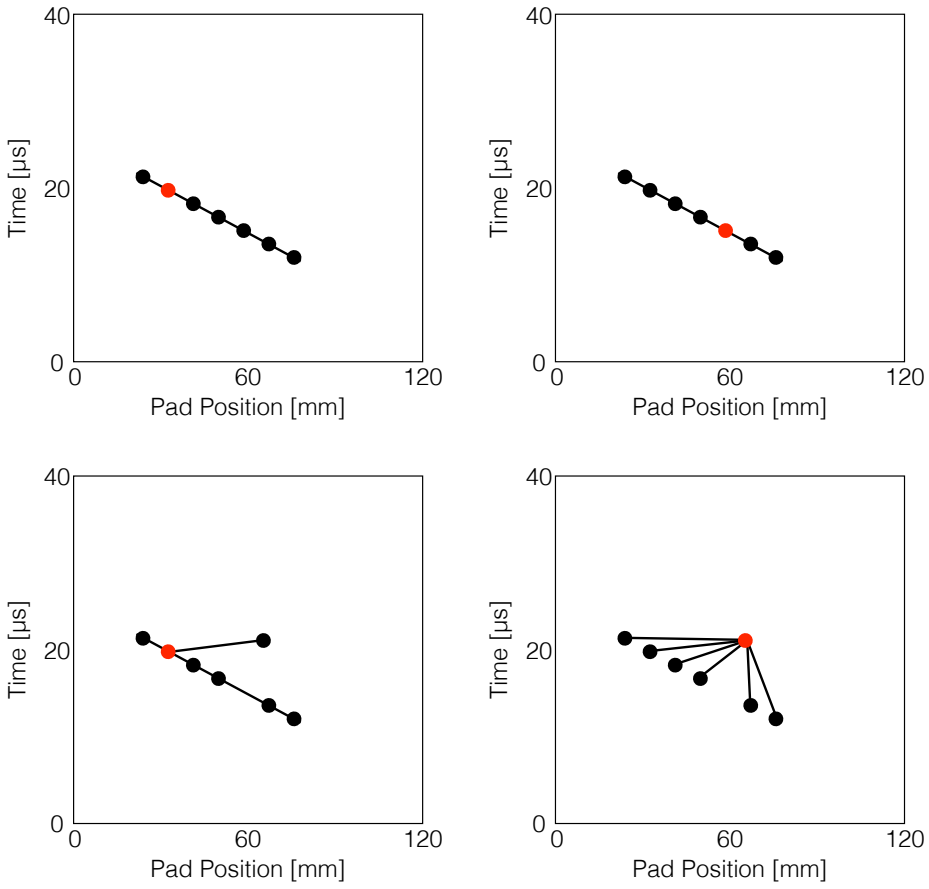

Figure 5.3: Illustrations showing the ray trace algorithm. For each panel, the red dot represents the signal from pad i, from which lines are drawn to each of the other pad signals. The top two panels show that, for a perfect fit, different pads i will results in lines to the other pads that have equivalent slopes. In the bottom panels, however, there is a spurious signal. If drawing from that spurious signal (bottom right panel), the slopes of the lines will all be very different. If drawing from one of the good signals (bottom left panel), only the line to the spurious signal has a slope that is different from the other lines. The algorithm takes advantage of this difference in the slopes of lines betweens pads to exclude a spurious signal like the one seen in the bottom panels.

the ray trace are excluded, at which point a final ray trace is made. Fig. 5.3 illustrates the algorithm. The maximum deviation was empirically determined to be

$$\sigma(i) < \sigma_{<}(i)\frac{N}{2}. \tag{5.2}$$

The threshold set in Eq. 5.2 was chosen to be slightly above the level of standard statistical fluctuations in the signals. In Fig. 5.2, the signal near 70 mm and 35 μs is excluded from the ray trace due to this slope algorithm.

The ray trace is independent of pad signal amplitude and area, that is, it does not depend on the amount of charge deposited on a pad as long as it is above noise. In principle, the amount of deposited charge is proportional to the energy of the nucleus being measured. Thus, measuring the charge allows for the energies of the products to be calculated, which would be a useful tool for identifying particles based on the Bethe formula, Eq. 2.1. In this work, however, the use of high gain pads for triggering makes the calculation of reaction product energies unfeasible. When a ^{10}Be nucleus deposits charge on a high gain pad, the pad becomes highly saturated. Also, pads near the saturated high gain pad pick up some of the signal via crosstalk, further complicating charge calculations. This results in an unreliable calculation of reaction product energies. Therefore, in this work the reaction product energies are not used in analysis.

If ray traces are successfully obtained in opposite quadrants of a triggered event, the angles of the two traces are calculated, as in Fig. 5.1. This procedure is repeated for all triggered events. Then, all calculated angle pairs are put into the matrix seen in Fig. 5.4.

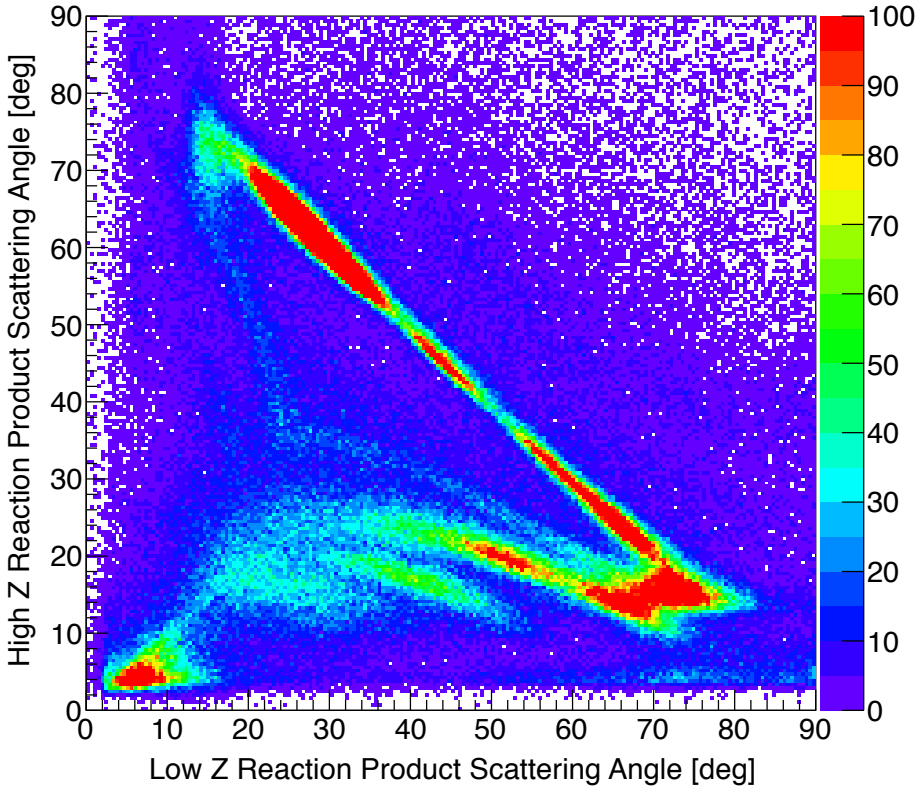

Figure 5.4: Angular data of all events where both reaction products are successfully tracked through the detector volume. The x-axis denotes the angle associated with the reaction product of lower charge Z, while the y-axis is of the higher Z reaction product.

The structures seen in Fig. 5.4 are due to different reactions. By comparing these structures with basic kinematics for various reactions, the reactions for each structure can be identified.

While the reaction product energies are not used in the analysis presented in this work, the deposited charge information in the quadrants is still of use. If the two reaction products of an event are not separable by their charge Z, the structures seen in Fig. 5.4 would be symmetric with respect to the two axes, making kinematic comparisons more difficult. Even with the saturation issues on high gain pads, the difference in deposited charge between two nuclei with different charge Z is measurable. Thus, the matrix in Fig. 5.4 can be filled by considering the relative charge of the two reaction products. When adding an entry to this matrix, the total charge deposited in the two quadrants where the ray traces are made are compared. The reaction product in the quadrant with a larger total charge across all of its pads is labeled as the High Z Reaction Product, and the other reaction product is labeled Low Z Reaction Product.

5.2 Particle Identification

Separating reaction products by their relative charges is only a first step in particle identification. The next task is identifying and separating beam nuclei.

Beam particles of interest in this work are ^{10}Be nuclei. As with most secondary beam facilities, the purity of the beam produced at the Nuclear Science Laboratory at Notre Dame is not perfect. As such, separating the desired beam particles from contaminants is important for distinguishing various nuclear reactions. The isotopes present in the beam in this work include ^{11}B, ^{10}B, ^{10}Be, ^{7}Li, and α particles.

Electrons ionized by beam particles in the field cage drift at a velocity of 2.4 cm/μs. The beam column, the region defined as where the beam signal is measured by the Micromegas, extends from the central pad to pad 15 of each quadrant, resulting in a 4.91 cm diameter. The energy deposit profile read by the Micromegas is recorded over a 40 μs time window, which is about double the full drift time of an electron in the 50 cm cage. The energy deposit profile of a given beam particle is sampled between 1.6 μs and 3.2 μs after the profile is first triggered on the micromesh. This sampling is called the ΔE of the beam, and is shown in Fig. 5.5. For nuclei with different charge and mass, the value of ΔE will be different. Fig. 5.6 shows the separation of beam species by ΔE. While various structures are clearly visible in Fig. 5.6, the identification of these beam nuclei relies on analyzing the kinematics of the structures seen in Fig. 5.4.

A beam stabilization routine was implemented on the ΔE spectrum. This was done to account for possible changes in electron absorption as the active target gas degrades over time in the field cage. The ^{10}Be peak was used as reference for stabilization. An initial center-of-gravity and boundary limits are set on the peak. If a data point filled into the histogram in Fig. 5.6 is located within the boundaries of the target peak, a new center-of-gravity c is calculated based on the value of ΔE and the previous center-of-gravity $c_<$ by the expression

$$c = c_< + \frac{\Delta E - c_<}{N}, \tag{5.3}$$

where $N = 1000$ is a constant weight. The ratio of the new and old center-of-gravity values is called the gain $g = c/c_<$. The boundaries of the target peak are then scaled by this gain. If,

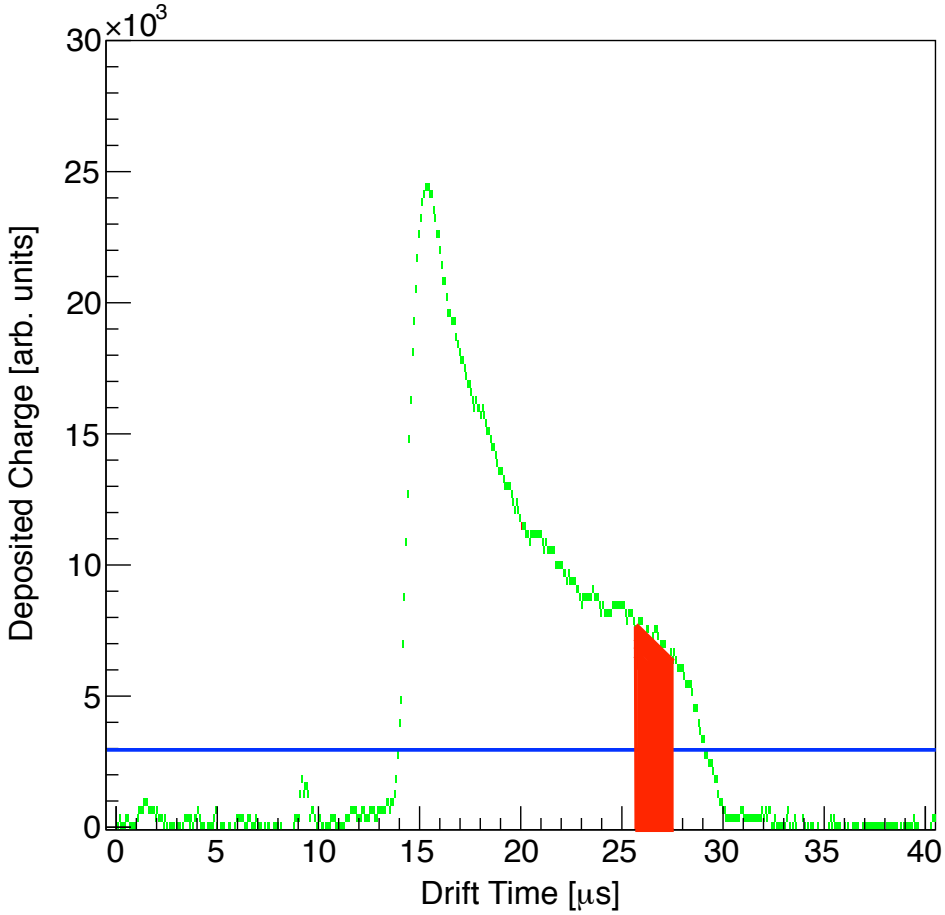

Figure 5.5: Plot of the energy deposit profile of a beam particle, in green. The horizontal blue line at 3,000 represents the amplitude threshold. The red region represents the ΔE sampling for beam particle determination. The shape of the energy deposit profile is described by a Bragg curve. The value of ΔE is different for different nuclei. A histogram of ΔE values is shown in Fig. 5.6.

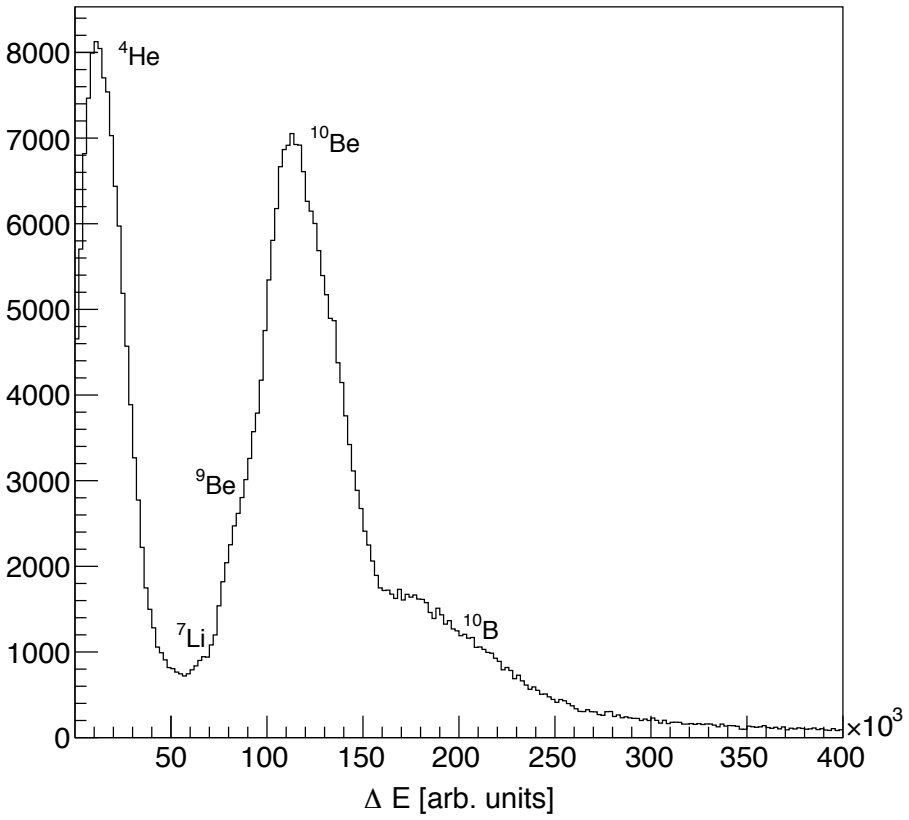

Figure 5.6: Histogram of beam species, as gated by ΔE after beam stabilization. The identification of the various species labeled in this plot is done by comparison to the kinematics of reactions with target ^{4}He particles in the angular correlations matrix.

however, the data point is outside of the boundaries, its ΔE is simply scaled by the current gain value. This process is then repeated for all events that fill the histogram, and it corrects for the slow drift in pulse height due to gas degradation.

For example, consider the first peak in Fig. 5.6 from 0 to 50,000. When plotting angular correlations with a gate on this peak, the data seen in Fig. 5.7 are obtained. Overlaying kinematics curves on the matrix reveals the two particles in the reaction. In this case, both particles are ^{4}He, meaning that the first peak Fig. 5.6 is a ^{4}He beam contaminant.

The identification of a ^{4}He beam contaminant is useful in verifying the calibration of the calculation of angles of the two reaction products. For $^4\mathrm{He} + {}^4\mathrm{He}$ elastic scattering, the sum of the two angles must be 90°. The data in Fig. 5.7 nicely follow this sum rule, confirming the suitability of the ray tracing method described in Sec. 5.1.

This comparison of kinematics is done for all of the peaks seen in Fig. 5.6. Further examples are given in Fig. 5.8 and Fig. 5.9, the latter of which reveals both elastic and inelastic scattering of ^{10}Be on ^{4}He.

The separation of elastic and inelastic scattering in Fig. 5.9 is particularly important for this work, as it allows for separate analysis of the two exit channels. The black curve in Fig. 5.9 represents elastic scattering, and the red curve shows inelastic scattering to the first excited state in ^{10}Be, which is a 2^+ state at 3.368 MeV. There are higher lying inelastic states as well. The data for these states are seen as a grouping near 15° in ^{10}Be and 25° in ^{4}He. Currently, they haven't been further investigated as separating these unbound states has proven difficult due to their natural widths and low statistics. Thus, for convenience, when further instances of inelastic data are mentioned, they refer only to the first inelastic state, as shown in the red kinematical curve.

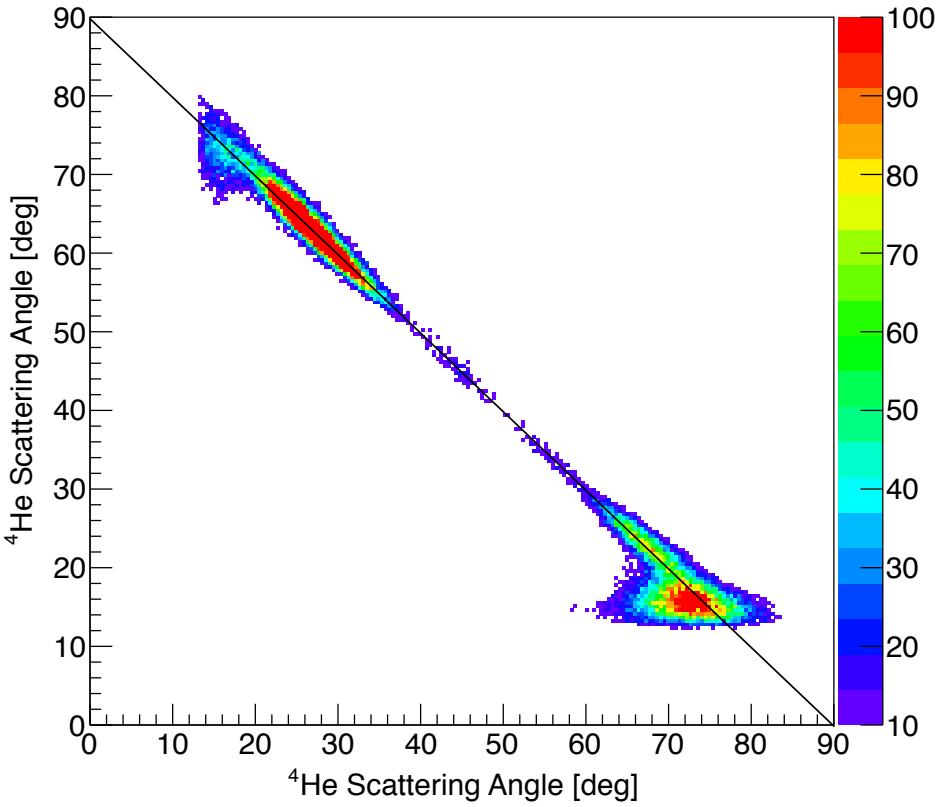

Figure 5.7: Angular data of events gated on the ^{4}He peak in Fig. 5.6. The kinematics curve for elastic scattering overlays the data in black. The ^{4}He + ^{4}He scattering data are useful for confirming calibration of the angles of the two reaction products.

Analysis of ΔE of the beam and reaction kinematics has resulted in the separation of elastic and inelastic ^{10}Be scattering on ^{4}He from other triggered events. Next, the determination of the reaction energy will be discussed.

5.3 Energy Calibration

To determine the energy at which a reaction occurs, the location of the reaction along the beam axis must be determined. This location, called the reaction vertex, represents the distance the ^{10}Be beam particle has traveled through the active target before interacting

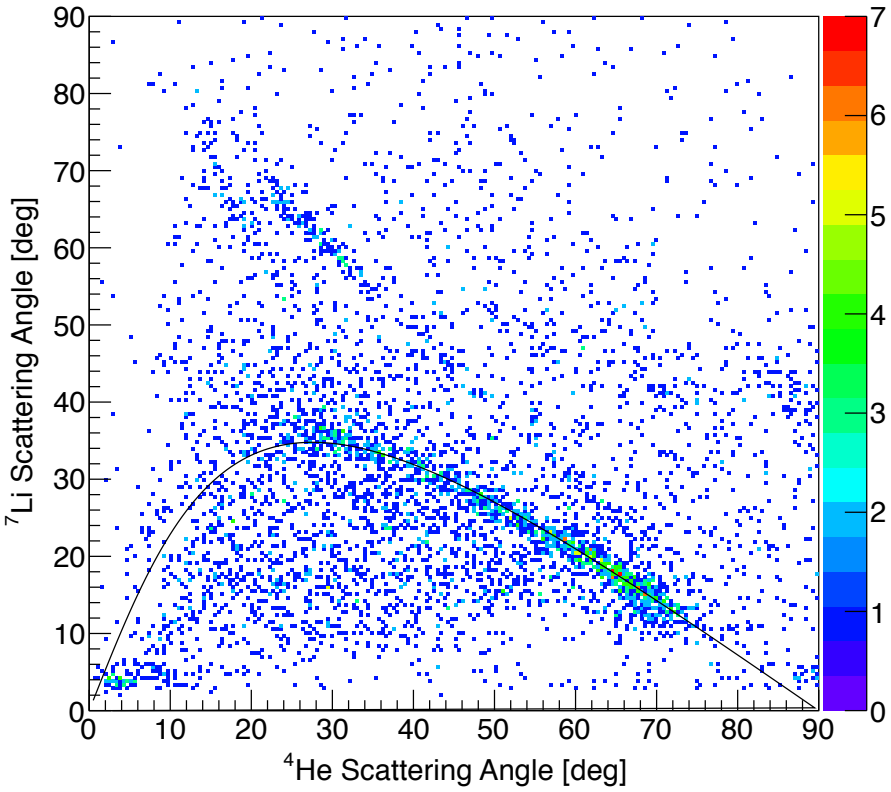

Figure 5.8: Angular data of events gated on the ^{7}Li peak in Fig. 5.6. The kinematics curve for elastic scattering overlays the data in black.

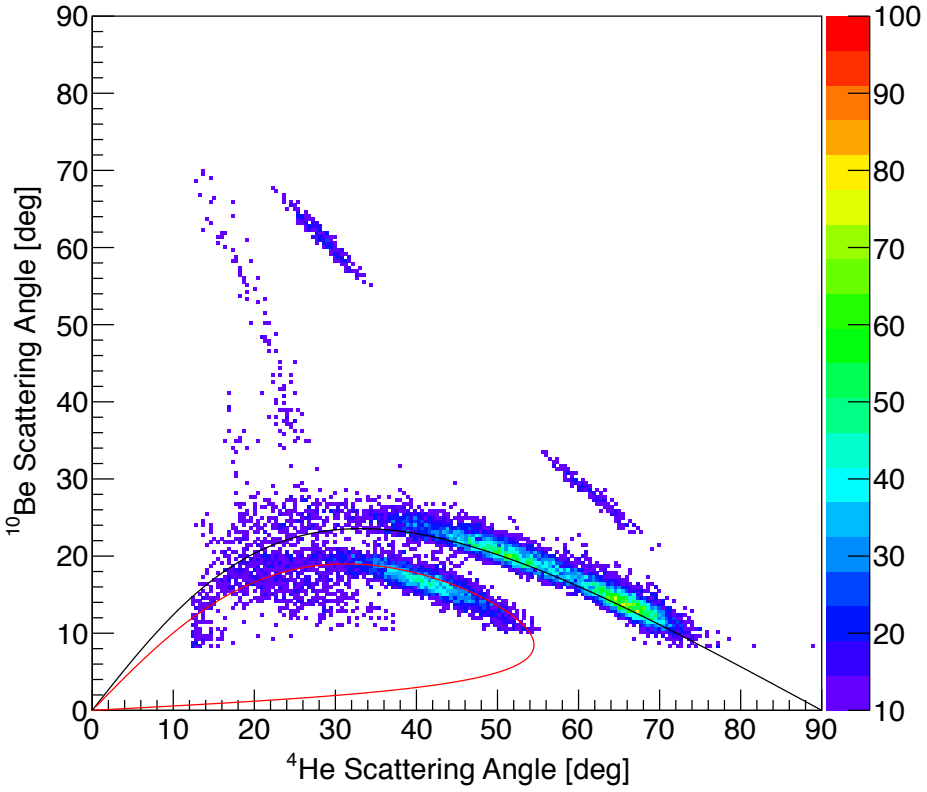

Figure 5.9: Angular data of events gated on the ^{10}Be peak in Fig. 5.6. Kinematics curves overlay the data: elastic scattering is in black, and the first excited state (3.368 MeV in ^{10}Be) inelastic scattering is in red.

with a target ^{4}He nucleus. Thus, the reaction vertex can be converted into an energy by comparing it to energy loss calculations of ^{10}Be in He:CO_2 90:10 of density 0.3113 kg/m^3. First, however, the energy of the incoming beam particle must be determined. Both of these calibrations are described below.

5.3.1 Beam Energy Calibration

The beam energy was measured at the location of the beam window into the active target volume with a Position Sensitive Silicon Detector (PSSD), described in Sec. 4.3.2. The ^{10}Be beam energy, as measured by the PSSD, was found to be $39.0^{+0.50}_{-0.25}$ MeV. This is the energy incident on the beam window, and after accounting for the energy loss in the window, the energy becomes 38.2 ± 0.5 MeV. The energy loss in the window was computed using SRIM (the Stopping and Range of Ions in Matter), which is software that calculates the transport of ions in matter based on experimental databases [67, 68].

The value of this beam energy as measured by the PSSD was checked by measuring the penetration depth of the various beam particles in the active target and comparing the depths to SRIM and LISE++ calculations. LISE++ is software [69, 70] that, among other features, is used to calculate penetration depth of ions in matter, similar to SRIM. Both softwares are commonly used for this purpose. Thus, comparing calculations with each software provides an independent beam calculation from that of the PSSD.

Data were taken without the binary reaction trigger, and instead just with a micromesh trigger on the beam. There are two main beam components seen in the spectrum: ^{10}Be and ^{10}B. They were identified by their ΔE values seen in Fig. 5.10. Lighter beam particles, such as ^{4}He and ^{7}Li contaminants seen in Fig. 4.26, did not trigger the micromesh as they have a lower charge than ^{10}Be, which is the nucleus the trigger level was set to measure. A 4^+

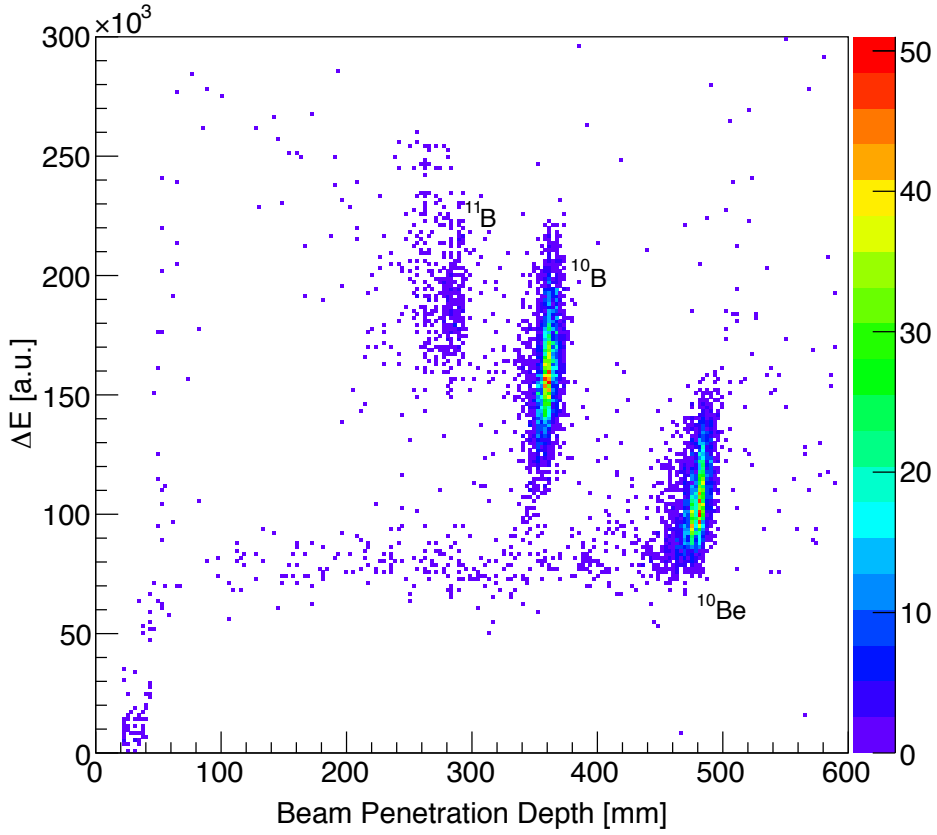

Figure 5.10: Two dimensional histogram of beam particles. While the ^{10}B particles stop in the chamber, the ^{10}Be particles punch through.

charge state is assumed for ^{10}Be and B isotopes. The data in Fig. 5.10 are then projected onto the x-axis for determination of penetration depth in the active target volume, as seen in Fig. 5.11. While present in both figures, the ^{11}B isotopes were not used for calibration of ^{10}Be as analysis of the low statistics ^{11}B contaminant was not necessary considering the strong presence of ^{10}B.

In Fig. 5.11, the penetration depth of ^{10}B beam particles is 360 ± 5 mm, while it is 480 ± 5 mm for ^{10}Be particles. However, this 480 mm depth is the full length of the chamber, which suggests that the ^{10}Be beam does not stop in the active target gas. To calculate its energy, a calculation must first be made on ^{10}B. With a penetration depth of 360 mm, the

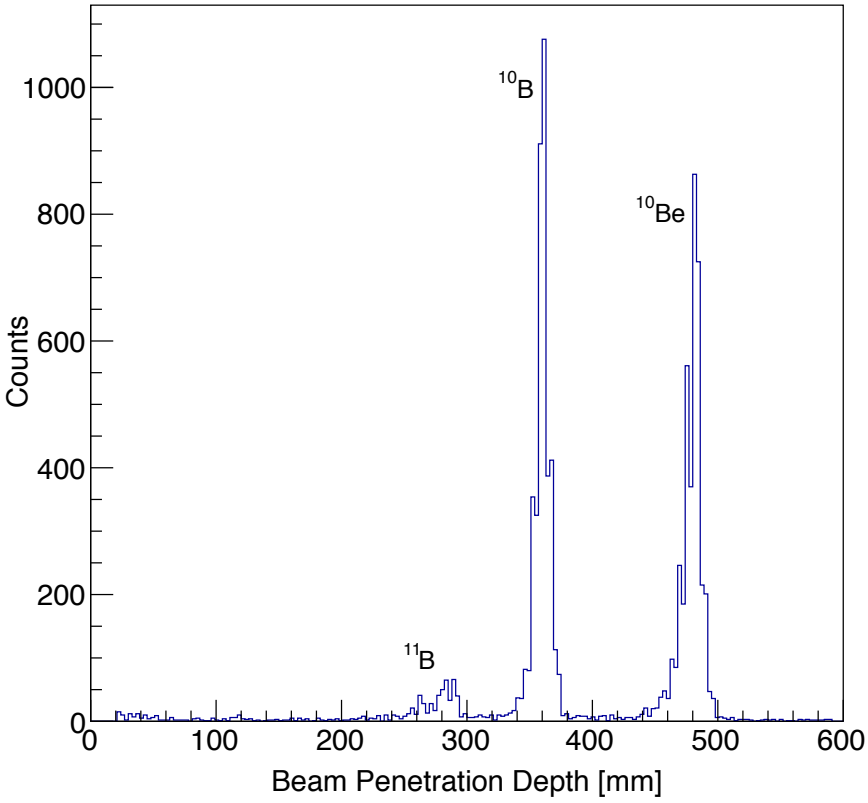

Figure 5.11: Projection of Fig. 5.10 onto the x-axis. The penetration depth of ^{10}B is 360 ± 5 mm and is 480 ± 5 mm for ^{10}Be, though this latter value reflects the total active target volume length and not the stopping distance of ^{10}Be.

^{10}B beam energy after the window was calculated using SRIM to be 40.150 MeV. Making a calculation of the energy before the beam window gives 41.335 MeV. Since TwinSol selects nuclei by their charge-to-mass ratio, or $B\rho$ value, ^{10}Be has the same energy as ^{10}B when incident on the window since it has the same mass and 4^+ charge state. The energy loss of ^{10}Be is less in the window due to its lower charge, and results in an energy of 40.554 MeV after the foil, which would have a penetration depth of 537.9 mm if the chamber were long enough to contain it.

Using LISE++, the ^{10}B energy was found to be 39.399 MeV after the window, and 40.539 MeV before it. The same energy in ^{10}Be results in an energy of 39.79 MeV after the window with a total range of 541.9 mm.

The particle track length approach to calculating beam energy is not as precise as the $E - \Delta E$ method of the PSSD, and since the values of 39.79 MeV and 40.55 MeV from LISE++ and SRIM, respectively, are quite similar to the value of 38.2 ± 0.5 MeV from the PSSD, the PSSD value is adopted as the calibrated beam energy of ^{10}Be. This implies an estimated energy uncertainty in the center-of-mass frame of $0.5 \times 4/14 = 0.14$ MeV.

5.3.2 Reaction Energy Calibration

With the energy of the ^{10}Be beam after the window calibrated, the reaction energy of data can be calculated. A SRIM calculation is made to convert the reaction vertex to the beam energy as a function of penetration depth. The penetration depth is defined as the difference in distance between the entrance of the beam particle into the active target and the reaction vertex. The particle entrance is determined by the first signal over threshold of the incoming beam particle, as shown in Fig. 5.5. Then, calculating the reaction vertex gives, via SRIM, the reaction energy.

The vertex of a given reaction is computed by taking the beam axis intercept of the reaction product ^{4}He ray trace. An average of the intercepts of both ^{10}Be and ^{4}He ray traces for a given event was considered, but the shorter paths of the ^{10}Be particles result in a less precise ray trace than ^{4}He. Thus, only the ^{4}He ray trace intercept is used to compute the vertex. Uncertainty in the calculation is 20 mm with the preferred method, while using an average results in an uncertainty a few mm larger.

5.4 Cross Section and Excitation Function Calculations

With energies and angles calculated and calibrated in the lab frame, they must be converted into the center-of-mass frame in order to compute cross sections and excitation functions. The acceptance of the detector, beam rate, and detector live time must also be taken into account.

5.4.1 Energy and Angle Frame Conversion

Converting energy to center-of-mass is quite simple. The conversion depends only on the masses of the system and the beam energy in the lab frame, defined as

$$E_{\mathrm{CM}} = \frac{m_{^4\mathrm{He}}}{m_{^4\mathrm{He}} + m_{^{10}\mathrm{Be}}} E_{\mathrm{Lab}} = \frac{2}{7} E_{\mathrm{Lab}}. \tag{5.4}$$

Converting angles from lab to center-of-mass is more complicated, however. The expression below is derived from energy and momentum conservation, and it is fully relativistic. The center-of-mass angle is defined as

$$\tan\theta_{\mathrm{CM}} = \begin{cases} \alpha, & \text{if } \alpha \geq 0 \\ \pi - \alpha, & \text{otherwise} \end{cases} \tag{5.5}$$

for

$$\alpha = \frac{P_3 \sin\theta_3}{\gamma\left(P_3\cos\theta_3 - \beta\sqrt{m_3^2 + P_3^2}\right)} \tag{5.6}$$

where

$$\beta = \frac{\sqrt{E_{\mathrm{Lab}}^2 + 2m_1E_{\mathrm{Lab}}}}{m_1 + m_2 + E_{\mathrm{Lab}}} \tag{5.7}$$

$$\gamma = \frac{1}{\sqrt{1-\beta^2}} = \frac{m_1 + m_2 + E_{\mathrm{Lab}}}{\sqrt{2m_2E_{\mathrm{Lab}} - (m_1+m_2)^2}} \tag{5.8}$$

$$P_3 = \frac{\sin\theta_4\sqrt{E_{\mathrm{Lab}}^2 + 2m_1E_{\mathrm{Lab}}}}{\sin(\theta_3+\theta_4)} \tag{5.9}$$

where E_{Lab} is the lab frame beam energy and the masses m_1, m_2, m_3, and m_4 refer to the the incident ^{10}Be beam particle, the at-rest ^{4}He target particle, the ^{4}He recoil particle, and the ^{10}Be ejectile, respectively. Similarly, the lab angles are labeled as θ_3 for the recoil and θ_4 for the ejectile. All expressions use units of $\hbar = c = 1$.

For elastic scattering, the center-of-mass angle does not depend on reaction energy, and can be calculated from the ^{4}He recoil angle θ_3 alone, provided the target nucleus is at rest in the lab frame. In this case, the center-of-mass angle in the non-relativistic approximation is

$$\theta_{\mathrm{CM}} = 2\left(\frac{\pi}{2} - \theta_3\right). \tag{5.10}$$

Thus, Eq. 5.10 was used for elastic data, and Eq. 5.5 was used for the inelastic data.

5.4.2 Acceptance Calculation

Reactions that take place in the active target do not all have an equal likelihood of being measured. For example, the paths of the reaction products may simply have angles that are so far forward that the products do not escape the beam column as they travel through the gas, resulting in a lack of trigger. Also, if a reaction occurs at a very low energy, the two reaction products may simply have kinetic energies that are so low that the particles' ranges are too short to traverse trigger pads on the Micromegas. To account for these situations, pictured in Fig. 5.12, acceptance calculations of elastic and inelastic scattering in the chamber were made. These acceptance calculations are then used to normalize the cross section calculations.

The acceptance calculations, one each for elastic and inelastic scattering of ^{10}Be on ^{4}He, are Monte Carlo simulations. In a calculation, the detector volume and gas are defined as found in the experimental setup, and $N = 1,000,000$ reactions are simulated inside of it at random energies and angles. The energy losses of the particles in the simulation are obtained from SRIM calculations. A trigger is set in the simulation to mimic that of the actual detector. The trigger used in the simulation requires both reaction products to reach the first trigger pad in their respective quadrants. The probability of simulated reactions in a given energy bin and angular bin to pass the simulation's trigger condition gives the

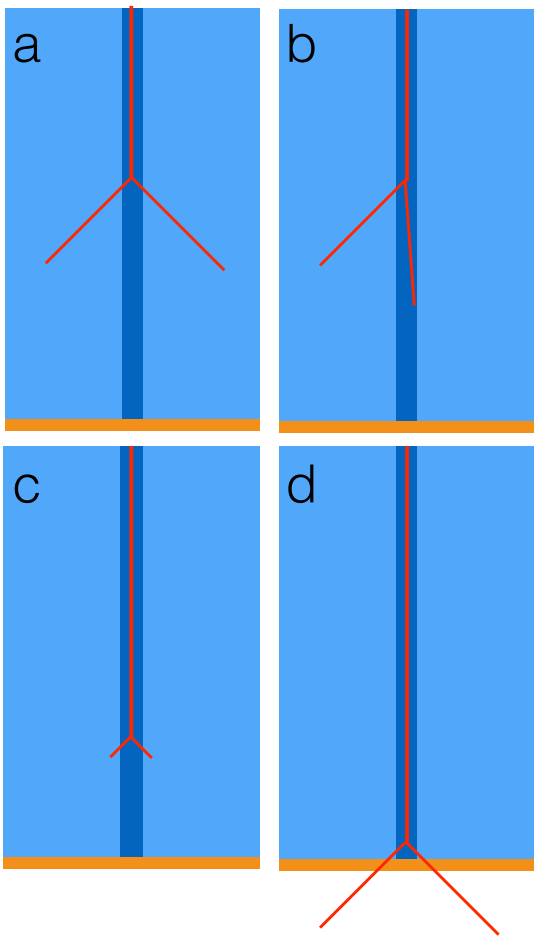

Figure 5.12: Four plots of possible reaction scenarios. All figures depict particle trajectories in red, a blue active target volume, a dark blue beam column, and an orange Micromegas plane at the bottom of the volume. Fig. 5.12(a) shows a binary reaction that would successfully trigger the electronics and thus would be recorded. Fig. 5.12(b) would not trigger as one of the reaction products has too small of an angle to leave the beam column. In Fig. 5.12(c), the energy of the reaction is low so that the reaction products do not travel over trigger pads, resulting in the event not being recorded. The reaction in Fig. 5.12(d) takes place so close to the Micromegas that the products quickly leave the chamber and are thus not detected. The acceptance calculation described in this section accounts for these various scenarios for the normalization of the elastic and inelastic reaction cross sections.

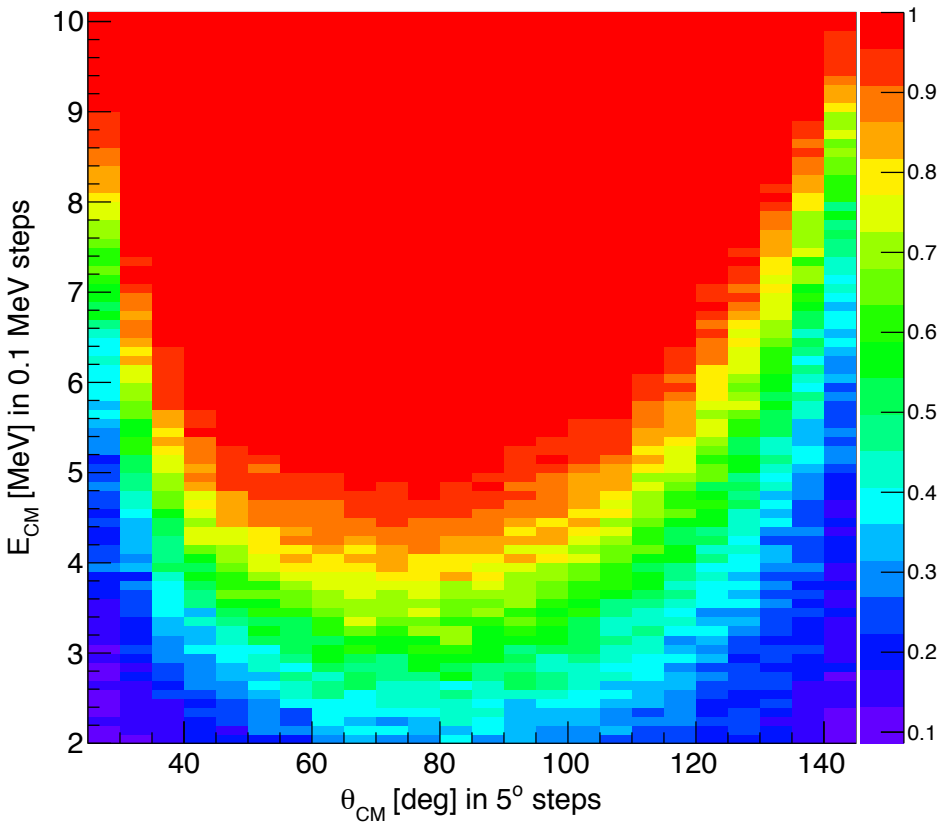

Figure 5.13: Acceptance calculation for elastic scattering of ^{10}Be on ^{4}He. The color scale represents the probability that a reaction at a given center-of-mass energy and angle would be recorded.

detector acceptance for reactions at such energies and angles. The acceptances for elastic and inelastic scattering are plotted for center-of-mass energies and angles in Fig. 5.13 and Fig. 5.14, respectively.

The simple trigger used in the acceptance calculations does not fully replicate the trigger system of the experiment. Thus, the calculations are not fully reliable in regions where acceptance is low, such as angles far from 90° and for low energies. An absolute uncertainty of 10% is assumed for the calculations.

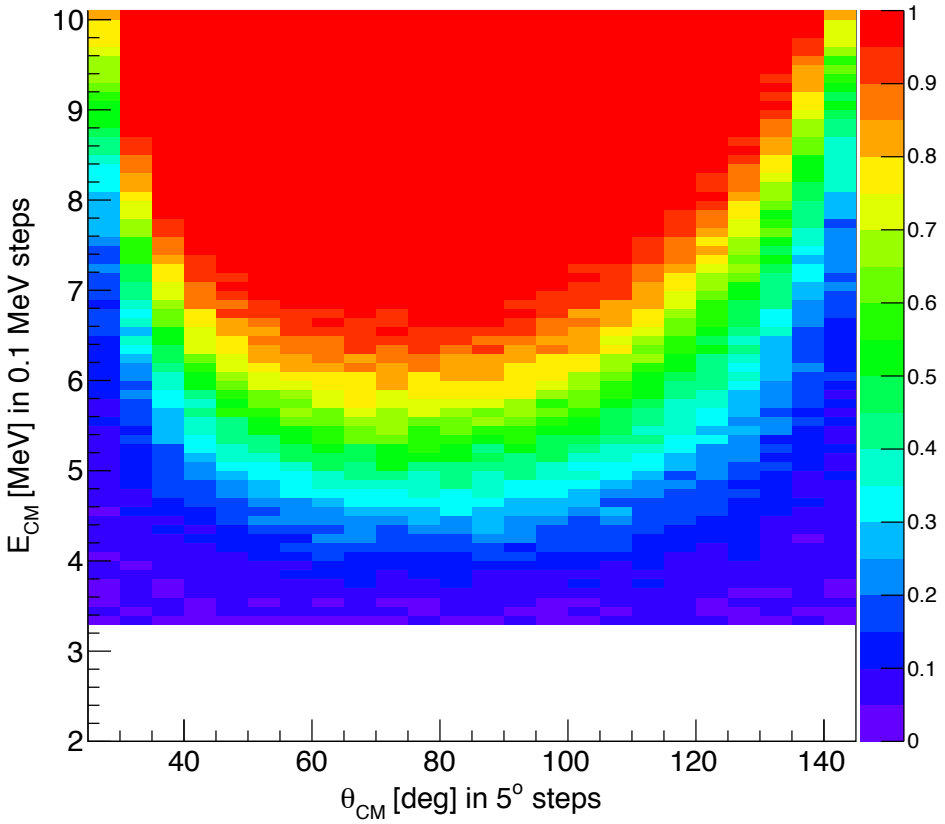

Figure 5.14: Acceptance calculation for inelastic scattering of ^{10}Be on ^{4}He. The color scale represents the probability that a reaction at a given center-of-mass energy and angle would be recorded if it were to take place in the detector. The energy cutoff seen in the plot is due to the 3.368 MeV excitation energy of the first excited state in ^{10}Be.

5.4.3 Elastic and Inelastic Cross Sections and Excitation Functions

With the calculated detector acceptance and the center-of-mass energies and angles calibrated, elastic and inelastic cross sections and excitation functions can be computed.

The experimental cross section, adapted from Eq. 1.15, is calculated separately for elastic and inelastic scattering as

$$\sigma(\theta) = \frac{N}{\epsilon_{\mathrm{DAQ}}\epsilon_{\mathrm{det}} N_{\mathrm{inc}} n_t \; 2\pi \sin\theta \Delta\theta} \; , \tag{5.11}$$

where N is the number of reactions at angle θ within an angular bin of width $\Delta\theta$, N_{inc} is the number of incident nuclei, n_t is the number of target nuclei per unit area, ϵ_{DAQ} is the data acquisition efficiency, and ϵ_{det} is the detector acceptance from the Monte Carlo simulation described above in Sec. 5.4.2. These values are defined as follows:

$$\begin{aligned} N_{\mathrm{inc}} &= f_{\Delta E}\left(^{10}\mathrm{Be}\right) N_{\mathrm{TPC}} \\ &= 0.571 \cdot 558,872,962 \\ &= 319,116,461 \end{aligned} \tag{5.12}$$

where $f_{\Delta E}\left(^{10}\mathrm{Be}\right)$ is the fraction of beam particles identified as ^{10}Be by ΔE in Fig. 5.6 and N_{TPC} is the number of total beam particles that triggered the micromesh in the prototype AT-TPC;

$$n_t = \rho dx = \rho(dx/dE)\Delta E \tag{5.13}$$

where $\rho = 2.15 \times 10^{19}$ 1/cm^3 is the target gas density, dx/dE is the energy loss function of ^{10}Be in He:CO_2 90:10 as calculated in SRIM, and ΔE is the energy bin;

$$\begin{aligned} \epsilon_{\text{DAQ}} &= \frac{\text{TimeLive}}{\text{Time100}} \\ &= \frac{\text{Time100 - DeadTime}}{\text{Time100}} \\ &= \frac{33,577,009}{38,416,240} \\ &= 0.874 \end{aligned} \tag{5.14}$$

where Time100 is the total amount of time the data acquisition (DAQ) electronics is running, DeadTime is the time during which the DAQ is processing data and not accepting new trigger events, and TimeLive is the amount of time the data acquisition electronics is accepting new trigger events.

By filling a histogram of energy and angular bins with values calculated from Eq. 5.11, the cross sections of the elastic and inelastic channels are obtained. The elastic scattering data are shown in Fig. 5.15; the inelastic are given in Fig. 5.16.

In both cross section plots, resonances are present. To analyze these resonances, projection onto each axis are made. Projections onto the x-axis yield differential cross sections for a given energy bin, while y-axis projections produce excitation functions for a given angular bin. These projections are useful for comparing the data to theoretical calculations, which

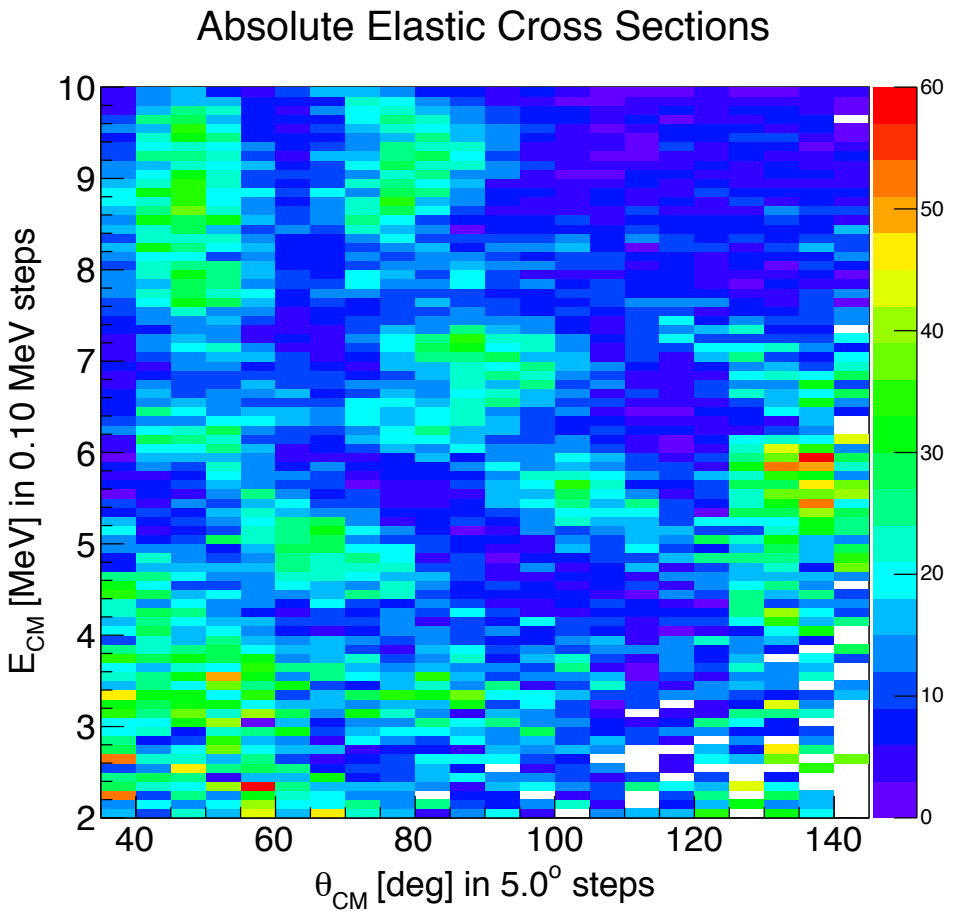

Figure 5.15: Normalized experimental elastic cross section as a function of energy and angle, given in mb/sr.

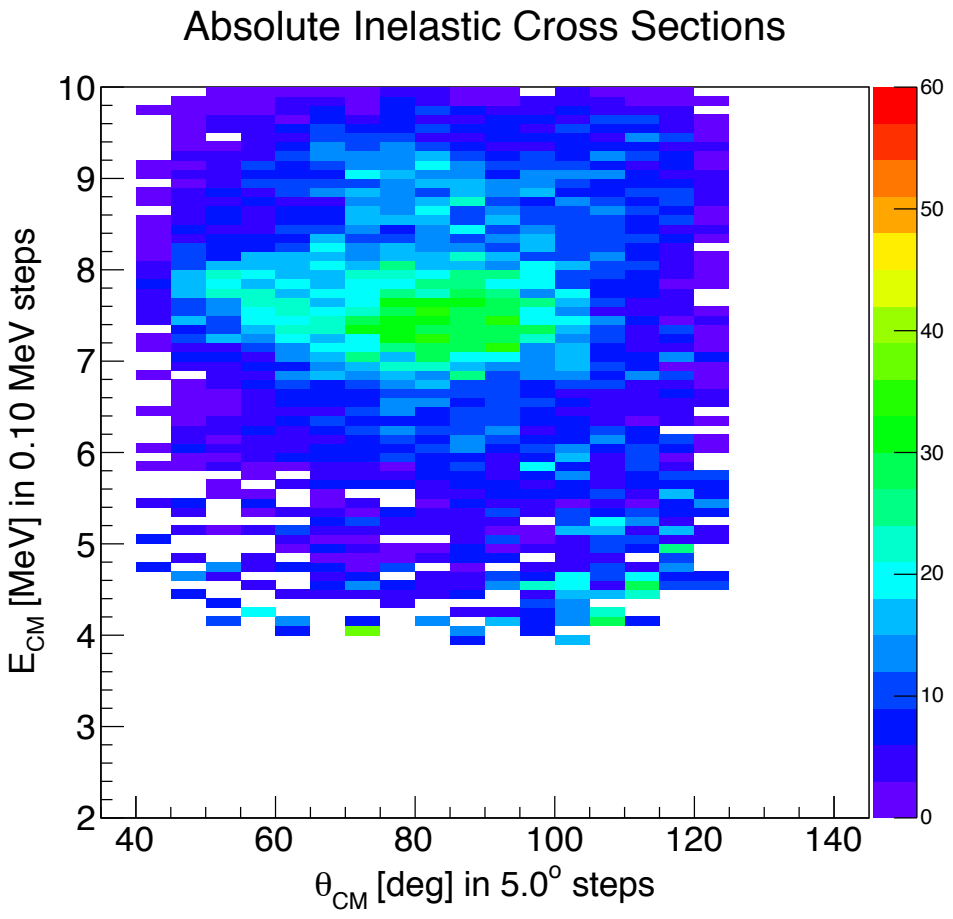

Figure 5.16: Normalized experimental inelastic cross section as a function of energy and angle, given in mb/sr.

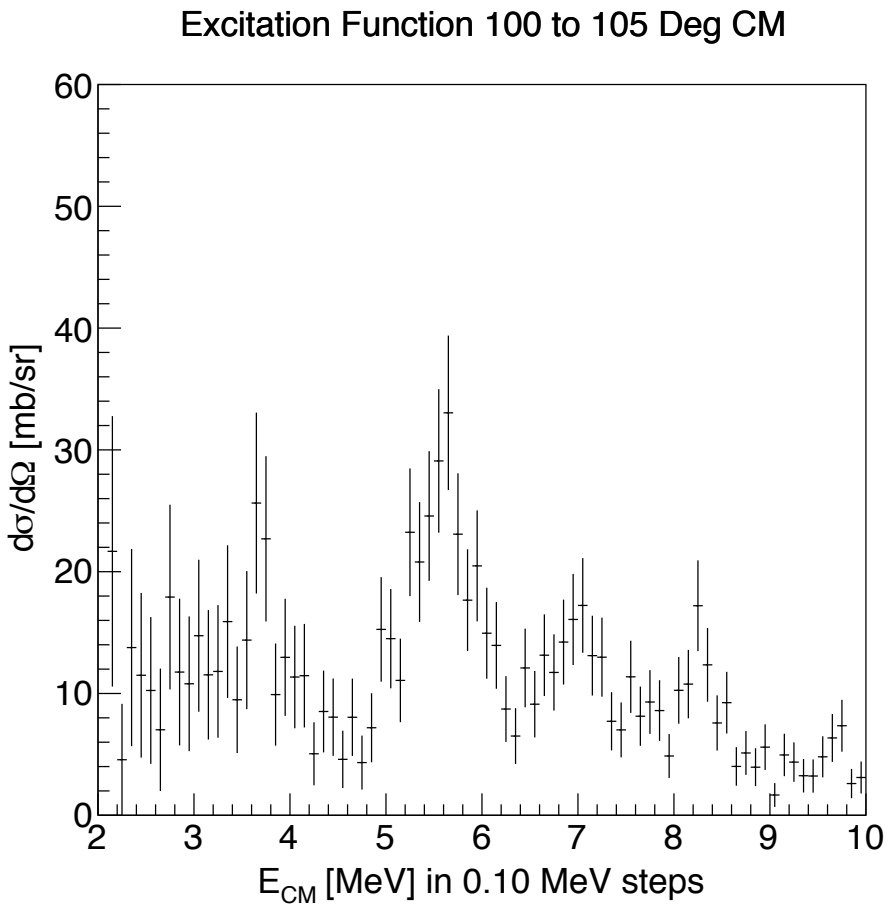

Figure 5.17: Elastic excitation function from 100° to 105°, a projection onto the y-axis from Fig. 5.15. An x-axis projection produces an angular cross section plot. The uncertainties are calculated from Eq. 5.15.

will be discussed in the following section. An example excitation function from elastic data is shown in Fig. 5.17.

The projections include an uncertainty in the cross section values. This uncertainty is defined, for each energy bin i and angular bin j, as

$$\Delta\sigma_{i,j}(E,\theta) = \sigma_{i,j}(E,\theta)\sqrt{(\Delta\epsilon_{\text{det}})^2 + \left(\frac{\sqrt{N_{i,j}}}{N_{i,j}}\right)^2 + \left(\frac{\sigma_{s.d.}(N_{\text{inc}})}{N_{\text{inc}}}\right)^2} \tag{5.15}$$

for an acceptance uncertainty of $\Delta\epsilon_{\text{det}} = 0.1$, number of counts per energy and angular bin $N_{i,j}$, and the number of incident ^{10}Be beam particles N_{inc}. The uncertainty in N_{inc} is given by the standard deviation of various beam measurements taken over the course of the experiment. For each beam measurement, the percentage of ^{10}Be beam particles was calculated based on the ΔE spectrum. The standard deviation of these percentages of all the beam measurements is called $\sigma_{s.d.}(N_{\text{inc}})$, and it is included in Eq. 5.15 with a value of $\sigma_{s.d.}(N_{\text{inc}})/N_{\text{inc}} = 0.0283/0.571 = 0.0496$.

5.5 Theoretical Calculations

Theoretical calculations to compare to the data are done in the following manner:

1. A non-resonant elastic scattering calculation is made based on the São Paulo (SP) potential, an optical model potential.

2. An elastic R-matrix calculation is made without any resonances and matched to the output of the SP calculation.

3. Resonances are added to the R-matrix elastic calculation and compared to the elastic data.

4. A similar R-matrix calculation is then made to compare to the inelastic data.

5. Spins and parities are assigned to the elastic and inelastic resonances, and their widths Γ_{res} and spectroscopic factors SF are computed.

6. The relevance of the resonance assignments to ^{14}C cluster predictions are discussed.

The following subsections will describe these points in detail.

5.5.1 São Paulo Optical Model Calculation

Before making theoretical calculations of the resonances seen in the data, a reliable description of Coulomb and nuclear elastic scattering is desired. An optical model (see Sec. 1.6) calculation is made based on the São Paulo (SP) potential [71]. The code used to make this calculation was provided by Luiz Chamon of the Departamento de Física Nuclear, Instituto de Física da Universidade de São Paulo.

Within the SP model, the nuclear interaction between two nuclei is described with a density-dependent folding potential and energy-dependent exponential term as

$$V_N(R, E) = V_F(R) e^{-4V^2/c^2}, \tag{5.16}$$

where c is the speed of light. The velocity relates to the energy by

$$V^2(R, E) = \frac{2}{\mu}[E - V_C(R) - V_N(R, E)] \tag{5.17}$$

for the reduced mass μ of the system and Coulomb potential V_C. By iteratively solving Eq. 5.16 and Eq. 5.17, the SP potential is obtained. The folding potential is defined as

$$V_F(R) = \int \rho_1(\boldsymbol{r}_1)\rho_2(\boldsymbol{r}_2)V_0\ \delta(\boldsymbol{R} - \boldsymbol{r}_1 + \boldsymbol{r}_2)d\boldsymbol{r}_1 d\boldsymbol{r}_2, \tag{5.18}$$

where $V_0 = -456$ MeV $\cdot$ fm^3, $\boldsymbol{R}$ is the relative displacement vector of the two nuclei, and $\boldsymbol{r}_1$ and $\boldsymbol{r}_2$ are the radii of the two nuclei [71]. The nuclear density is modeled as a Fermi distribution [72]

$$\rho(r) = \frac{\rho_0}{1 + \exp\left(\frac{r - R_0}{a}\right)}. \tag{5.19}$$

Matter and charge densities are both computed, and they have average diffuseness values of $a = 0.56$ and 0.53 fm, respectively. These densities are calculated without any adjustable parameters, meaning that the resulting cross sections are predictions and not fits to data, an important characteristic of the SP potential [71].

For this work, the SP potential is used for the real part of the optical model. The value of the imaginary term is set as a scaled value of the real depth. Multiple scaling factors around the value of $W = 0.8V_N$ suggested in Ref. [71] were considered, with the suggested value ultimately adopted. A comparison of these values and their effect on the transmission probabilities $|\boldsymbol{S}|$ for each L is shown in Fig. 5.18.

Fig. 5.19 is a plot of the elastic output from the SP calculation. At low energies and forward angles, the cross section due to Coulomb scattering is higher than found in the elastic data in Fig. 5.15. This discrepancy is likely due to the acceptance calculation's simplified trigger condition. Further work may be done to address this issue.

This elastic SP calculation does not include the option of including resonances. Thus, a separate R-matrix code is used. The SP calculation does, however, serve as a starting point reference for the potential scattering of the R-matrix calculations done in this work.

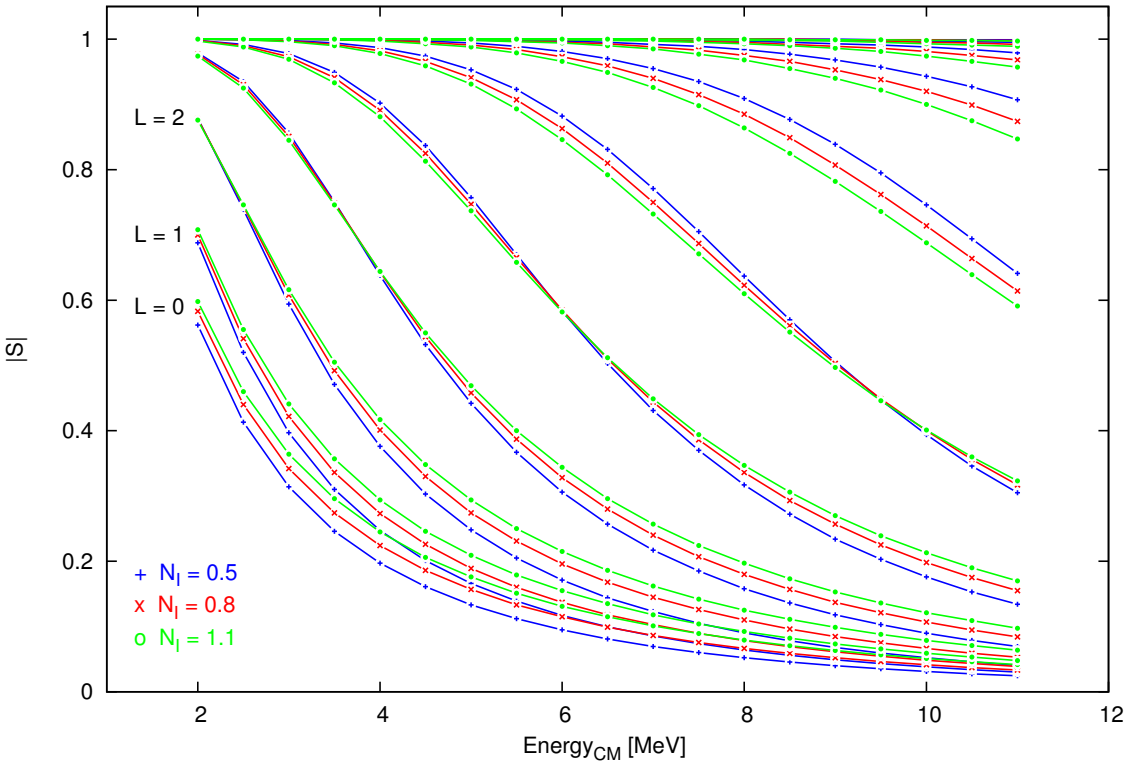

Figure 5.18: Comparison of the effect of different imaginary depths on the transmission probability $|\boldsymbol{S}|$ as a function of angular momentum L and center-of-mass energy for the SP calculation.

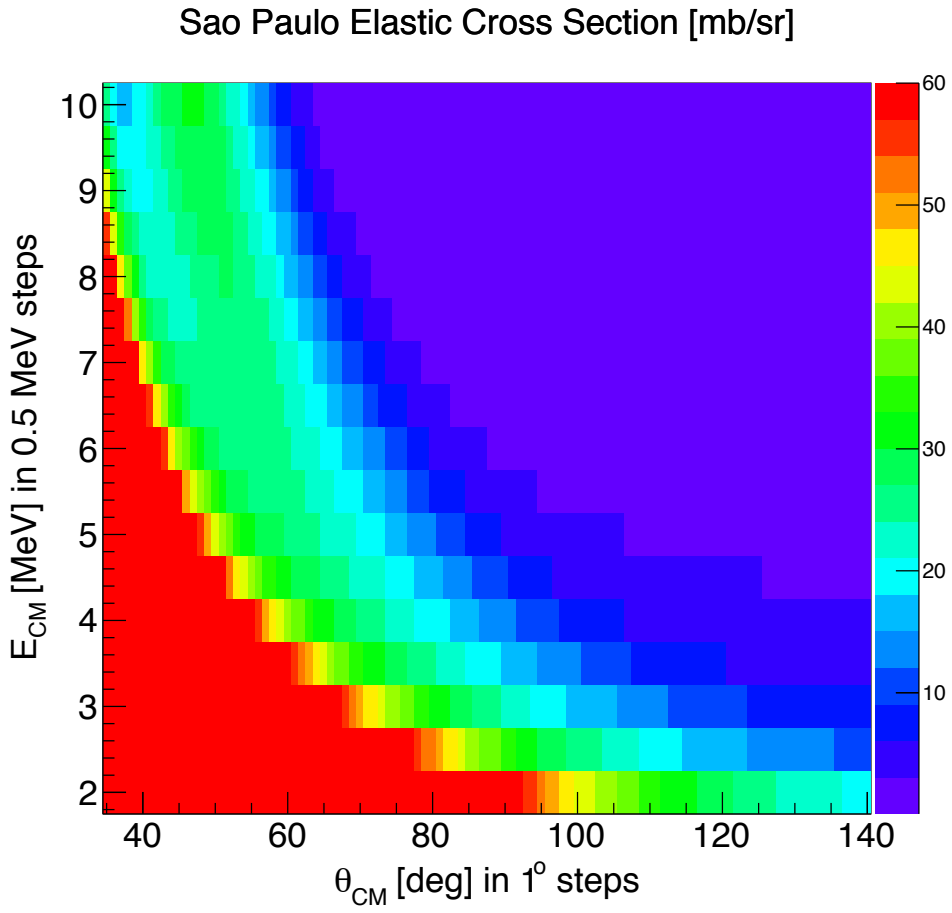

Figure 5.19: Elastic SP cross section calculation as a function of energy and angle, given in mb/sr. This output is used as a reference for the R-matrix calculation.

5.5.2 R-Matrix Calculations

In order to understand the resonances present in the data, interference effects among the resonances and potential scattering must be modeled. R-matrix theory can be used to calculate the cross sections of the resonances in the Breit-Wigner form shown in Eq. 1.27 by modeling the interaction during which the resonance is formed [5].

In R-matrix analysis, the cross sections for resonances are calculated through the use of a unitary and symmetric collision matrix **U**. Each matrix element of **U** defines the interaction between incoming channel c and outgoing channel c' as

$$U_{cc'} = \sqrt{U^0_{cc} U^0_{c'c'}} \left[\delta_{cc'} + \frac{i\sqrt{\Gamma_c(E)\Gamma_{c'}(E)}}{E_r - E - \frac{i}{2}\Gamma(E)} \right] \tag{5.20}$$

for potential scattering elements $\mathbf{U}^0$, channel orthogonality condition $\delta_{cc'} = \langle c|c' \rangle$, partial widths Γ_c and $\Gamma_{c'}$, resonance energy E_r, and total width $\Gamma(E) = \Gamma_c(E) + \Gamma_{c'}(E)$ for energy E [77]. The differential elastic cross section is then

$$\frac{d\sigma_{\text{el.}}}{d\Omega} = \frac{1}{(2I_1+1)(2I_2+1)} \sum_{M_1 M_2} \sum_{M_1' M_2'} \left| f_C(\Omega)\delta_{M_1' M_1}\delta_{M_2' M_2} + f^{(cM_1M_2)}_{cM_1'M_2'}(\Omega) \right|^2 \tag{5.21}$$

for Coulomb scattering amplitude f_C and elastic scattering amplitudes

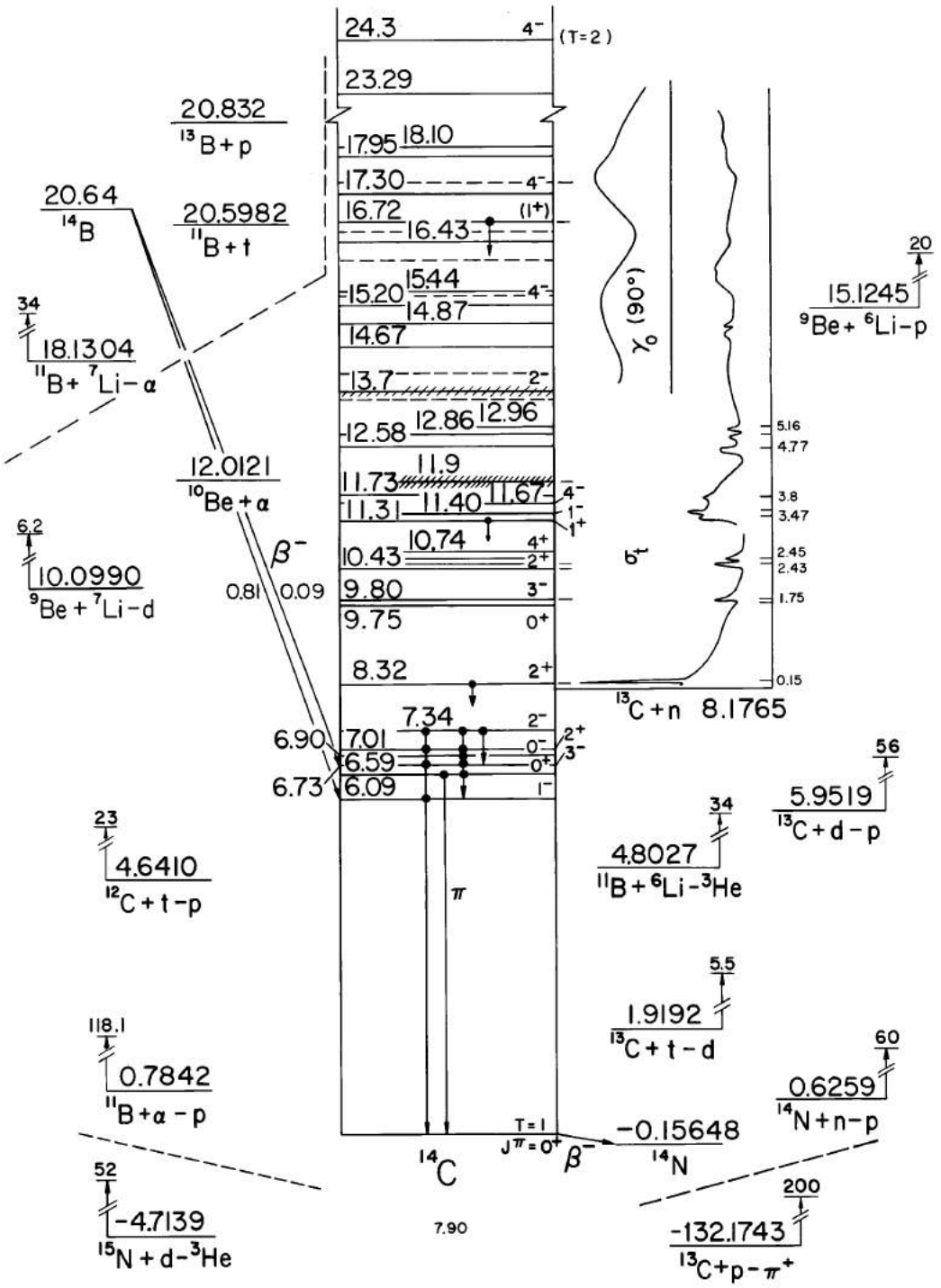

Figure 5.20: Level scheme of ^{14}C with various exit channels. Neutron separation occurs at 8.18 MeV, while $^{10}\mathrm{Be} + \alpha$ starts at 12.01 MeV. The energy domain studied in this work ranges from about 14 MeV to 22 MeV, over which the $^{13}\mathrm{C} + n$ cross section is low and flat. Thus, neutron emission can be modeled as background and absorbed with the optimal model used in DSigmaIV. Figure from [73].

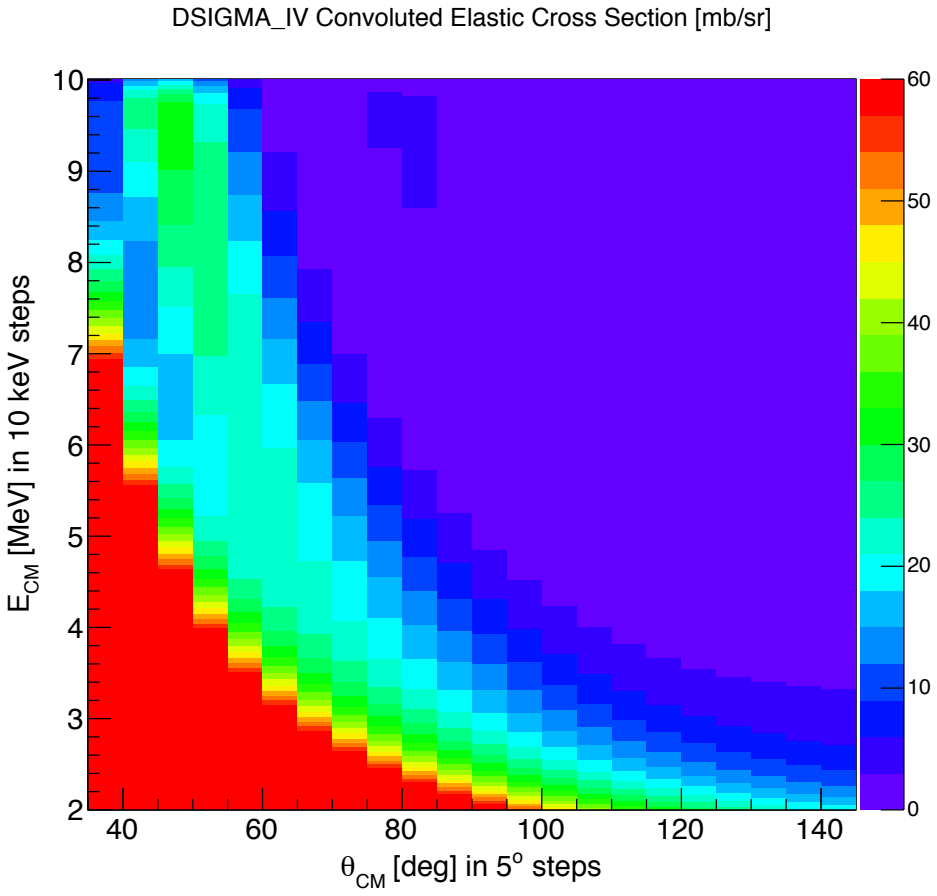

Figure 5.21: Elastic cross section calculation with DSIV using the Li and Hird parameter set, given in mb/sr. The results are similar to the SP calculation shown in Fig. 5.19.

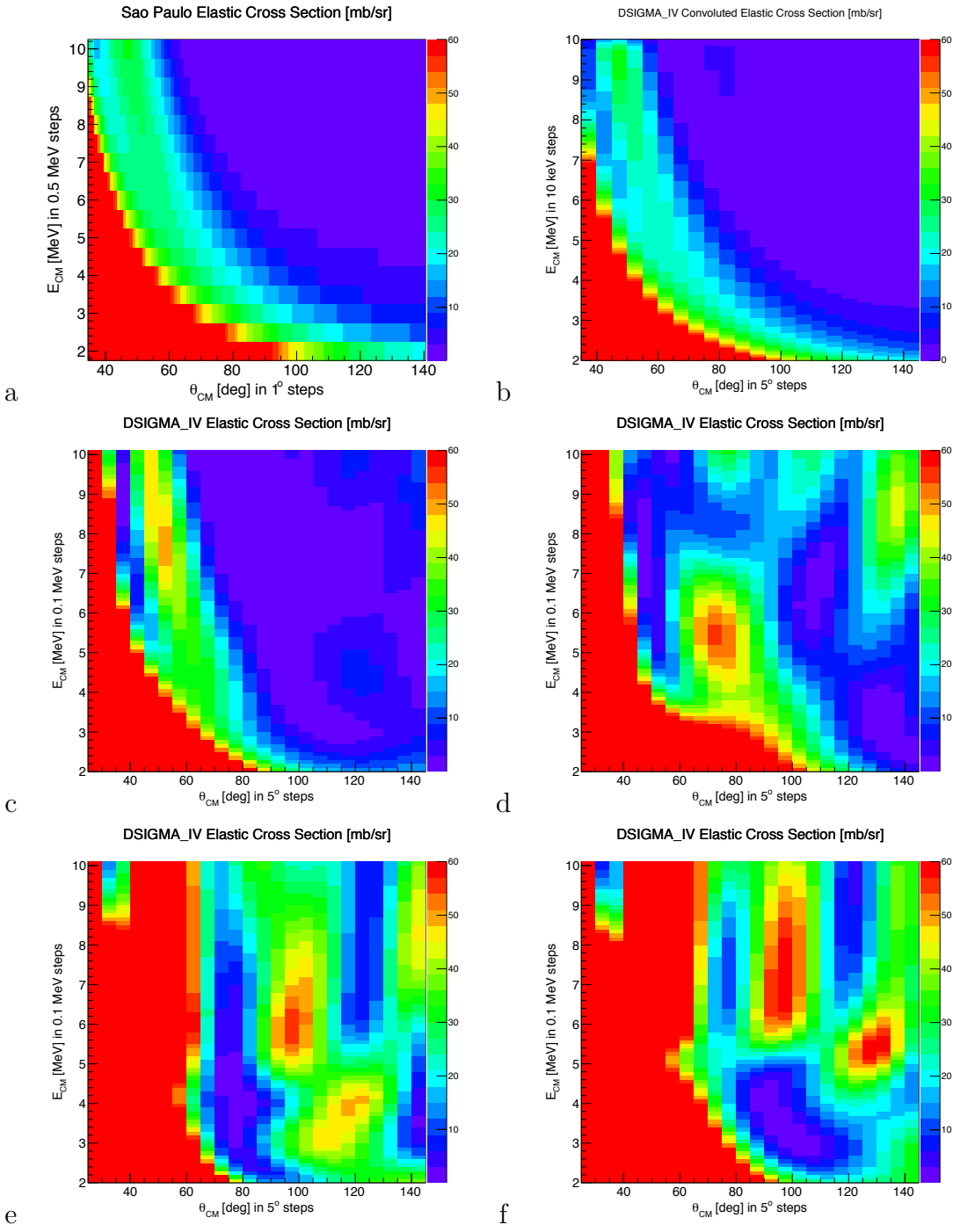

Figure 5.22: Comparison of various optical model parameter sets, given in mb/sr: (a) São Paulo from Fig. 5.19, (b) final choice from Fig. 5.21, (c) ^{10}Be+α, 6 MeV CM [74], (d) ^{10}B+α, 16.07 MeV CM [75], (e) ^{9}Be + α, 6.06 MeV CM set one [76], (f) ^{9}Be + α, 6.06 MeV CM set two [76].

$$f^{(cM_1M_2)}_{cM_1'M_2'}(\Omega) = i\frac{\sqrt{\pi}}{k}\sum_{J\pi}\sum_{I\ell}\sum_{I'\ell'}(2\ell+1)^{1/2}e^{i(\sigma_\ell+\sigma_{\ell'})}(I_1I_2M_1M_2|IM)$$
$$\times (I\ell M0|JM)(I_1'I_2'M_1'M_2'|I'M')(I'\ell'M'M-M'|JM)$$
$$\times (\delta_{c'c}\delta_{I'I}\delta_{\ell'\ell} - U^{J\pi}_{c'I'\ell',cI\ell})Y_{\ell'}^{M-M'}(\Omega). \tag{5.22}$$

The differential inelastic cross section is [77]

$$\frac{d\sigma_{c\to c'}}{d\Omega} = \frac{\pi}{k^2}\frac{1}{(2I_1+1)(2I_2+1)}\sum_L B_L(E)P_L(\cos\theta) \tag{5.23}$$

for

$$B_L(E) = \frac{1}{4\pi}\sum_{J\pi}\sum_{I\ell L}\sum_{J'\pi'}\sum_{I'\ell'L'}(-1)^{I-I'}e^{i(\sigma_\ell+\sigma_{\ell'}-\sigma_L-\sigma_{L'})}$$
$$\times Z(\ell JLJ', I\lambda)Z(\ell' JL'J', I'\lambda)U^{J\pi}_{c'I'\ell',cI\ell}(E)U^{J'\pi'*}_{c'I'L',cIL}(E), \tag{5.24}$$

where Z are the 6j-symbols, also called the Racah coefficients. The integrated inelastic cross section has the form

$$\sigma_{c\to c'} = \frac{\pi}{k^2}\frac{1}{(2I_1+1)(2I_2+1)}\sum_{J\pi}(2J+1)\sum_{I\ell}\sum_{I'\ell'}\left|U^{J\pi}_{c'I'\ell',cI\ell}(E)\right|^2, \tag{5.25}$$

explicitly showing the dependence of the cross section on the modulus squared of the collision matrix.

The partial width Γ_c from Eq. 1.29 now includes the spectroscopic factor SF as a scaling factor in the form

$$\Gamma_c(L,E) = 2P_c(L,E)\gamma_c^2(L)\mathrm{SF}. \tag{5.26}$$

Then, the calculated partial width Γ_{res} for a resonance is simply the partial width Γ_c times the transmission factor:

$$\Gamma_{\mathrm{res}} = \Gamma_c|U_{cc}^0|. \tag{5.27}$$

Previously when discussing the SP calculation, the transmission factor was denoted as $|\boldsymbol{S}|$. Now, it is explicitly given as $|U_{cc}^0|$ for this R-matrix calculation.

Elastic R-matrix calculations in this work were made with code provided by Wang Hongwei of the Shanghai Institute of Applied Physics (SINAP) at the Chinese Academy of Sciences, based on the Lane and Thomas [5] description of R-matrix theory. Reference calculations were made by my advisor Wolfgang Mittig of the National Superconducting Cyclotron Laboratory and Daisuke Suzuki of Institut de Physique Nucléaire Orsay with their own codes, based on the Lane and Thomas description and Descouvement and Baye description [77], respectively. Preliminary inelastic calculations were made with the code of Suzuki.

For a clear and complete description of R-matrix theory, see both the Lane and Thomas description [5] and the Descouvement and Baye description [77].

As input for Wang's R-matrix code, called DSigmaIV, resonances are entered for a given energy, spin, parity, and spectroscopic factor. A Coulomb radius parameter must also be given, and a choice between hard sphere scattering and an optical model parameterization is made. Ideally, the SP output would be used as input for DSigmaIV, but the SP output is not of the Woods-Saxon form required by DSigmaIV. Thus, various optical model parameter sets were considered and used to compute the non-resonant scattering in DSigmaIV. By design, the non-resonant scattering must represent exit channels other than ^{10}Be$+\alpha$, such as ^{13}C$+n$ by the absorption part of the optical model. The neutron separation energy is 8.18 MeV above the ^{14}C ground state, and resonances in ^{13}C$+n$ continue throughout the energy domain probed in $^{10}\mathrm{Be} + \alpha$. However, in the energy region of interest for this work in $^{10}\mathrm{Be} + \alpha$, the cross section in $^{13}\mathrm{C} + n$ is low and flat (Fig. 5.20), allowing for it to be modeled by the imaginary part of the optical model.

No reliable optical model parameter set exists for elastic scattering of ^{10}Be on ^{4}He, so sets describing similar reactions were considered, including $^{9}\mathrm{Be} + {}^{4}\mathrm{He}$ and $^{12}\mathrm{C} + {}^{4}\mathrm{He}$ at various energies.

An optical model parameter set from Li and Hird [78] best reproduced the SP output, and was thus adopted for this work. The Li and Hird set describes $^{9}\mathrm{Be} + {}^{4}\mathrm{He}$ at $E_\alpha = 48$ MeV. The parameters are given in Table 5.1, and are found in Ref. [78] in Table I(a). The DSigmaIV calculation with the Li and Hird parameter set without any resonances is shown in Fig. 5.21; comparisons to other optical model parameter sets that were considered are shown in Fig. 5.22.

Table 5.1: Optical model parameter set [78] used with DSigmaIV. The real and imaginary terms use the same radius and diffuseness, given in columns two and three, respectively. Column six shows the Coulomb radius r_c, and the last column displays the channel radius R_c, which was adopted as a different value than in Ref. [78].

V [MeV]	r [fm]	a [fm]	W_{vol} [MeV]	W_{sur} [MeV]	r_c [fm]	R_c [fm]
70.9	1.550	0.660	23.87	0	1.25	4.68

Table 5.1 also includes the channel radius R_c used in the DSigmaIV calculation. The value of R_c was varied to best fit the DSigmaIV output to the SP calculation. Variations between 3 and 5 fm were considered, as this range is common in literature [8, 78, 79]. A value of $R_c = 4.68$ fm was found to produce the best fit to SP. This corresponds to a Coulomb radius of $r_c = 1.25$ fm in the expression $R_c = r_c\left(A_1^{1/3} + A_2^{1/3}\right) = 3.74\ r_c$. Other optical model calculation sometimes use the expression $R_c = r_c\ A_1^{1/3} = 2.15\ r_c$ for defining channel radius.

With the optical model parameter set chosen, DSigmaIV was used to compute cross sections, shown in Fig. 5.23, comparable to that of the elastic data seen in Fig. 5.15. A side-by-side comparison of the two plots are given in Fig. 5.24. The DSigmaIV output shown in Fig. 5.23 is convoluted to the energy resolution of the data. The convolution assumes a Gaussian shape for the resonances, and incorporates both the uncertainty in beam energy and the uncertainty in the location of the reaction vertex. The convoluted cross section $\sigma_{\text{conv}}(E_i, \theta)$ for the i^{th} energy bin is defined in terms of the cross section $\sigma_{\text{DSIV}}(E, \theta)$ from the DSIV calculation as

$$\sigma_{\text{conv}}(E_i, \theta) = \sum_j \sigma_{\text{DSIV}}(E_j, \theta) \cdot w(i, j) \cdot N(i) \tag{5.28}$$

where $N(i)$ is a normalization factor and the Gaussian weight function is

$$w(i,j) = e^{\frac{-(E_i - E_j)^2}{2\Delta E^2}} \tag{5.29}$$

for

$$\Delta E = \sqrt{\left(\alpha \frac{\Delta R}{E}\right)^2 + \Delta E_b^2}\,. \tag{5.30}$$

In Eq. 5.30, $\Delta E_b = 143$ keV is the uncertainty in beam energy in center-of-mass, $\Delta R =$ 20 mm represents the uncertainty in the vertex position, and α is a constant relating the first term to the Betha formula. Values of ΔE are in the range of 200 to 350 keV.

Including energy convolution allows for the R-matrix calculation to be more reliably compared to the data. Since the angular resolution of the data is better than the 5° binning used in DSigmaIV, angular convolution is not necessary.

Since both ^{10}Be and ^{4}He are 0^+, the shapes of the resonances in the excitation functions are of the form of the square of the Legendre polynomial P_L for a given L value if potential scattering is neglected. Thus, in a first step the experimental angular distribution was compared to P_L^2 to provide a first guess of the angular momentum of the resonance. These initial comparisons ended up being qualitatively very similar to the output of DSigmaIV, which includes potential scattering. Thus, assigning spin and parity for each resonance was quite straightforward and not reliant on the optical model parameterization. Four examples

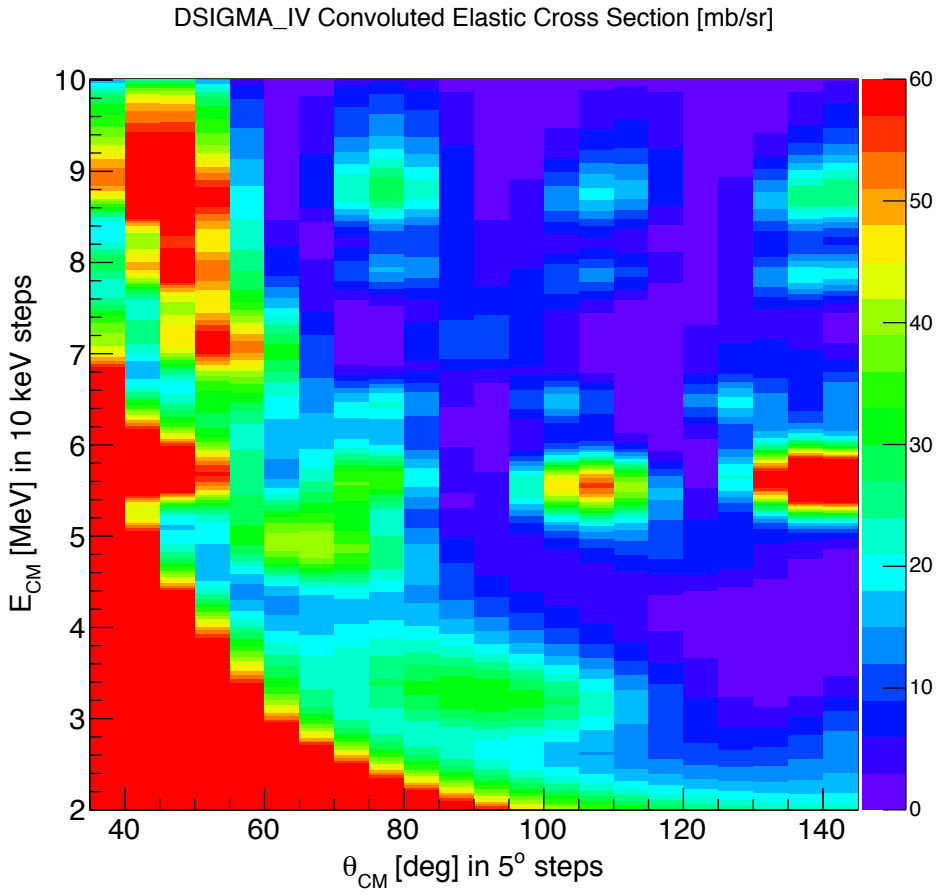

Figure 5.23: DSIV elastic cross section calculation, given in mb/sr, reproducing the elastic data in Fig. 5.15.

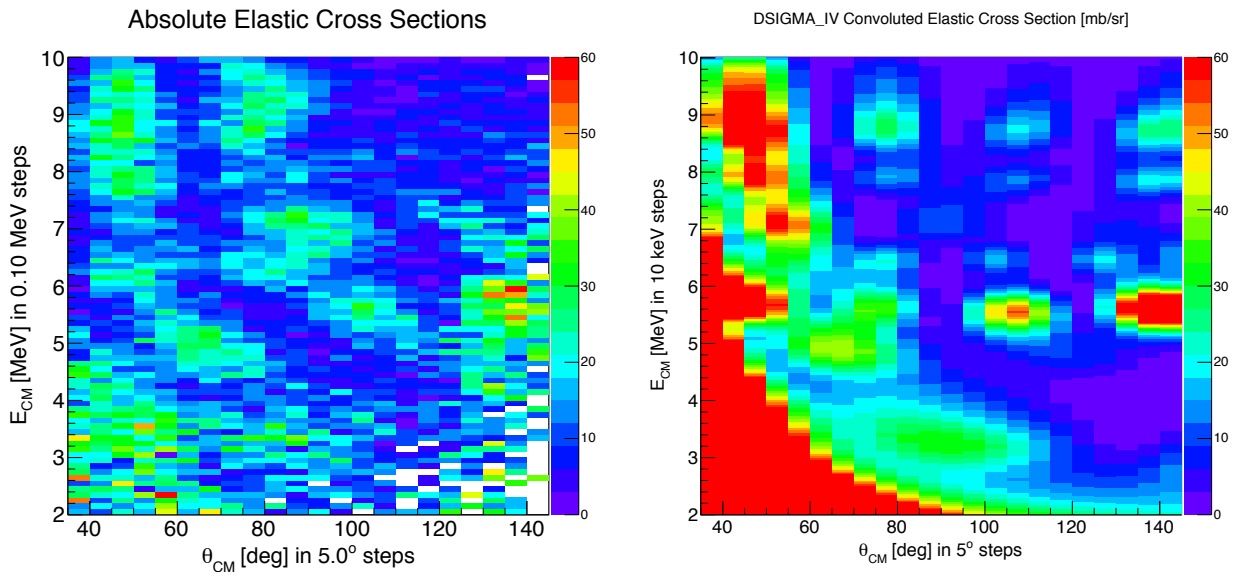

Figure 5.24: Side-by-side comparison of the data, given in mb/sr, from Fig. 5.15 (left) with the calculation from Fig. 5.23 (right).

are given in Fig. 5.25. Calculating the partial widths and spectroscopic factors and their associated uncertainties is described in the following section.

5.6 Resonance Spin and Parity Assignments

5.6.1 Method of Making Assignments

Since the experimental resonances follow quite perfectly the square of the Legendre polynomials, spin and parity assignments are easily made and unambiguous. Modeling the width and cross sections of the data by varying SF in DSigmaIV is the next step. Due to interference of the potential scattering with the resonances, perfect agreement cannot be expected between the calculation and experimental data. Many iterations of parameters of energy and spectroscopic factor were attempted, and the results in Table 5.2 and Fig. 5.23 represent the best current fit to data. The error are estimated from the variations of these parameters,

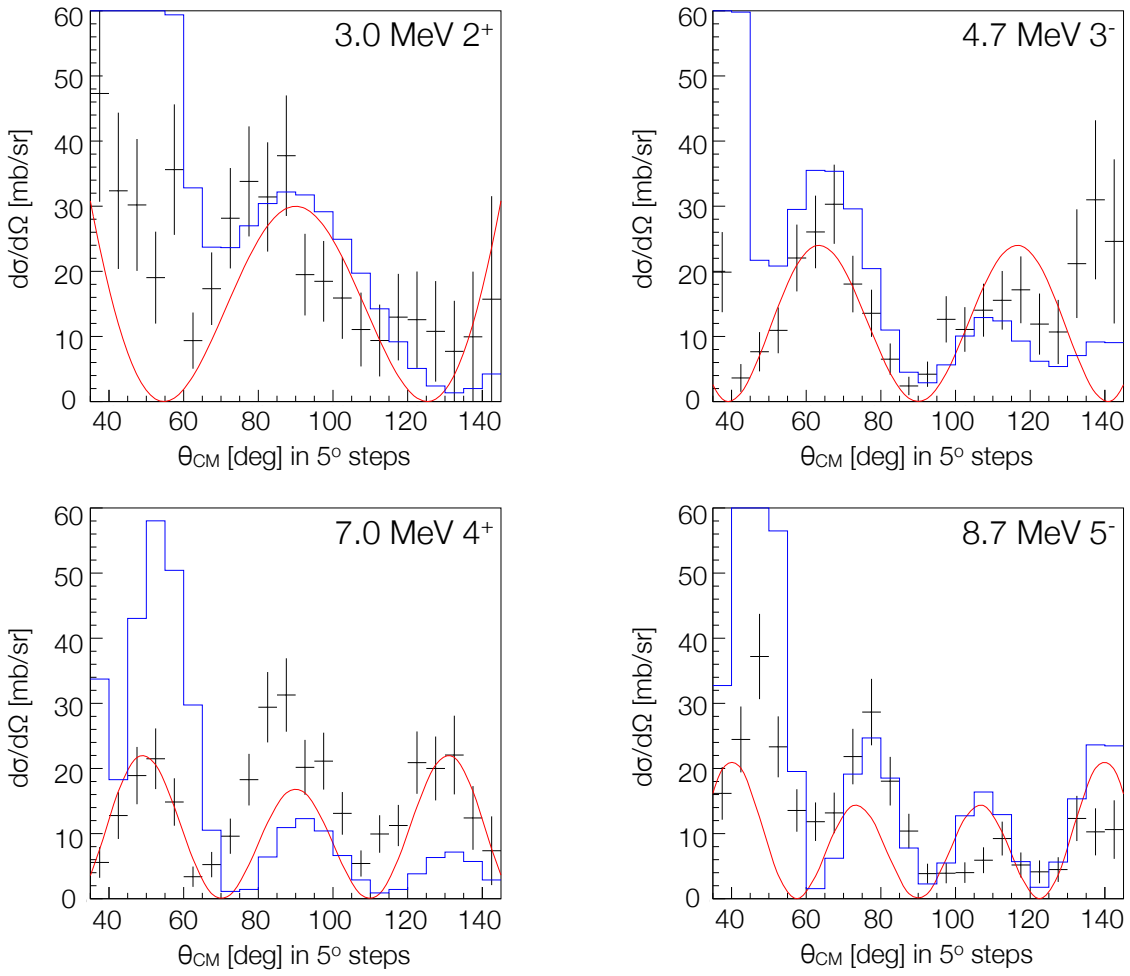

Figure 5.25: Angular cross sections for four elastic resonances seen in the data. The data are given in black, the squares of the Legendre polynomials are in red, and the DSigmaIV calculations are in blue. There is very good agreement in the oscillations of the angular distribution of the data with the red and blue curves. Of particular note in this figure, the good agreement of the data with the red P_L^2 curves show that the spin and parity assignments are not dependent on the optical model parameterization in DSigmaIV and are thus unambiguous.

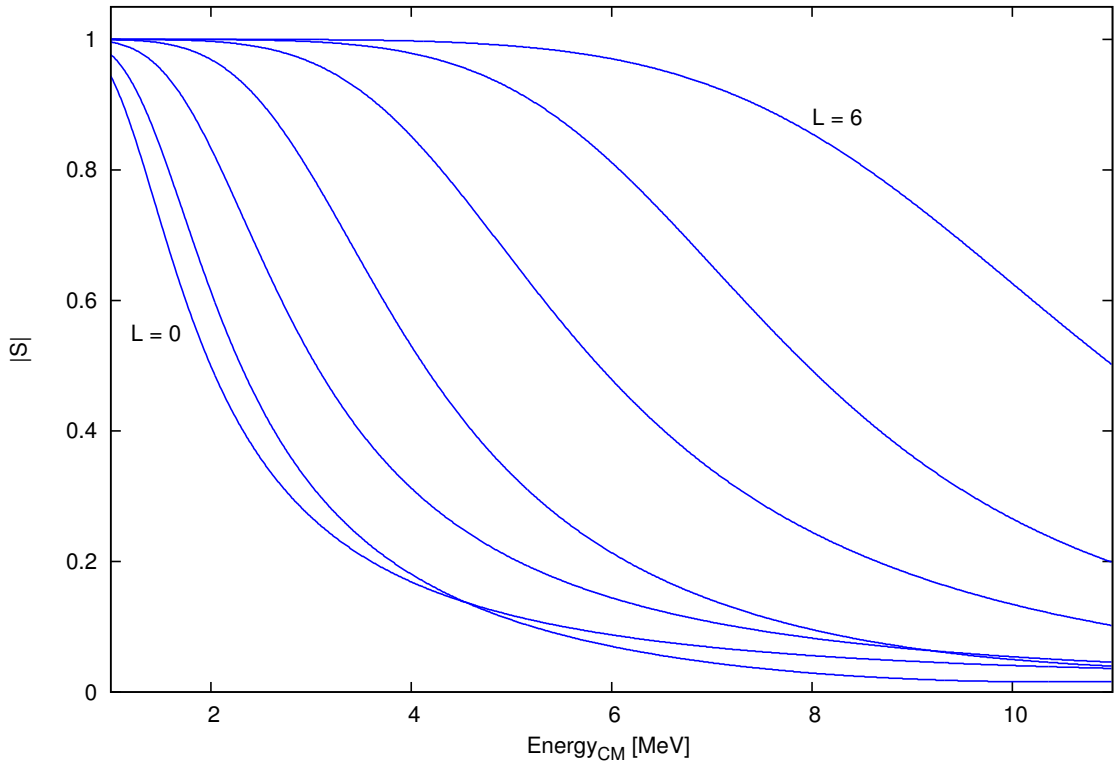

Figure 5.26: Plot of transmission probability $|\boldsymbol{S}| = |U^0_{cc}|$ as a function of angular momentum L and center-of-mass energy for the final elastic R-matrix calculation.

Table 5.2: Table of elastic scattering resonances, as obtained from the R-matrix calculation fit to the data. All of the spin-parity assignments are without ambiguity. The spectroscopic factors SF all are assigned a 50% uncertainty as they are not precisely calculated. $|U^0_{cc}|$ is the transmission factor for each resonance, as determined by the absorption chosen in the calculation. Γ_{res} is the width of the resonance, as defined in Eq. 5.27. Γ_{conv} is the width after convoluting the calculation with the energy resolution of around 150 keV.

E [MeV]	J^π	SF	$\lvert U^0_{cc}\rvert$	Γ_{res} [keV]	Γ_{conv} [MeV]
3.0 ± 0.15	2^+	0.3 ± 0.15	0.50	292	1.3 ± 0.5
4.7 ± 0.15	3^-	0.2 ± 0.1	0.40	273	1.1 ± 0.2
5.6 ± 0.15	5^-	0.4 ± 0.2	0.85	100	0.6 ± 0.2
6.5 ± 0.15	7^-	1.6 ± 0.8	0.95	22	0.6 ± 0.2
7.0 ± 0.15	4^+	0.2 ± 0.1	0.35	344	0.7 ± 0.3
7.9 ± 0.15	5^-	0.1 ± 0.05	0.50	104	0.5 ± 0.3
8.7 ± 0.15	5^-	0.4 ± 0.2	0.40	566	0.9 ± 0.3

within the limits of their agreement with the data. A plot of transmission factors is given in Fig. 5.26.

A short discussion is given for each resonance appearing in Table 5.2, after which evidence of rotational band structure is discussed.

5.6.2 3.0 MeV, 2^+

This resonance is the only 2^+ resonance identified in the analysis. The apparent partial width Γ_{conv} is difficult to precisely measure due to the low energy of the resonance near the strong potential scattering background, which means that Γ_{res} for this resonance is less precise than for the others. Interference effects result in the apparent energy to be 3.3 MeV.

5.6.3 4.7 MeV, 3^-

The apparent partial width Γ_{conv} is quite sharp for this resonance, resulting in confidence in the value of Γ_{res}. The forward-angle peak matches the data quite well, while there is slight

disagreement at back angles. The data have an increase in cross section near 135° that is not present in the calculation, though the calculation does reproduce the small increase near 115°. Interference effects result in the apparent energy to be 4.9 MeV.

5.6.4 5.6 MeV, 5^-

The calculation reproduces well each of the two backward-angle peaks in the data, both in width and cross section, though the peak near 75° is not clearly apparent.

5.6.5 6.5 MeV, 7^-

This is the highest L resonance assignment in this work. The peaks near 50° and especially 80° are well reproduced by a 7− assignment, which other spin-parity choices could not accomplish. With a narrow partial width of 22 keV, this resonance is very sensitive to changes in SF, energy, and interference.

5.6.6 7.0 MeV, 4^+

While the spin-parity assignment of this resonance is clear due to the location of the three peaks of the resonance in the data and calculation, the calculated width and SF are less precise. Interference puts the energy at 7.2 MeV. A substantial cross section in the inelastic data is found at this energy, implying a strong branching ratio to the 2^+ state in ^{10}Be, as predicted for a linear-chain state [80].

5.6.7 7.9 MeV, 5^-

The peak near 50° and 80° are reproduced in the calculation, as is a small peak near 140°. The resonance appears at 8.0 MeV due to interference. There is also a resonance at this energy in the inelastic data, implying a branching ratio to the 2^+ state in ^{10}Be.

5.6.8 8.7 MeV, 5^-

While the peaks near 50° and 80° are reproduced in the calculation, the calculation predicts larger cross sections at backward angles than is seen in the data. The resonance in the data at this energy may perhaps be two 5^- resonances, but they are not separable given the resolution of the data. Increasing the width of this 8.7 MeV calculation strongly increases the 140° peak, in disagreement with the data, so a relatively narrow width compared to the data is used. Interference puts the resonance at 8.8 MeV.

5.6.9 Experimental Results Compared to Theory: Positive-Parity Rotational Band

As mentioned previously in Chapter 3, Ref. [13] predicts a positive-parity rotational band for linear-chain structures in ^{14}C with $^{10}\text{Be}+\alpha$ correlations. The resonances in this band are 0^+, 2^+, and 4^+, as first shown in Fig. 3.5. A plot of this band in comparison to the 3.0 MeV 2^+ and 7.0 MeV 4^+ resonances from the DSigmaIV calculation is given in Fig. 5.27.

In Fig. 5.27, there is very good agreement between the experimental and theoretical 4^+ resonances. The 2^+ state differs by less than 1 MeV. The lack of a 0^+ resonance in the data does not rule out the assignment of these resonances to the linear-chain band, for two reasons: (1) with the substantial potential scattering background in the data at low energies,

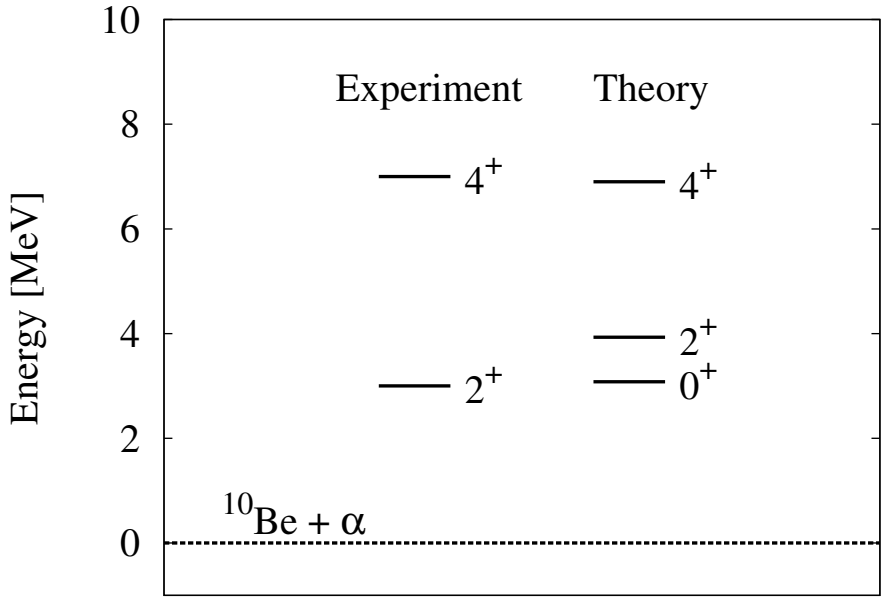

Figure 5.27: Comparison of resonances in this work (left column labeled "Experiment") with predictions for a rotational band with linear-chain structure [13] (right column labeled "Theory"), given in MeV above the $^{10}\mathrm{Be} + \alpha$ threshold. The theory predictions are in good agreement with the experimental results.

J^π of ^{14}C	(J', M') of ^{10}Be	Overlap
0^+	$(0, 0)$	28.9%
	$(2, 0)$	7.7%
2^+	$(0, 0)$	28.2%
	$(2, 2)$	0.3%
	$(2, 1)$	6.7%
	$(2, 0)$	10.1%

J^π of ^{14}C	(J', M') of ^{10}Be	Overlap
4^+	$(0, 0)$	15.7%
	$(2, 2)$	1.2%
	$(2, 1)$	14.0%
	$(2, 0)$	13.1%

Figure 5.28: Overlaps between linear-chainlike states and artificial $^{10}\mathrm{Be} + \alpha$ states. Tables from Ref. [80].

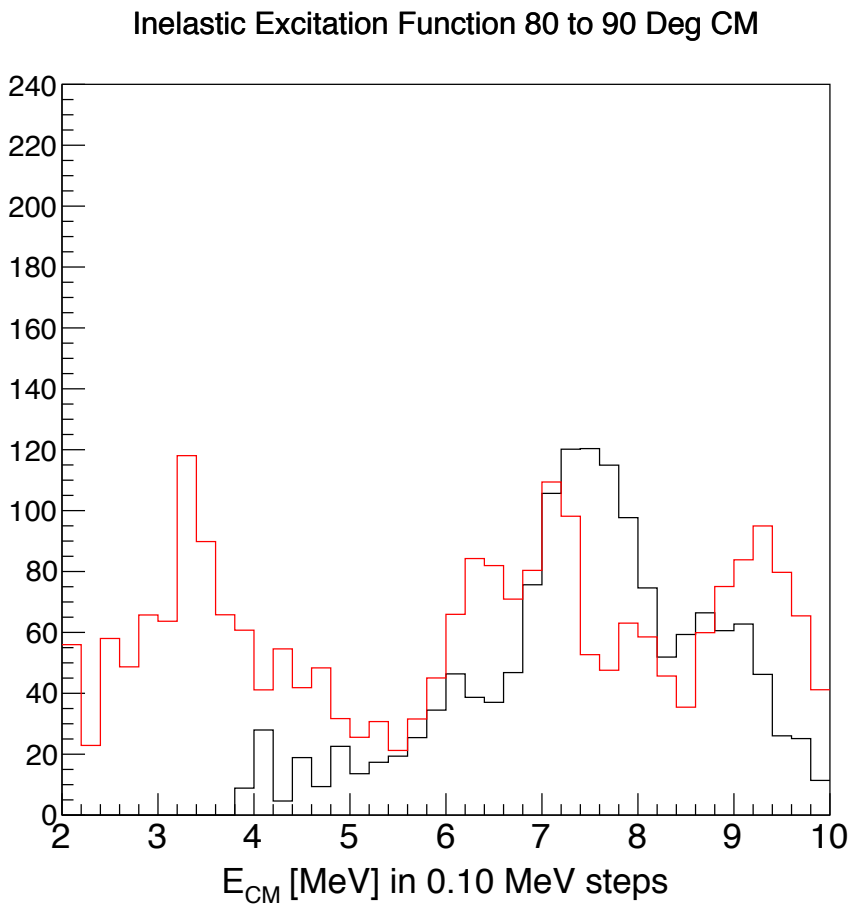

Figure 5.29: Experimental excitation functions, given in 4 × mb/sr, from this work: elastic in red, inelastic in black. Note the large cross section in inelastic at 7.2 MeV, which coincides with the 7.2 MeV elastic resonance (which is found to be a 7.0 MeV 4^+ resonance from the R-matrix calculation). This excitation function shows a strong branching to the inelastic for this 4^+ resonance, as predicted in Ref. [80] for the linear-chain rotational band.

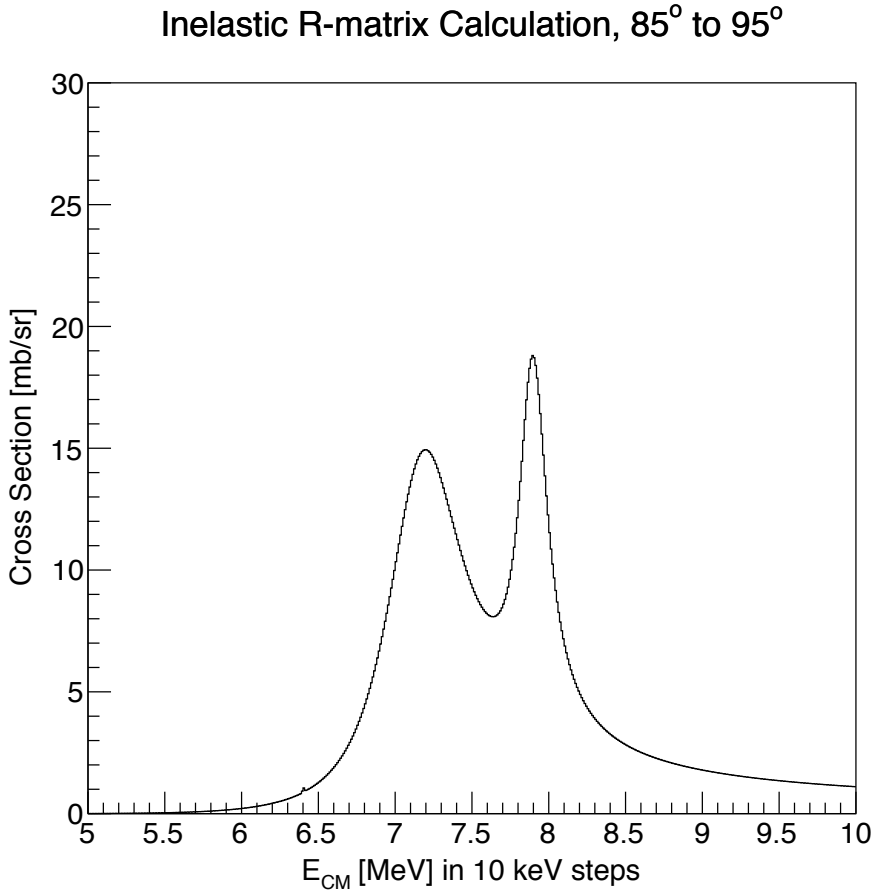

Figure 5.30: Preliminary inelastic R-matrix excitation function from 85° to 95°. The inelastic resonances in the calculation are 7.2 MeV 4^+ and 7.8 MeV 5^-. Further calculations will be made for the inelastic data.

the 0^+ resonance could be below the energy detection threshold, and (2) there is a strong absorption for $L = 0$ resonances. Thus this resonance will be much more difficult to see above background scattering.

The theory predicts overlap factors of 0.282 for the elastic 2^+ resonance and 0.157 for the elastic 4^+ resonance. From the elastic R-matrix calculation, values for spectroscopic factors of 0.3 ± 0.15 for the elastic 2^+ resonance and 0.2 ± 0.1 for the elastic 4^+ resonance were obtained, in very good agreement with theory. The predicted linear-chain band also has a large inelastic component [80], as shown in the tables of Fig. 5.28. Theory predicts an overlap factor of 0.283 for this inelastic channel. In the data, there is strong branching to the inelastic channel for the 4^+ resonance, as seen in Fig. 5.29 and the R-matrix calculation in Fig. 5.30. The current inelastic R-matrix calculations are preliminary. Even without a detailed analysis it is clear that the large cross section in the inelastic channel is compatible only with a large spectroscopic factor.

The good agreement between the predicted band and resonances shown in Fig. 5.27, along with the strong branching to the inelastic for the 4^+, make these resonances excellent candidates for a positive-parity linear-chain rotational band in ^{14}C.

5.6.10 Experimental Results Compared to Theory: Negative-Parity Rotational Band

With five negative-parity resonances in Table 5.2, various types of rotational band structure have been considered. As of yet, no final determination of band structure has been made. A few preliminary proposals are described below.

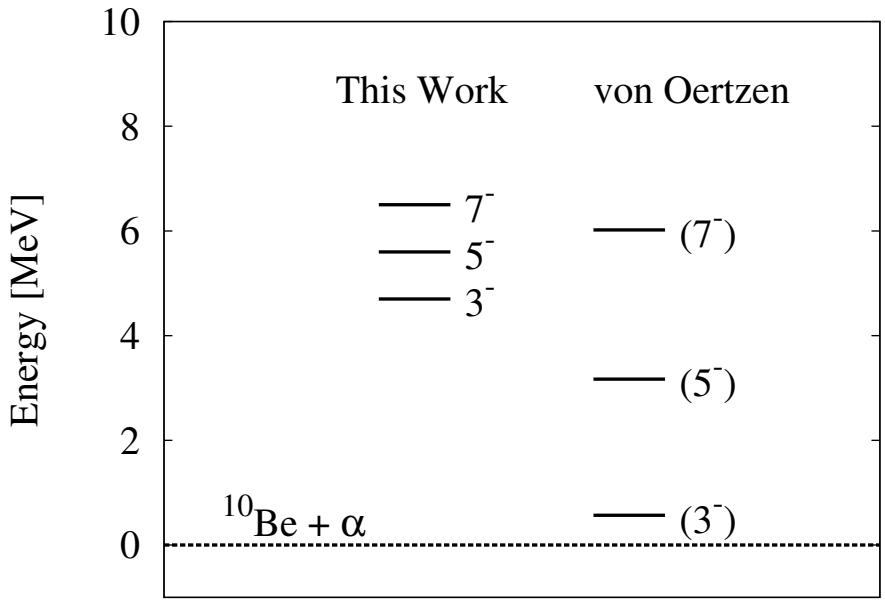

Figure 5.31: Comparison of negative-parity resonances of this work (left column) and from Ref. [25], observed via a (^{7}Li,d) reaction. The rotational band from Ref. [25] is predicted to be a prolate structure in ^{14}C. Poor agreement is seen for 3^- and 5^-, though it is better for 7^-.

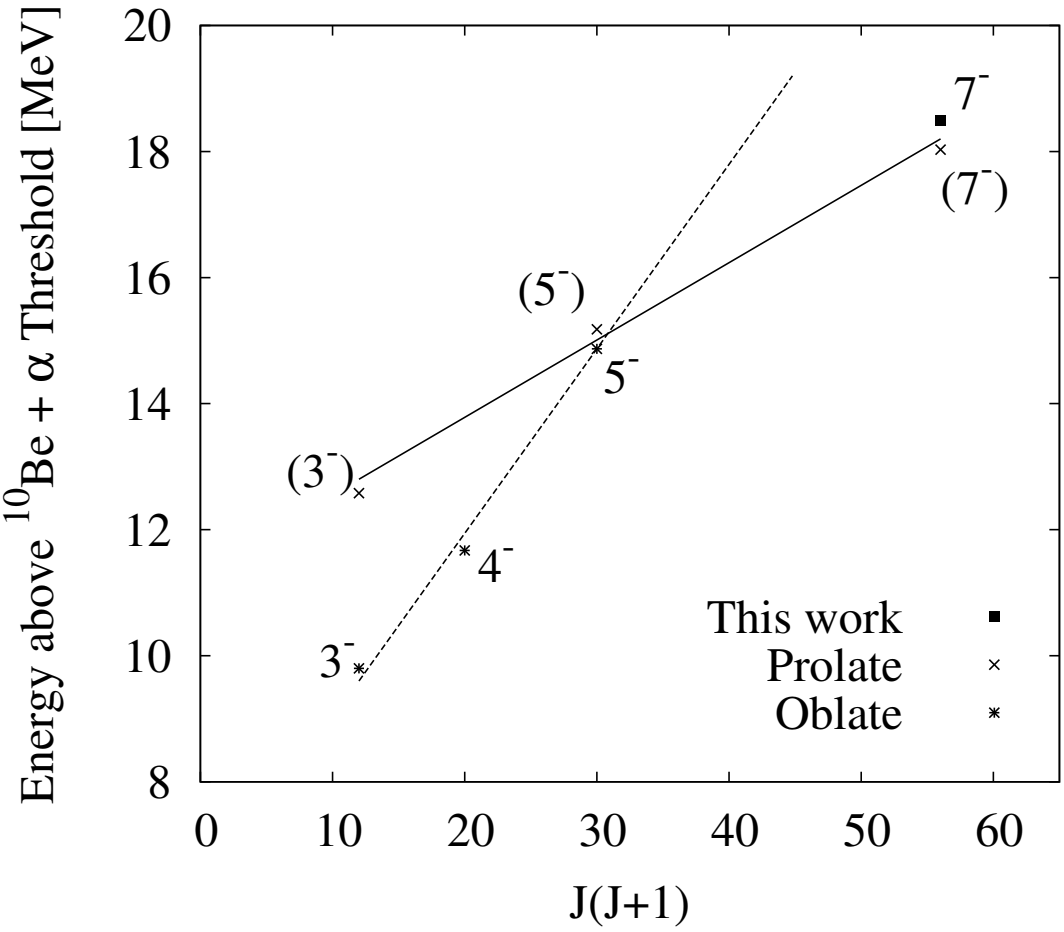

Figure 5.32: Band gradient comparison of 7^- resonance from this work with proposed prolate and oblate rotational bands in ^{14}C from Ref. [25]. Close agreement is seen with the prolate band.

- One possibility is that the 3^-, first 5^-, and 7^- resonances constitute a rotational band. These resonances are within 2 MeV of each other, resulting in a small band gradient of around 60 keV compared to the positive-parity band discussed above. Band gradient analysis allows for the comparison of different bands by moment of inertia, and is often shown by plotting energy as a function of $J(J+1)$. Other works [81, 82, 83, 84] do suggest sub-100 keV band gradients for α clustering, so further investigation of this

possible band structure is planned.

- A second consideration is prolate structure. Ref. [25] proposes a 3^-, 5^-, and 7^- prolate band in ^{14}C above the $^{10}\mathrm{Be} + \alpha$ threshold. A comparison of this band with the data is shown in Fig. 5.31. While the resonances do not generally agree in energy level spacing, the 7^- states are quite close in energy. The proposed band's 3^- and 5^- resonances are on the edge of the energy domain probed in this work, and are thus likely not to be seen in the data. One explanation for the discrepancy is that the 7^- seen in the data belongs to this proposed prolate band, and is not part of a band with the 3^- and 5^- resonances. Fig. 5.32 compares this 7^- resonance with predicted prolate and oblate band gradients from Ref. [25], showing much better agreement with the prolate band.

- Another view is that the 3^- resonance forms a band with one of the two higher 5^- resonances, as this would result in a more natural band gradient. Determining which 5^- resonance to pair with it may prove difficult; more work must be done on this possibility.

- One possible explanation is that the data do not show clear band structure of the negative-parity resonances. Ref. [13] predicts that while there is a positive-parity linear-chain rotational band, the negative-parity linear-chain band fractions into multiple negative-parity resonances. This interpretation is fully compatible with the data. In this case, it is natural to see multiple negative-parity states that have substantial α decay widths, but do not seem to constitute a distinctive rotational band.

5.6.11 Comparison to Literature

In Table 5.3, the resonances from this work in Table 5.2 are listed with observed resonances in ^{14}C from other reactions and works. The energies are given in MeV in ^{14}C, resulting in an increase of 12.01 MeV compared to Table 5.2. While some of the resonances from this work may be found at similar resonance energies, six have unique spin-parity assignment compared to literature while the 19.91(15) MeV resonance (7.9 MeV in Table 5.2) is assigned 5^-, as is the 19.76 MeV resonance from Ref. [85]. The selectivity of different reactions is not the same, and therefore exact correspondence is not expected. The results of this work provide the most reliable spin-parity assignments due to (1) the simple and well-understood reaction mechanism of resonant scattering and (2) clearly identified diffractive peak angles.

Table 5.3: Comparison of resonances from this work with literature. Reaction mechanism for each column is given under the reference. The last column show states which have been observed to α-decay. Table adapted from Ref. [85].

This Work $^{10}\mathrm{Be}+\alpha$		[85] $^{10}\mathrm{Be}+\alpha$		[86, 87] Various			[25] 2n Transfer		[88] $^{13}\mathrm{C}(p,n)$		[25] $^{9}\mathrm{Be}(^{7}\mathrm{Li},d)$		[89, 90, 91] α-decay	
E	J^π	E	J^π	E	J^π	Ref.	E	J^π	E	J^π	E	J^π	E	J^π
				11.666	4^-	[87]	11.66	4^-	11.7	4^-	11.66	4^-		
				11.73	5^-	[87]	11.73	4^+			11.73	4^+		
				11.9(3)	(1^-)	[86]								
				12.20	1^-	[86]								
				12.61	2^-	[86]					12.58	(3^-)		
				12.863		[87]					12.86			
				12.963	(3^-)	[87]	12.96(4)	3^-	12.96		12.96			
				(13.50)		[87]								
				13.7	2^-	[86]	13.7(1)		13.56					
							14.0(1)				14.03		14.3(1)	[91]
		14.54												
				14.63	(1^-)	[86]	14.67(5)	6^+			14.67	6^+		
				14.717	4^+	[86]								
				14.91	(1^+)	[86]	14.87(4)	5^-	14.87	5^-	14.87	5^-	14.8(1)	[89, 90, 91]
15.01(15)	2^+													
		15.11												
				15.20	4^-	[87]					15.18	(5^-)		
		15.35		(15.37)		[87]								
				15.44		[87]					15.40	(2^+)		
		15.51		15.56	3^-	[86]							15.55(10)	[89, 90]
				15.8	(1^-)	[86]	15.75(8)							
		15.91		15.91	4^+	[86]							15.9	[90]
				(16.02)		[87]								
		16.22												
				16.43		[87]	16.4(1)	(6^+)			16.43	6^+	16.43(10)	[89, 90, 91]
				(16.57)		[87]					16.53	(2^+)		
16.71(15)	3^-			16.715	(1^+)	[87]	16.72(5)	(6^+)			16.72	(1^+)		
				17.30	4^-	[87]			17.3	4^-	17.30	4^-	17.3(1)	[91]
		17.50	(3^-)	(17.5)	(1^+)	[87]	17.5(1)				17.52	(2^+)		
17.61(15)	5^-													
		17.98	(4^+)	17.95		[87]					17.91	(2^+)		
				18.10		[87]					18.03	(7^-)	(18.1)	[91]
18.51(15)	7^-								18.53	(4^-)	18.39		18.5(1)	[89, 90]
							18.6(1)	4^-			18.60		18.6(1)	[91]
		18.8												
		18.86	5^-											
19.01(15)	4^+										19.14		(19.07(1))	[89, 90, 91]
													(19.3(1))	[91]
		19.76	5^-				19.8(1)	2^+			19.73	(2^+)	19.83(1)	[89, 90, 91]
19.91(15)	5^-													
				20.4		[87]					20.02		(20.3(1))	[91]
20.71(15)	5^-	20.66	6^+								20.75		20.6(1)	[89, 91]
											21.00			
							21.4(2)				21.41		21.43(1)	[89, 90, 91]
				22.1		[87]	22.5(3)						22.45(3)	[89, 91]
							23.5		23.2				(23.15(1))	[89, 91]
				24.3		[87]							24.0(3)	[89]
				24.5		[87]								

Chapter 6

Conclusion

6.1 Summary

By studying elastic and inelastic scattering of 38.2 MeV ^{10}Be nuclei on a ^{4}He active target gas with the prototype AT-TPC, various resonances in ^{14}C were observed. The beam was delivered to the prototype AT-TPC by TwinSol at the University of Notre Dame. The Micromegas detector in the prototype AT-TPC employed individual pad biasing, and the geometry of the segmentation of the pads was optimized for triggering binary reactions. A 2^+ elastic scattering resonance at 3.0 MeV and a 4^+ elastic scattering resonance at 7.0 MeV are strong candidates for a predicted [13] linear-chain positive-parity rotational band in ^{14}C. Preliminary analysis performed on the inelastic data shows strong branching of the 7.0 MeV 4^+ resonance, also in agreement with the linear-chain prediction. These resonances provide the first strong experimental evidence of a linear-chain structure in ^{14}C. This evidence provides important information and insight into the more general discussion of α clustering in light nuclei. This result also strongly supports the reliability of the $\beta-\gamma$ constraint AMD for the clustering of carbon isotopes. Another important conclusion from the study by Suhara and Kanada-En'yo [13] is that the 0_3^+ state of ^{12}C has a linear-chain structure, which is not true in the molecular-orbit model [22]. Our results thus imply that this conjecture of ^{12}C by the AMD framework is very probable and merits further experimental investigation. This

possible state may be a one-dimensional gas-like state, a novel nuclear structure proposed by another work of Suhara [11], and this work points to a new horizon for cluster studies.

Negative-parity elastic resonances have also been investigated for possible band structure. Preliminary analysis shows that a 6.5 MeV 7^- elastic resonance may be part of a suggested [25] prolate rotational band. The resonance may instead form a rotational band with the observed 4.7 MeV 3^- and 5.6 MeV 5^- elastic resonances. There are also two additional 5^- elastic resonances observed at 7.9 and 8.7 MeV, with the former possibly having branching to the inelastic. The general features of the negative-parity states are compatible with the mixing of many configurations of rotational-like band structure.

This work has demonstrated the effectiveness of the principles of the AT-TPC. A He:CO_2 90:10 active target gas successfully allowed for the measurement of resonances in ^{14}C across an energy domain of nearly 40 MeV in the lab frame, about 10 MeV in the center-of-mass frame. The TPC capabilities provided large angular coverage for the measurements, with probed center-of-mass angles ranging from 35 to 145°. This work employed the first demonstrated use of the Micromegas amplification device's gain variation for specific pads, which was essential for triggering the reactions in the prototype AT-TPC. Along with other experimental work performed with the prototype AT-TPC [9, 26, 27], this work has provided important information for the design and construction of the now-built full-scale AT-TPC.

6.2 Outlook

The prototype AT-TPC will be of continued use as a complimentary device to the full-scale AT-TPC. Its smaller size makes it portable for work at other labs, providing the opportunity for studies with a large variety of beams.

While spin-parity assignments have been made for the seven of the observed elastic resonances in ^{14}C, the values of their partial widths and spectroscopic factors could be determined with better precision if needed. Further analysis will be done for the inelastic data, including performing detailed R-matrix calculations similar to those made for the elastic data. In addition to the strong evidence of linear-chain structure in a predicted positive-parity rotational band, other band structures will be further investigated among the observed elastic and inelastic resonances.

Many other light systems show specific quasi-molecular structures. A proposed experiment for $^{8}\mathrm{He} + \alpha$ scattering has been accepted for beam time at TRIUMF-ISAC, and will be performed in the near future.

BIBLIOGRAPHY

BIBLIOGRAPHY

[1] I. J. Thompson and F. N. Nunes. *Nuclear Reactions for Astrophysics*. Cambridge University Press, 2009.

[2] D. T. Khoa, D. C. Cuong, and Y. Kanada-En'yo. Hindrance of the excitation of the Hoyle state and the ghost of the 2_2^+ state in ^{12}C. *Phys. Lett. B*, **695**:469, 2011.

[3] J. W. Bittner and R. D. Moffat. Elastic Scattering of Alpha Particles by Carbon. *Phys. Rev.*, **96**:374, 1954.

[4] J. M. Blatt and V. F. Weisskopf. *Theoretical Nuclear Physics*. Dover, 1991. Originally published by Springer-Verlag in 1979.

[5] A. M. Lane and R. G. Thomas. R-Matrix Theory of Nuclear Reactions. *Rev. Mod. Phys.*, **30**:257, 1958.

[6] S. S. M. Wong. *Introductory Nuclear Physics*. Wiley-Interscience, 2nd edition, 1998.

[7] J. A. Wheeler. Molecular Viewpoints in Nuclear Structure. *Phys. Rev.*, **52**:1083, 1937.

[8] H. Yamaguchi, D. Kahl, Y. Wakabayashi, S. Kubono, T. Hashimoto, S. Hayakawa, T. Kawabata, N. Iwasa, T. Teranishi, Y. K. Kwon, D. N. Binh, L. H. Khiem, and N. N. Duy. α-resonance structure in ^{11}C studied via resonant scattering of $^7\mathrm{Be} + \alpha$ and with the $^7\mathrm{Be}(\alpha, p)$ reaction. *Phys. Rev. C*, **87**:034303, 2013.

[9] D. Suzuki, A. Shore, W. Mittig, J. J. Kolata, D. Bazin, M. Ford, T. Ahn, F. D. Becchetti, S. Beceiro Novo, D. Ben Ali, B. Bucher, J. Browne, X. Fang, M. Febbraro, A. Fritsch, E. Galyaev, A. M. Howard, N. Keeley, W. G. Lynch, M. Ojaruega, A. L. Roberts, and X. D. Tang. Resonant α scattering of ^{6}He: Limits of clustering in ^{10}Be. *Phys. Rev. C*, **87**:054301, 2013.

[10] H. Feldmeier and T. Neff. Clusters, Halos, and S-Factors in Fermionic Molecular Dynamics. *EPJ Web of Conferences*, **63**:02021, 2013.

[11] T. Suhara, Y. Funaki, B. Zhou, H. Horiuchi, and A. Tohsaki. One-Dimensional α Condensation of α-Linear-Chain States in ^{12}C and ^{16}O. *Phys. Rev. Lett.*, **112**:062501, 2014.

[12] W. Broniowski and E. R. Arriola. Signatures of α Clustering in Light Nuclei from Relativistic Nuclear Collisions. *Phys. Rev. Lett.*, **112**:112501, 2014.

[13] T. Suhara and Y. Kanada-En'yo. Cluster structures of excited states in ^{14}C. *Phys. Rev. C*, **82**:044301, 2010.

[14] H. Feldmeier. Fermionic Molecular Dynamics. *Nucl. Phys. A*, **515**:147, 1990.

[15] H. Horiuchi. Microscopic Study of Clustering Phenomena in Nuclei. *Nucl. Phys. A*, **522**:257, 1991.

[16] P. Descouvemont and D. Baye. Microscopic theory of the $^{8}\mathrm{Be}(\alpha,\gamma)^{12}\mathrm{C}$ reaction in a three-cluster model. *Phys. Rev. C*, **36**:54, 1986.

[17] H. Morinaga. Interpretation of Some of the Excited States of $4n$ Self-Conjugate Nuclei. *Phys. Rev.*, **101**:254, 1956.

[18] A. H. Wuosmaa, R. R. Betts, B.B. Back, M. Freer, B. G. Glagola, Th. Happ, D. J. Henderson, and P. Wilt. Evidence for Alpha-Particle Chain Configurations in ^{24}Mg. *Phys. Rev. Lett.*, **68**:1295, 1992.

[19] F. Hoyle. On Nuclear Reactions Occurring in Very Hot Stars. 1. The Synthesis of Elements from Carbon to Nickel. *Astrophys. J. Suppl. Ser.*, **1**:121, 1954.

[20] C. W. Cook, W. A. Fowler, C. C. Lauritsen, and T. Lauritsen. B^{12}, C^{12}, and the Red Giants. *Phys. Rev.*, **107**:508, 1957.

[21] M. Freer, H. Fujita, Z. Buthelezi, J. Carter, R. W. Fearick, S. V. Förtsch, R. Neveling, S. M. Perez, P. Papka, F. D. Smit, J. A. Swartz, and I. Usman. 2^+ excitation of the ^{12}C Hoyle state. *Phys. Rev. C*, **80**:041303, 2009.

[22] N. Itagaki, T. Otsuka, K. Ikeda, and S. Okabe. Equilateral-Triangular Shape in ^{14}C. *Phys. Rev. Lett.*, **92**:142501, 2004.

[23] T. Suhara and Y. Kanada-En'yo. Quadrupole Deformation β and γ Constraint in a Framework of Antisymmetrized Molecular Dynamics. *Prog. Theor. Phys.*, **123**:303, 2010.

[24] N. Itagaki, S. Okabe, K. Ikeda, and I. Tanihata. Molecular-orbital structure in neutron-rich C isotopes. *Phys. Rev. C*, **64**:014301, 2001.

[25] W. von Oertzen, H. Bohlen, M. Milin, Tz. Kokalova, S. Thummerer, A. Tumino, R. Kalpakchieva, T. N. Massey, Y. Eisermann, G. Graw, T. Faestermann, R. Hertenberger, and H.-F. Wirth. Search for cluster structure of excited states in ^{14}C. *Eur. Phys. J. A*, **21**:193, 2004.

[26] D. Suzuki, D. Bazin, W. Mittig, W. G. Lynch, C. Hewko, A. Roux, D. Ben Ali, J. Browne, E. Galyaev, M. Ford, A. Fritsch, J. Gilbert, F. Montes, A. Shore, G. Westfall, and J. Yurkon. Test of a micromegas detector with helium-based gas mixtures for active target time projection chambers utilizing radioactive isotope beams. *Nucl. Instr. and Meth. Phys. Res. A*, **660**:64, 2011.

[27] D. Suzuki, M. Ford, D. Bazin, W. Mittig, W. G. Lynch, T. Ahn, S. Aune, E. Galyaev, A. Fritsch, J. Gilbert, F. Montes, A. Shore, J. Yurkon, J. J. Kolata, J. Browne, A. Howard, A. L. Roberts, and X. D. Tang. Prototype AT-TPC: Toward a new generation active target time projection chamber for radioactive beam experiments. *Nucl. Instr. and Meth. Phys. Res. A*, **691**:39, 2012.

[28] H. Sakurai. Physics opportunities with the RI Beam Factory at RIKEN. *Eur. Phys. J. Special Topics*, **150**:249, 2007.

[29] R. York. Realization of FRIB at Michigan State University. *APS April Meeting 2010*, 2010.

[30] D. Leitner, J. Popielarski, A. Lapierre, F. Montes, G. Perdikakis, S. Schwarz, W. Wittmer, and X. Wu. Status of the ReAccelerator Facility ReA for Rare Isotopes. *2011 Fall Meeting of the APS Division of Nuclear Physics*, 2011.

[31] S. Gales. SPIRAL2 at GANIL: A world leading ISOL facility at the dawn of the next decade. *Progress in Particle and Nuclear Physics*, **59**:22, 2007.

[32] E. Pollacco, S. Anvar, H. Baba, P. Baron, D. Bazin, C. Belkhiria, B. Blank, J. Chavas, P. Chomaz, E. Delagnes, F. Druillole, P. Hellmuth, C. Huss, E. Galyaev, B. Lynch, W. Mittig, T. Murakami, L. Nalpas, J. Pedroza, R. Raabe, J. Pibernat, B. Raine, A. Rebii, A. Taketani anf F. Saillant, D. Suzuki, N. Usher, and G. Wittwer. GET: A Generic Electronic System for TPCs for nuclear physics experiments. *Physics Procedia*, **37**:1799, 2012.

[33] Y. Giomataris, Ph. Rebourgeard, J. P. Robert, and G. Charpak. MICROMEGAS: a high-granularity position-sensitive gaseous detector for high particle-flux environments. *Nucl. Instr. and Meth. Phys. Res. A*, **376**:29, 1996.

[34] C. E. Demonchy, M. Caamaño, H. Wang, W. Mittig, P. Roussel-Chomaz, H. Savajols, M. Chartier, D. Cortina-Gil, A. Fomichev, G. Frémont, P. Gangnant, A. Gillibert, L. Giot, M. S. Golovkov, B. Jurado, J. F. Libin, A. Obertelli, E. Pollaco, A. Rodin, Ch. Spitaels, S. Stepantsov, G. Ter-Akopian, and R. Wolski. MAYA: An active-target detector for binary reactions with exotic beams. *Nucl. Instr. and Meth. Phys. Res. A*, **583**:341, 2007.

[35] Y. Mizoi, T. Fukuda, Y. Matsuyama, T. Miyachi, J. Nakano, N. Fukuda, M. Hirai, H. Kobinata, Y. X. Watanabe, H. Sakurai, Y. Watanabe, and A. Yoshida. Multiple-sampling and tracking proportional chamber for nuclear reactions with low-energy radioactive isotope beams. *Nucl. Instr. and Meth. Phys. Res. A*, **431**:112, 2010.

[36] K. Yamaguchi, H. Ishiyama, M. H. Tanaka, Y. X. Watanabe, H. Miyatake, Y. Hirayama, N. Imai, H. Makii, Y. Fuchi, S. C. Jeong, T. Nomura, Y. Mizoi, S. K. Das, T. Fukuda, T. Hashimoto, and I. Arai. Development of the GEM-MSTPC for measurements of low-energy nuclear reactions. *Nucl. Instr. and Meth. Phys. Res. A*, **623**:135, 2010.

[37] D. R. Nygren. The Time-Projection Chamber - A new 4π detector for charged particles. *Proceedings of the 1974 PEP Summer Study, PEP-144*, page 58, 1974.

[38] D. R. Nygren. The Time-Projection Chamber. *Proceedings of the 1975 PEP Summer Study, PEP-198*, page 126, 1975.

[39] D. Fancher, H. J. Hilke, S. Loken, P. Martin, J. N. Marx, D. R. Nygren, P. Robrish, G. Shapiro, M. Urban, and W. Wenzel. Performance of a Time-Projection Chamber. *Nucl. Instr. and Meth.*, **161**:383, 1979.

[40] S. Benso and L. Rossi. A Time Projection Chamber for Precise Vertex Determination. *Nucl. Instr. and Meth.*, **187**:355, 1981.

[41] G. F. Knoll. *Radiation Detection and Measurement*. Wiley, 4th edition, 2010.

[42] F. Sauli. GEM: A new concept for electron amplification in gas detectors. *Nucl. Instr. and Meth. Phys. Res. A*, **386**:531, 1997.

[43] T. Suhara and Y. Kanada-En'yo. Cluster structures of excited states in ^{14}C. *Journal of Physics: Conference Series*, **321**:012047, 2012.

[44] A. Ono, H. Horiuchi, T. Maruyama, and A. Ohnishi. Antisymmetrized Version of Molecular Dynamics with Two-Nucleon Collisions and Its Application to Heavy Ion Reactions. *Prog. Theor. Phys.*, **87**:1185, 1992.

[45] K. Varga, Y. Suzuki, and R. G. Lovas. Microscopic multicluster description of neutron-halo nuclei with a stochastic variational method. *Nucl. Phys. A*, **571**:447, 1994.

[46] Y. Ogawa, K. Arai, Y. Suzuki, and K. Varga. Microscopic four-cluster description of ^{10}Be and ^{10}C with the stochastic variational method. *Nucl. Phys. A*, **673**:122, 2000.

[47] J. Aichelin and H. Stöcker. Quantum Molecular Dynamics - A Novel Approach to N-Body Correlations in Heavy Ion Collisions. *Phys. Lett. B*, **176**:14, 1986.

[48] A. Ohnishi, T. Maruyama, and H. Horiuchi. Near- and Far-Side Contributions to Ejectile Polarization. *Prog. Theor. Phys.*, **87**:417, 1992.

[49] C. Hartnack, L. Zhuxia, L. Neise, G. Peilert, A. Rosenhauer, H. Sorge, J. Aichelin, H. Stöcker, and W. Greiner. Quantum Molecular Dynamics: A Microscopic Model from UNILAC to CERN Energies. *Nucl. Phys. A*, **495**:303, 1989.

[50] P. Kramer and M. Saraceno. Geometry of the Time-Dependent Variational Principle in Quantum Mechanics. *Lecture Notes in Physics*, **140**:41, 1981.

[51] A. B. Volkov. Equilibrium Deformation Calculations of the Ground State Energies of the 1p Shell Nuclei. *Nucl. Phys.*, **74**:33, 1965.

[52] N. Yamaguchi, T. Kasahara, S. Nagata, and Y. Akaishi. Effective Interaction with Three-Body Effects. *Prog. Theor. Phys.*, **62**:1018, 1979.

[53] S. Okabe and Y. Abe. The Structure of ^{9}Be by a Molecular Model. II. *Prog. Theor. Phys.*, **61**:1049, 1979.

[54] N. Itagaki and S. Okabe. Molecular Orbital Structures in ^{10}Be. *Phys. Rev. C*, **61**:044306, 2000.

[55] F.D. Becchetti, M.Y. Lee, T.W. O'Donnell, D.A. Roberts, J.J. Kolata, L.O. Lamm, G. Rogachev, V. Guimarães, P.A. DeYoung, and S. Vincent. The TwinSol low-enegy radioactive nuclear beam apparatus: status and recent results. *Nucl. Instr. and Meth. Phys. Res. A*, **505**:377, 2003.

[56] University of Notre Dame. http://library.nd.edu/chemistry/about/history/physics.shtml.

[57] ISNAP: MC-Snics Sputter Ion Source. http://isnap.nd.edu/html/research_SNICS.html.

[58] ISNAP: FN Tandem Van de Graaff Accelerator. http://isnap.nd.edu/html/research_FN.html.

[59] ISNAP: Radioactive Nuclear Beams (RNB). https://isnap.nd.edu/html/research_radio.html.

[60] W. M. Haynes, editor. *CRC Handbook of Chemistry & Physics*. CRC Press, 92nd edition, 1991.

[61] R. Veenhof. Garfield, recent developments. *Nucl. Instr. and Meth. Phys. Res. A*, **419**:726, 1998.

[62] S. F. Biagi. Magbolts – transport of electrons in gas mixtures. http://magboltz.web.cern.ch/magboltz/.

[63] M. Anderson, F. Bieser, R. Bossingham, D. Cebra, E.L. Hjort, S.R. Klein, S. Kleinfelder, C.Q. Vu, and H. Wieman. A readout system for the STAR time projection chamber. *Nucl. Instr. and Meth. Phys. Res. A*, **499**:679, 2003.

[64] I. Giomataris, R. De Oliveria, S. Andriamonje, S. Aune, G. Charpak, P. Colas, G. Fanourakis, E. Ferrer, A. Giganon, Ph. Rebourgeard, and P. Salin. Micromegas in a Bulk. *Nucl. Instr. and Meth. Phys. Res. A*, **560**:405, 2006.

[65] P. Baron, D. Calvet, E. Delagnes, X. de la Broise, A. Delbart, F. Druillole, E. Mazzucato, E. Monmarthe, F. Pierre, and M. Zito. AFTER, an ASIC for the Readout of the large T2K Time Projection Chambers. *IEEE Transactions on Nuclear Science*, **55**(3), 2008.

[66] Y. Kudenko. The near neutrino detector for the T2K experiment. *Nucl. Instr. and Meth. Phys. Res. A*, **598**:289, 2009.

[67] SRIM: The Stopping and Range of Ions in Matter. http://www.srim.org.

[68] J. F. Ziegler, M. D. Ziegler, and J. P. Biersack. SRIM - The stopping and range of ions in matter. *Nucl. Instr. and Meth. Phys. Res. B*, **268**:1818, 2010.

[69] LISE++: Exotic Beam Production with Fragment Separators. http://lise.nscl.msu.edu/lise.html.

[70] O. B. Tarasov and D. Bazin. LISE++: Radioactive beam production with in-flight separators. *Nucl. Instr. and Meth. Phys. Res. B*, **4657**:266, 2008.

[71] L. C. Chamon. The São Paulo Potential. *Nucl. Phys. A*, **787**:198, 2007.

[72] L. C. Chamon, B. V. Carlson, L. R. Gasques, D. Pereira, C. De Conti, M. A. G. Alvarez, M. S. Hussein, M. A. Cândido Ribeiro, Jr. E. S. Rossi, and C. P. Silva. Toward a global description of the nucleus-nucleus interaction. *Phys. Rev. C*, **66**:014610, 2002.

[73] TUNL Nuclear Data Project. http://www.tunl.duke.edu/nucldata/.

[74] V. Avrigeanu and P. E. Hodgson. Global optical potentials for emitted alpha particles. *Phys. Rev. C*, **49**:2136, 1994.

[75] P. David, J. Debrus, H. Mommsen, and A. Riccato. Elastic Scattering of α-Particles on ^{10}B for $E_\alpha = 5 - 30$ MeV. *Nucl. Phys. A*, **182**:234, 1972.

[76] F. P. Brady, J. A. Jungerman, and J. C. Young. Elastic Alpha-Particle Scattering at 8.75, 9.35, and 10.15 MeV. *Nucl. Phys. A*, **98**:241, 1967.

[77] P. Descouvemont and D. Baye. The R-matrix theory. *Rep. Prog. Phys.*, **73**:036301, 2010.

[78] T. Y. Li and B. Hird. Analysis of the $C^{12}(p,\alpha)B^9$ Reaction at 44.5 MeV. *Phys. Rev.*, **174**:1130, 1968.

[79] M. Freer, N. L. Achouri, C. Angulo, N. I. Ashwood, D. W. Bardayan, S. Brown, W. N. Catford, K. A. Chipps, N. Curtis, P. Demaret, C. Harlin, B. Laurent, J. D. Malcolm, M. Milin, T. Munoz-Britton, N. A. Orr, S. D. Pain, D. Price, R. Raabe, N. Soić, J. S. Thomas, C. Wheldon, G. Wilson, and V. A. Ziman. Resonances in ^{11}C observed in the ^{4}He(^{7}Be, α)^{7}Be and ^{4}He(^{7}Be, p)^{10}B reactions. *Phys. Rev. C*, **85**:014304, 2012.

[80] T. Suhara and Y. Kanada-En'yo. ^{14}Be + α Correlation in ^{14}C. *Proceedings of Workshop on Hadron and Nuclear Physics, HNP09*, page 366, 2010.

[81] P. Chevallier, F. Scheibling, G. Goldring, I. Plesser, and M. W. Sachs. Breakup of O^{16} into Be^8 + Be^8. *Phys. Rev.*, **160**:827, 1967.

[82] Y. Suzuki, H. Horiuchi, and K. Ikeda. Study of α Chain States through Their Decay Widths. *Prog. Theor. Phys.*, **47**:1517, 1972.

[83] M. Freer, M. P. Nicoli, S. M. Singer, C. A. Bremner, S. P. G. Chappell, W. D. M. Rae, I. Boztosun, B. R. Fulton, D. L. Watson, B. J. Greenhalgh, G. K. Dillon, R. L. Cowin, and D. C. Weisser. ^{8}Be + ^{8}Be decay of excited states in ^{16}O. *Phys. Rev. C*, **70**:064311, 2004.

[84] M. Freer, N. M. Clarke, N. Curtis, B. R. Fulton, S. J. Hall, M. J. Leddy, J. S. Pople, G. Tungate, R. P. Ward, P. M. Simmons, W. D. M. Rae, S. P. G. Chappell, S. P. Fox, C. D. Jones, D. L. Watson, G. J. Gyapong, S. M. Singer, W. N Catford, and P. H. Regan. ^{8}Be and α decay of ^{16}O. *Phys. Rev. C*, **51**:1682, 1995.

[85] J. Malcolm. *Study of Excited States in ^{14}C via the $^{4}He(^{10}Be,\alpha)^{10}Be$ Resonance Scattering Reaction*. PhD dissertation, The University of Birmingham, 2012.

[86] D. A. Resler, H. D. Knox, P. E. Koehler, and R. O. Lane. Structure of ^{14}C via elastic and inelastic neutron scattering from ^{13}C: Measurement and R-matrix analysis. *Phys. Rev. C*, **39**:766, 1989.

[87] F. Ajzenberg-Selove. Energy Levels of Light Nuclei $A = 13 - 15$. *Nucl. Phys. A*, **523**:1, 1991.

[88] E. Korkmaz, S. E. Vigdor, W. W. Jacobs, T. G. Throwe, L. C. Bland, M. C. Green, P. L. Jolivette, and J. D. Brown. ^{12,13}C$(\vec{p},\pi^{\pm})$ reactions at $T_p = 200$ MeV. *Phys. Rev. C*, **40**:813, 1989.

[89] N. Soić, M. Freer, L. Donadille, N. M. Clarke, P. J. Leask, W. N Catford, K. L. Jones, D. Mahboub, B. R. Fulton, B. J. Greenhalgh, D. L. Watson, and D. C. Weisser. ^{4}He decay of excited states in ^{14}C. *Phys. Rev. C*, **68**:014321, 2003.

[90] D. L. Price, M. Freer, S. Ahmed, N. I. Ashwood, N. M. Clarke, N. Curtis, P. McEwan, C. J. Metelko, B. Novatski, S. Sakuta, N. Soić, D. Stepanov, and V. Ziman. Alpha-decay of excited states in ^{13}C and ^{14}C. *Nucl. Phys. A*, **765**:263, 2006.

[91] D. L. Price, M. Freer, N. I. Ashwood, N. M. Clarke, N. Curtis, L. Giot, V. Lima, P. McEwan, B. Novatski, N. A. Orr, S. Sakuta, J. A. Scarpaci, D. Stepanov, and V. Ziman. α decay of excited states in ^{14}C. *Phys. Rev. C*, **75**:014305, 2007.